

Durham E-Theses

Monte Carlo Simulations of Heavy Particles for the Large Hadron Collider

DAVID ELLIOT WINN

How to cite:

WINN, DAVID ELLIOT (2013) Monte Carlo Simulations of Heavy Particles for the Large Hadron Collider. Doctoral thesis, Durham University.

Use policy

The full-text may be used and/or reproduced, and given to third parties in any format or medium, without prior permission or charge, for personal research or study, educational, or not-for-profit purposes provided that:

- a full bibliographic reference is made to the original source
- a <https://etheses.durham.ac.uk/id/eprint/6913/> is made to the metadata record in Durham E-Theses
- the full-text is not changed in any way

The full-text must not be sold in any format or medium without the formal permission of the copyright holders.

Please consult the [full Durham E-Theses policy](#) for further details.

Monte Carlo Simulations of Heavy Particles for the Large Hadron Collider

David Winn

A Thesis presented for the degree of
Doctor of Philosophy



Institute for Particle Physics Phenomenology
Department of Physics
University of Durham
England

March 2013

Dedicated to my parents

without whom none of this would have been possible.

Monte Carlo Simulations of Heavy Particles for the Large Hadron Collider

David Winn

Submitted for the degree of Doctor of Philosophy

March 2013

Abstract

As the Large Hadron Collider has switched on at CERN in Geneva, accurate predictions for complex hadronic processes are essential for the validation of theory and therefore the success of the machine. After motivating the requirement for a Monte Carlo event generator, the principles and Physics behind such a generator are laid out.

Following this, the Monte Carlo tuning system *Professor* is used to give an assessment of the uncertainty from tuning *Herwig++* and the results from this analysis used, along with a more accurate implementation of Higgs boson decays using the POWHEG method, to determine the error associated with searching for the Higgs boson with a jet substructure technique.

Then, modifications to the shower to take into account the top quark width are presented along with radiation patterns from top quark production processes for up to two external gluons. A general algorithm is outlined for systematically including these corrections.

Finally, as the LHC is ultimately a discovery machine, it is pertinent to provide Monte Carlo studies of new Physics. The colour sextet diquark model is looked at in the final chapter of this thesis, and the associated phenomenology studied.

Declaration

The work in this thesis is based on research carried out at the Institute for Particle Physics Phenomenology, the Department of Physics, Durham, England under STFC Studentship ST/F007299/1. The work in this thesis was carried out in collaboration with Prof. Peter Richardson and as part of the wider Herwig++ collaboration. Parts of this thesis therefore either will be seen or have been seen previously:

1. The majority of the work undertaken in Chapter 2 has been published as:
P. Richardson and D. Winn, *Investigation of Monte Carlo Uncertainties on Higgs Boson searches using Jet Substructure*, *Eur.Phys.J.* **C72** (2012) 1862, [arXiv:1207.0380].
2. The majority of the work undertaken in Chapter 3 is in preparation as:
P. Richardson and D. Winn, *Improved Monte Carlo Simulation of Soft Radiation in the Production and Decay of Unstable Particles*, arXiv:13mm.xxxx.
3. The majority of the work undertaken in Chapter 4 has been published as:
P. Richardson and D. Winn, *Simulation of Sextet Diquark Production*, *Eur.Phys.J.* **C72** (2012) 1862, [arXiv:1108.6154].

No part of this thesis has been submitted elsewhere for any other degree or qualification.

Copyright © 2013 by David Winn.

“The copyright of this thesis rests with the author. No quotations from it should be published without the author’s prior written consent and information derived from it should be acknowledged”.

Acknowledgements

Firstly I would like to thank my supervisor Peter Richardson. I have enjoyed working with Peter and without his guidance, help and endless patience this thesis would never have been written.

I am also thankful to other members of the **Herwig++** collaboration for all their help, in particular David Grellscheid for all his help with any computing issues I may have had and for taking the time to explain the solutions to my problems. I hope the collaboration continues to go from strength to strength.

I would also like to thank all members of the IPPP who have made my time there so enjoyable. This especially includes my office mates Steven and James who have had to endure my endless cursing at the computer and other general problems whilst also using them as a sounding board.

Finally I would like to say how much those closest in my life are appreciated. Firstly, my parents -without your love and support I wouldn't be anywhere close to where I am today - thank you. And finally to my fiancée Georgie, who probably now knows more about the Grid than any non-Physicist in the country, "this is it."

All Watched Over by Machines of Loving Grace

I like to think (and
the sooner the better!)
of a cybernetic meadow
where mammals and computers
live together in mutually
programming harmony
like pure water
touching clear sky.

I like to think
(right now, please!)
of a cybernetic forest
filled with pines and electronics
where deer stroll peacefully
past computers
as if they were flowers
with spinning blossoms.

I like to think
(it has to be!)
of a cybernetic ecology
where we are free of our labors
and joined back to nature,
returned to our mammal
brothers and sisters,
and all watched over
by machines of loving grace.

Richard Brautigan

Contents

Abstract	iii
Declaration	iv
Acknowledgements	v
1 Introduction	1
1.1 The Standard Model	2
1.1.1 Symmetries	2
1.1.2 Quantum Chromodynamics	5
1.1.3 Electroweak Theory	8
1.1.4 The Higgs Mechanism	9
1.1.5 Renormalization, Divergences and Running Couplings	14
1.2 Monte Carlo Simulations	18
1.2.1 Parton Splitting	19
1.2.2 A Monte Carlo Event Generator	31
1.3 Next-to-Leading Order Processes	39
1.3.1 Numerical Integration	39
1.3.2 POWHEG	41
2 Jet Substructure and Boosted Higgs Studies	43
2.1 Simulation of $h^0 \rightarrow b\bar{b}$ using the POWHEG Method	46
2.2 Tuning Herwig++	50
2.3 Jet Substructure of Boosted Higgs	60
2.4 Conclusions	66

3 Improved Simulation of Soft Radiation in the Production and Decay of Unstable Particles	68
3.1 Radiation Patterns	70
3.1.1 Top Quark Pair Production in Hadron–Hadron Collisions . . .	70
3.1.2 $e^+e^- \rightarrow t\bar{t}$	85
3.2 SUSY Processes	88
3.2.1 $q\bar{q} \rightarrow \tilde{t}\tilde{t}^*$	88
3.2.2 $e^+e^- \rightarrow \tilde{t}\tilde{t}^*$	89
3.3 Algorithm	92
3.4 Results	94
3.5 Conclusions	97
4 Colour Sextet Diquark Phenomenology	99
4.1 Simulation	100
4.1.1 Lagrangian	100
4.1.2 Colour Decomposition	103
4.2 Phenomenology	108
4.2.1 Resonance Production	109
4.2.2 Pair Production	113
4.3 Conclusions	116
5 Conclusions	118
Appendix	121
A Monte Carlo Integration	121
B Jets and Jet Algorithms	125
C Triple Gluon Vertex	130
D Veto Algorithm	132

List of Figures

1.1	The shape of the potential $V(x) = \mu^2 x^2 + x^4$ for different values of μ .	10
1.2	The particle content of the Standard Model.	14
1.3	An example of a perturbative series in pQCD for $e^+e^- \rightarrow q\bar{q}$.	15
1.4	A simple loop in a propagator.	16
1.5	The cancellation of infrared divergences in the matrix element squared at the Next-to-Leading order level.	18
1.6	The splitting of $q \rightarrow qg$.	19
1.7	Feynman diagram and colour flow for $q\bar{q} \rightarrow g \rightarrow q\bar{q}$.	29
1.8	A diagrammatic representation of angular ordering in the shower, where radiation occurs in cones to the radiating particle's colour partner.	30
2.1	The branching ratio of the Higgs boson with respect to mass using results from Ref. [1].	44
2.2	The two real-emission processes contributing to the NLO decay rate.	47
2.3	The scale at which we go from a two to a three jet event for Higgs boson decays using the LO and new POWHEG implementation in Herwig++.	50
2.4	The χ'^2/N_{df} distributions for the parameters that were varied from their default values whilst determining the error tune. The scatter of the results gives a representation of the systematics of tuning procedure.	55
2.5	Results from the DELPHI [2] analysis of out-of-plane p_T with-respect-to the thrust axis and 1-thrust showing the new tune and the envelopes corresponding to a change in $\Delta\chi'^2/N_{\text{df}} = 5$.	57

- 2.6 Results from the DELPHI [2] analysis of out-of-plane p_T with-respect-to the thrust axis and 1-thrust showing the new tune and the envelopes corresponding to a change in $\Delta\chi'^2/N_{\text{df}} = 10$ 57
- 2.7 A scan of `PSplitLight` using the internal `Herwig++` tuning system with the other parameters fixed at their new tuned value. From the total χ'^2/N_{df} we see that a value of 0.90 for `PSplitLight` is favoured at the new tuned parameters driven by the multiplicities. 58
- 2.8 Results for the reconstructed Higgs boson mass distribution using `HERWIG` leading-order matrix elements for top quark pair production, and the production of W^\pm and Z^0 bosons in association with a hard jet. A SM Higgs boson was assumed with a mass of 115 GeV. 60
- 2.9 Results for the reconstructed Higgs boson mass distribution using leading-order matrix elements. A SM Higgs boson was assumed with a mass of 115 GeV. In addition to the full result the contribution from top quark pair production ($t\bar{t}$), the production of W^\pm (W+Jet) and Z^0 (Z+Jet) bosons in association with a hard jet, vector boson pair production (VV) and the production of a vector boson in association with the Higgs boson (V+Higgs), are shown. 61
- 2.10 Results for the reconstructed Higgs boson mass distribution using leading-order matrix elements for top quark pair production ($t\bar{t}$), and the production of W^\pm (W+Jet) and Z^0 (Z+Jet) bosons in association with a hard jet. The next-to-leading-order corrections are included for vector boson pair production (VV) and the production of a vector boson in association with the Higgs boson (V+Higgs) as well as in the decay of the Higgs boson, $h^0 \rightarrow b\bar{b}$. A SM Higgs boson was assumed with a mass of 115 GeV. 62
- 2.11 Results for the reconstructed Higgs boson mass distribution using leading-order matrix elements. A SM Higgs boson was assumed with a mass of 115 GeV. The envelope shows the uncertainty from the Monte Carlo simulation. We have not shown the statistical error. 65

2.12	Results for the reconstructed Higgs boson mass distribution using leading-order matrix elements for top quark pair production, and the production of W^\pm and Z^0 bosons in association with a hard jet. The next-to-leading-order corrections are included for vector boson pair production and the production of a vector boson in association with the Higgs boson as well as in the decay of the Higgs boson, $h^0 \rightarrow b\bar{b}$. A SM Higgs boson was assumed with a mass of 115 GeV. The envelope shows the uncertainty from the Monte Carlo simulation. We have not shown the statistical error.	66
3.1	The tree level initial state quark-quark initiated top quark production process and associated colour flow.	70
3.2	The tree level initial state gluon-gluon top quark production processes.	70
3.3	A schematic of the kinematics used to plot the $t\bar{t}$ single gluon emission radiation patterns shown below. The incoming beam particles depend on the process being studied.	77
3.4	The radiation pattern for single emission from $q\bar{q} \rightarrow t\bar{t}$. Noting the logarithmic scale, we show the full radiation pattern, the shower approximation to the full radiation pattern and the leading N_C contribution. E_k is the energy of the emitted gluon. The dips in the pattern are associated with the finite bottom quark mass and we see singularities with the incoming quarks at 0° and 180° . These features are repeated in the other radiation patterns we will display here. We also note that the leading approximation as employed in the shower interpretation is performing well, meaning in the collinear region of interest the approximation is good.	78
3.5	Colour flow diagrams for the gluon-gluon initiated processes.	79
3.6	The radiation pattern for single emission from $gg \rightarrow t\bar{t}$. We show the full radiation pattern, the shower approximation to the full radiation pattern and the leading N_C contribution to the radiation pattern. E_k is the energy of the emitted gluon.	80
3.7	$C_t(1 - D_t)$ for different gluon energies.	82

- 3.8 The radiation pattern for double emission from $q\bar{q} \rightarrow t\bar{t}$. We show the full radiation pattern, the shower approximation to the full radiation pattern and the leading N_C contribution. E_{k_1} is the energy of the gluon from the first emission and E_{k_2} is the energy of the gluon from the second emission. 86
- 3.9 The radiation pattern for double emission from $gg \rightarrow t\bar{t}$. We show the full radiation pattern, the shower approximation to the full radiation pattern and the leading N_C contribution. E_{k_1} is the energy of the gluon from the first emission and E_{k_2} is the energy of the gluon from the second emission. 86
- 3.10 The production of top quarks by e^+e^- 87
- 3.11 The radiation pattern for single gluon emission from e^+e^- collisions. We show the full radiation pattern, the shower approximation to the full radiation pattern and shower approximation with the interference terms neglected. These interference terms are so small, that this line lies on top of the shower approximation line. 87
- 3.12 The production of stop quarks by the $q\bar{q}$ initiated processes. 88
- 3.13 The radiation pattern for single emission from $q\bar{q} \rightarrow t\bar{t}^*$. We show the full radiation pattern, the shower approximation to the full radiation pattern and the leading N_C contribution. E_k is the energy of the emitted gluon. 90
- 3.14 The production of stop quarks in e^+e^- collisions. 90
- 3.15 The radiation pattern for single gluon emission from e^+e^- collisions producing top squarks. We show the full radiation pattern, the shower approximation to the full radiation pattern and shower approximation with the interference terms neglected. 93
- 3.16 The probabilities of radiation from the colour lines of a gluon undergoing secondary radiation of a gluon whilst colour connected to a top and bottom in this example. 94

3.17	A plot showing the effects of the new multi-scale shower with and without hadronization on the top mass using the Rivet MC_TTBAR analysis.	95
3.18	A plot showing the effects of the new multi-scale shower with and without hadronization on the top mass using the HEPTopTagger analysis.	95
3.19	A plot showing the effects of the new multi-scale shower without hadronization and with increasing width on the top mass using the Rivet MC_TTBAR analysis.	96
3.20	A plot showing the effects of the new multi-scale shower with and without hadronization on the heavy top quark mass in a Little Higgs model using a similar analysis to the Rivet MC_TTBAR analysis. . . .	97
4.1	The radiation pattern associated with gluon emission from the incoming and outgoing quarks during resonant production, where θ is the polar angle of the gluon with respect to the z -axis.	102
4.2	Resonant production and decay of a diquark	104
4.3	Unique colour flows associated with the resonant production of a diquark.	104
4.4	The four diagrams contributing to the pair production of a diquark. .	105
4.5	Unique colour flows associated with the pair production of diquarks. .	107
4.6	Colour flows for a diquark emitting a gluon during the shower. . . .	108
4.7	The diquark width as a function of the diquark mass for a coupling as quoted in the text for scalar and vector diquarks. The diquark coupling to quarks has been taken to be 0.1.	109
4.8	Cross section for the production of vector and scalar diquarks as a function of the diquark mass for both resonant production, from incoming uu states, and diquark pair production at $\sqrt{s} = 14$ TeV. The diquark coupling to quarks has been taken to be 0.1.	110
4.9	The dijet mass spectrum at $\sqrt{s} = 7$ TeV for 500 GeV, 800 GeV, 1200 GeV, 1600 GeV and 2000 GeV diquark masses with the couplings given in the text.	112

4.10	The dijet mass spectrum at $\sqrt{s} = 14$ TeV for 500 GeV, 800 GeV, 1200 GeV, 1600 GeV and 2000 GeV diquark masses with the couplings given in the text.	112
4.11	Limit on the coupling as a function of the diquark mass based on the model independent data given in the recent ATLAS publications [3,4]. The band reflects the uncertainty from varying the scale between 50% and 200% of the diquark mass.	113
4.12	The mass spectrum of dijet pairs in four jet events at $\sqrt{s} = 7$ TeV for 500 GeV, 800 GeV, 1200 GeV, 1600 GeV and 2000 GeV diquark masses.	115
4.13	The mass spectrum of dijet pairs in four jet events at $\sqrt{s} = 14$ TeV for 500 GeV, 800 GeV, 1200 GeV, 1600 GeV and 2000 GeV diquark masses.	115
4.14	$\frac{S}{\sqrt{B}}$ for the scalar and vector diquark at luminosities of $\mathcal{L} = 1 \text{ fb}^{-1}$ and $\mathcal{L} = 5 \text{ fb}^{-1}$ at $\sqrt{s} = 7$ TeV and $\mathcal{L} = 10 \text{ fb}^{-1}$ and $\mathcal{L} = 100 \text{ fb}^{-1}$ at $\sqrt{s} = 14$ TeV. The black horizontal line shows $\frac{S}{\sqrt{B}} = 5$	116
A.1	The evaluation of π using the hit or miss method.	124
B.1	The simulated production of microscopic black hole in the ATLAS detector at the LHC. Image courtesy of the CERN press office, with whom copyright remains.	125
B.2	An example of the cancellation of divergencies in jets, taken from Ref. [5].	127
C.1	The triple gluon vertex.	130
D.1	The region of integration in the veto algorithm.	133

List of Tables

1.1	The transformation of the fermions under the different groups for the left-handed and right-handed fermions in the Electroweak theory.	8
1.2	The transformation of the Higgs doublet in the Electroweak theory.	11
1.3	The quantum numbers of the fermions of the SM.	13
2.1	The ten parameters to which the jet substructure is most sensitive with their default values, the allowed range of these values in Herwig++, the range scanned over and the new optimum value found from minimizing χ'^2	52
2.2	Observables used in the tuning and associated weights for observables taken from [6].	53
2.3	Observables used in the tuning and associated weights for observables taken from [2].	53
2.4	Multiplicities used in the tuning and associated weights for observables taken from [7].	54
2.5	Observables used in the tuning and associated weights for observables taken from [8].	54
2.6	The five directions corresponding to the error tune for a $\Delta\chi'^2/N_{\text{df}} = 5$ and the values the parameters take in each direction.	59
2.7	The five directions corresponding to the error tune for a $\Delta\chi'^2/N_{\text{df}} = 10$ and the values the parameters take in each direction.	59
2.8	The significance of the different processes for the leading- and next-to-leading-order matrix elements. The significance is calculated using all masses in the range 112-120 GeV.	63

A.1	A comparison of the uniform sampling method and the importance sampling method for the integration of the function $f(x) = \sin\left(\frac{\pi x}{2}\right)$, $N = 10^3$	124
-----	---	-----

Chapter 1

Introduction

The Standard Model (SM) was first written down over thirty years [9–11] ago and is arguably the crown jewel in man’s achievements. It is a theory of almost everything, except for gravity, and its ability to explain and predict experimental observables is both monumental and problematic. It is monumental in that it has been tested and verified repeatedly at collider experiments, and problematic as it does not include gravity. In this chapter the basics of the SM are outlined along with how calculations are performed.

Providing links to theory at modern collider experiments, with their complex hadronic final states, requires a Monte Carlo event generator. These tools provide a theoretical description in a form that can be used to describe real world collider events, such as at the Large Hadron Collider (LHC) at CERN in Geneva. They provide the simulation of physical processes and therefore an ability to compare experiment and theory. Without Monte Carlo event generators, the experimental programme would not be able to interpret the results and relate the observed results to fundamental theory. Later in this chapter the principles behind a Monte Carlo event generator are detailed.

1.1 The Standard Model

1.1.1 Symmetries

The SM is based entirely on symmetries that can be explained with the Mathematics of group and gauge theories. In fact, the SM is actually an $SU(3) \times SU(2) \times U(1)$ gauge theory. To understand the ideas behind gauge theory we first turn to the example of Electromagnetism, which was the first gauge theory to be discovered.

Electromagnetism

In Electromagnetism, one can talk about the electric field \mathbf{E} or equivalently the vector potential ϕ , and the magnetic field \mathbf{B} , or the scalar potential \mathbf{A} . These are related by

$$\mathbf{E} = -\nabla\phi - \frac{\partial\mathbf{A}}{\partial t}, \quad (1.1.1a)$$

$$\mathbf{B} = \nabla \times \mathbf{A}. \quad (1.1.1b)$$

A simple transformation of the fields

$$\phi \rightarrow \phi - \frac{\partial\chi}{\partial t}, \quad (1.1.2a)$$

$$\mathbf{A} \rightarrow \mathbf{A} + \nabla\chi, \quad (1.1.2b)$$

where $\chi = \chi(\mathbf{x}, t)$ leave the original field equations in Eqn. 1.1.1 unchanged, as $\nabla \times \nabla\chi = 0$. Here we have performed a gauge transformation, by shifting the potentials that the \mathbf{E} and \mathbf{B} fields depend on by an arbitrary amount whilst leaving the \mathbf{E} and \mathbf{B} fields themselves unchanged *i.e.* \mathbf{A} and ϕ are not unique for a given \mathbf{E} and \mathbf{B} [12]. By writing

$$A^\mu = (\phi, \mathbf{A}), \quad (1.1.3)$$

we may write the gauge transformation more compactly as

$$A^\mu \rightarrow A^\mu - \partial^\mu\chi, \quad (1.1.4)$$

and we may more compactly write the current as

$$j^\mu = (\rho, \mathbf{j}). \quad (1.1.5)$$

This allows us to write Maxwell's equations in the form

$$\partial_\mu F^{\mu\nu} = j^\nu, \quad (1.1.6)$$

where we have introduced the electromagnetic field strength tensor

$$F^{\mu\nu} = \partial^\mu A^\nu - \partial^\nu A^\mu, \quad (1.1.7)$$

which is also a gauge-invariant quantity. It is these principles that guide us in building our theory of Particle Physics.

This still leaves us with the question of how to actually construct a theory. Again, we are driven by what symmetries we wish our theory to obey and from that, what we are allowed to write down. So other than choosing which particles we wish to describe, we must also choose what symmetries we wish these particles to obey. Only then may we write down the most general invariant Lagrangian with these particles, obeying these symmetries, as our theory.

Guided by past principles, it is clear that for the theory of the SM, one symmetry we will always require is that our theory be Lorentz invariant. We also further constrain the theory by requiring it to be renormalizable - where the renormalizability is related to the short distance divergences in the theory.

When performing calculations at one-loop level and beyond, divergences arise at large momentum scales, *i.e.* short distances. The renormalizability of the theory means that we can reabsorb these divergences into the bare parameters of the theory, leaving it finite at short distances.¹ With regards to writing down our theory, in practice this means not writing down any operators with a mass/energy dimension greater than four in the Lagrangian. We will discuss renormalization more later in this chapter.

Following on, from the example of Electromagnetism, we turn now to Quantum Electrodynamics (QED) as a further simple example of gauge invariance and gauge symmetry where we will see that the gauge symmetry gives rise to the interactions between the particles of the theory, and where the gauge bosons act as the force

¹t Hooft proved that the SM is a renormalizable gauge theory with a spontaneous broken symmetry [13, 14].

carriers. From this, we will then go on to discuss the more complicated non-Abelian case of Quantum Chromodynamics (QCD).

Quantum Electrodynamics

We start with the Dirac Lagrangian which is written as a sum over the fermions

$$\mathcal{L}_{\text{Dirac}} = \sum_i \bar{\psi}_i (i\gamma^\mu \partial_\mu - m_i) \psi_i. \quad (1.1.8)$$

$\mathcal{L}_{\text{Dirac}}$ has the property of being invariant under the global U(1) transformation

$$\psi_i \rightarrow e^{i\alpha} \psi_i, \quad (1.1.9)$$

but if we promote this symmetry to be local so that now

$$\psi_i \rightarrow e^{i\alpha(x)} \psi_i, \quad (1.1.10)$$

we destroy the invariance, as the derivative acts on the $\alpha(x)$ term in the exponent. To restore the invariance of the Lagrangian under the local gauge transformation, we introduce a new vector field, A_μ , which has the following kinetic term

$$\mathcal{L}_{\text{Maxwell}} = -\frac{1}{4} F^{\mu\nu} F_{\mu\nu}, \quad (1.1.11)$$

where as before, $F^{\mu\nu} = \partial^\mu A^\nu - \partial^\nu A^\mu$. The fields therefore transform under the local gauge transformation as

$$\psi_i \rightarrow e^{i\alpha(x)} \psi_i, \quad (1.1.12a)$$

$$A_\mu \rightarrow A_\mu - \frac{1}{e} \partial_\mu \alpha(x). \quad (1.1.12b)$$

We replace the usual derivative ∂_μ with the covariant derivative $D_\mu \equiv \partial_\mu + ieA_\mu$ and we have the QED Lagrangian

$$\mathcal{L}_{\text{QED}} = \sum_i \bar{\psi}_i (i\gamma^\mu D_\mu - m_i) \psi_i - \frac{1}{4} F^{\mu\nu} F_{\mu\nu}, \quad (1.1.13)$$

which is invariant under the gauge transformation Eqn. 1.1.12. Note that a mass term for A_μ such as $m^2 A_\mu A^\mu$, is not permitted as it would not be invariant under the gauge transformations. We can therefore say that the new field we introduced, A_μ , is identified as the photon and the interaction of the photon with the fermions in the theory depends on the expansion of the covariant derivative, where the photon field lies, acting on the spinors. The strength of this coupling is dictated by the size of e , which is the charge of the positron [15, 16].

1.1.2 Quantum Chromodynamics

Before formulating the theory, we recall that for a general group G which is a set with an operator, then there are four basic axioms for the group which are²

1. Closure - $a \cdot b = c$ where $\{a, b, c\} \in G$;
2. Associativity - if $\{a, b, c\} \in G$ then $a \cdot (b \cdot c) = (a \cdot b) \cdot c$;
3. Identity - there is an element of the group such that $a \cdot I = I \cdot a = a$;
4. Inverse - for any element in the group a then there is an element a^{-1} such that $a \cdot a^{-1} = I$.

We have already seen a $U(1)$ group in the formulation of QED *i.e.* the circle group which act as rotations on the complex plane. The procedure followed in QED can be applied in general and the natural extension is to a non-Abelian theory, where the charge is a non-Abelian quantity. The QCD Lagrangian is derived in this way (we follow here the formalism in Ref. [18, 19]) and is built on the $SU(3)$ Lie group. It is in the non-Abelian nature of this theory that will give rise to self interactions of the gauge bosons. It is therefore important to understand some of the general properties of an $SU(N_C)$ group, which we review briefly now.

A general $SU(N_C)$ group consists of $N_C \times N_C$ unitary matrices with a unit determinant. The dimension of the group is $N_C^2 - 1$ and so there are $N_C^2 - 1$ traceless and hermitian group generators. In the case of $SU(3)$ these are often given by the Gell-Mann³ matrices. We do not state the Gell-Mann matrices here, however, for $SU(2)$ which the Electroweak theory is built upon, we often use the Pauli matrices. There is generally more than one representation of the group. The simplest representation is called the fundamental representation, where the generators of the group give the group transformations.

Following the group axioms, we expect operations between group elements to return an element in the group. The richness of the theory comes from the generators

²An excellent introduction to groups for Particle Physics can be found in Ref. [17].

³It was Murray Gell-Mann that chose the naming of the fundamental particles “quarks”.

obeying the commutator (or Lie bracket) [18]

$$[\mathbf{t}^A, \mathbf{t}^B] = if^{ABC}\mathbf{t}^C, \quad (1.1.14)$$

where f^{ABC} are called the structure constants of the group. The generators and Lie bracket form what is called the Lie algebra. The structure constants are numbers that can be determined for SU(3) and we state them as the completely anti-symmetric tensor, ϵ_{ijk} , for SU(2), which the Electroweak theory is built on. Using Eqn. 1.1.14 and the trivial relation

$$[[\mathbf{t}^A, \mathbf{t}^B], \mathbf{t}^C] + [[\mathbf{t}^B, \mathbf{t}^C], \mathbf{t}^A] + [[\mathbf{t}^C, \mathbf{t}^A], \mathbf{t}^B] = 0 \quad (1.1.15)$$

we get the Jacobi identity

$$f^{ABD}f^{DCE} + f^{BCD}f^{DAE} + f^{CAD}f^{DBE} = 0. \quad (1.1.16)$$

From this we see that the structure constants themselves also obey the group transformation forming an important representation of the group called the adjoint representation, where the generators of the adjoint representation are $\mathbf{T}_{(BC)}^A = -if^{ABC}$ [18].

As we will be using many relations of SU(3), which is of interest in building QCD, we cite here the conventions for the normalization of the matrices, which is such that [18]

$$\text{Tr}(\mathbf{t}^A\mathbf{t}^B) = T_R\delta^{AB}, \quad T_R = \frac{1}{2}. \quad (1.1.17)$$

This means the colour matrices of SU(3) obey

$$\text{Tr}(\mathbf{t}^A\mathbf{t}^A) = \mathbf{t}_{mb}^A\mathbf{t}_{bn}^A = C_F\delta_{mm}, \quad C_F = \frac{N_C^2 - 1}{2N_C}, \quad (1.1.18)$$

which we will make use of throughout this thesis, and for the adjoint representation

$$\text{Tr}(\mathbf{T}^C\mathbf{T}^D) = \sum_{A,B} f^{ABC}f^{ABD} = C_A\delta^{CD}, \quad C_A = N_C, \quad (1.1.19)$$

i.e. $C_F = \frac{4}{3}$ and $C_A = 3$ for $N_C = 3$. We may now use this knowledge to derive the QCD Lagrangian, where we start like in QED with the Dirac Lagrangian, here for quarks

$$\mathcal{L}_{\text{Dirac}} = \sum_a \bar{q}_a (i\gamma^\mu\partial_\mu - m) q_a. \quad (1.1.20)$$

where now our index a runs over the $N_C = 3$ quark colours, we have an explicit sum over the quark types and we introduce a non-Abelian symmetry that transforms the fields by

$$q_a \rightarrow \Omega(\theta)_{ab} q^b, \quad (1.1.21)$$

where $\theta = \theta(x)$ are the parameters of the transformation and we note that the transformation carries indices itself [19] *i.e.*

$$\Omega(\theta)_{ab} = \exp(i\theta_A(x)\mathbf{t}_{ab}^A) \quad (1.1.22)$$

where the \mathbf{t}_{ab}^A are the generators of the $SU(N_C)$ group and the index A runs over the $N_C^2 - 1$ generators of the group.

To make the QCD Lagrangian invariant under local transformations as in Eqn. 1.1.21, we proceed as before by introducing $N_C^2 - 1$ gauge fields $G_{ab}^\mu = G_A^\mu \mathbf{t}_{ab}^A$ and replace ∂_μ with the covariant derivative $D_{ab}^\mu \equiv \delta_{ab}\partial^\mu + ig_s G_{ab}^\mu$, where g_s is the strong coupling. The new fields and covariant derivative transform as [19]

$$D_\mu \rightarrow \Omega(\theta) D_\mu \Omega(\theta)^{-1} \quad (1.1.23a)$$

$$G^\mu \rightarrow \Omega(\theta) G^\mu \Omega(\theta)^{-1} + \frac{i}{g_s} [\partial^\mu \Omega(\theta)] \Omega(\theta)^{-1}. \quad (1.1.23b)$$

We still need to introduce the usual kinetic term for the new gauge fields G^μ . We do this by considering $[D^\mu, D^\nu] \equiv ig_s G^{\mu\nu}$, and we now find that [19]

$$G_{\mu\nu}^A = \partial_\mu G_\nu^A - \partial_\nu G_\mu^A - g_s f^{ABC} G_\mu^B G_\nu^C, \quad (1.1.24)$$

and the transformation from Eqns. 1.1.23

$$G^{\mu\nu} \rightarrow \Omega(\theta) G^{\mu\nu} \Omega(\theta)^{-1}. \quad (1.1.25)$$

Therefore, by considering a gauge invariant kinetic term for the gluons of the form $\text{Tr}([D_\mu, D_\nu][D^\mu, D^\nu])$, we construct the gauge invariant QCD Lagrangian

$$\mathcal{L}_{\text{QCD}} = \sum_i \bar{q}_i^a (i\gamma^\mu D_\mu - m_i)_{ab} q_i^b - \frac{1}{4} G_A^{\mu\nu} G_{\mu\nu}^A. \quad (1.1.26)$$

The quarks are in the fundamental representation of $SU(3)$ and the gluons, the gauge bosons, are in the adjoint representation of $SU(3)$. The fact the theory needs to be renormalizable constrains any additional terms we may try to add to the Lagrangian. Again we note that a mass term for the gluons is not permitted as it would not be invariant under gauge transformations.

SU (2)	U (1)
$Q_L \rightarrow \exp(i\frac{g}{2}\alpha(x)_i\sigma^i) Q_L$	$Q_L \rightarrow \exp(ig'Y_{qL}\alpha_0(x)) Q_L$
$u_R \rightarrow u_R$	$u_R \rightarrow \exp(ig'Y_{uR}\alpha_0(x)) u_R$
$d_R \rightarrow d_R$	$d_R \rightarrow \exp(ig'Y_{dR}\alpha_0(x)) d_R$
$L_L \rightarrow \exp(i\frac{g}{2}\alpha(x)_i\sigma^i) L_L$	$L_L \rightarrow \exp(ig'Y_{lL}\alpha_0(x)) L_L$
$e_R \rightarrow e_R$	$e_R \rightarrow \exp(ig'Y_{eR}\alpha_0(x)) e_R$

Table 1.1: The transformation of the fermions under the different groups for the left-handed and right-handed fermions in the Electroweak theory.

1.1.3 Electroweak Theory

Electricity and Magnetism were first unified by Maxwell in 1865 in his paper “A Dynamical Theory of the Electromagnetic Field” [20], then in a series of works during the 1960’s, Glashow, Salam and Weinberg unified Electromagnetism and the weak nuclear force, culminating in their award of a Nobel prize in 1979 [9–11].

The Electroweak theory is an $SU(2) \times U(1)$ gauge theory. In this theory, the left-handed spinors transform differently to the right-handed spinors, which is forced upon us by Nature allowing the W boson to only couple to left-handed particles⁴. To construct the theory, we form a left-handed doublet of fields with weak isospin $T = \frac{1}{2}$ and right-handed singlets with weak isospin $T = 0$

$$Q_L = \begin{pmatrix} u_L \\ d_L \end{pmatrix} \quad L_L = \begin{pmatrix} \nu_L \\ e_L \end{pmatrix}. \quad (1.1.27)$$

We identify u_L to have third-component of weak isospin $T_3 = \frac{1}{2}$, and d_L to have $T_3 = -\frac{1}{2}$, and similarly for the leptons. The gauge transformations under the different groups for the left and right-handed particles are shown in Table 1.1, where $\alpha(x)$ are the parameters of the transformation, σ are the Pauli matrices and Y are the weak hypercharges.

Following the same procedure as before, this necessitates the introduction of

⁴We project out the different components of the spinor using the projection operators, *i.e.* $\psi_L = P_L\psi$, where $P_L = \frac{1}{2}(1 - \gamma^5)$ and similarly $P_R = \frac{1}{2}(1 + \gamma^5)$.

three new gauge fields for the SU(2) transformation, W_i^μ , and one new gauge field for the U(1) transformation, B^μ , with the usual change of derivative to covariant derivative, so the Lagrangian is

$$\begin{aligned}\mathcal{L}_{\text{EW}} &= \mathcal{L}_{\text{gauge}} + \mathcal{L}_{\text{fermions}} + \mathcal{L}_{\text{Higgs}} \\ &= -\frac{1}{4}F_i^{\mu\nu}F_{\mu\nu}^i - \frac{1}{4}B^{\mu\nu}B_{\mu\nu} + \mathcal{L}_{\text{fermions}} + \mathcal{L}_{\text{Higgs}}\end{aligned}\quad (1.1.28)$$

where

$$\mathcal{L}_{\text{fermions}} = i\bar{Q}_L\gamma^\mu D_\mu Q_L + i\bar{L}_L\gamma^\mu D_\mu L_L + i\bar{u}_R\gamma^\mu D_\mu u_R + i\bar{d}_R\gamma^\mu D_\mu d_R + i\bar{e}_R\gamma^\mu D_\mu e_R, \quad (1.1.29)$$

describing the interactions of the fermions with the gauge bosons and also the kinetic terms for the fermions.

We still need a mass term for our fermions and bosons, and having the benefit of foresight, we include this under $\mathcal{L}_{\text{Higgs}}$. The reason for generating the masses this way, is two fold. Firstly, is that due to the different transformations of the left and right-handed fermions there is a problem with the usual Dirac mass term. A mass term such as in $\mathcal{L}_{\text{Dirac}}$ is strictly forbidden by gauge symmetry. This can be seen by considering [15]

$$\mathcal{L} = -\bar{\psi}m\psi = -m(\bar{\psi}_R\psi_L + \bar{\psi}_L\psi_R), \quad (1.1.30)$$

where clearly due to the different transformation properties of left- and right-handed fermions, is not gauge invariant. Secondly, a standard mass term for our bosons, as is required for the Z and W bosons, in our non-Abelian theory is not gauge invariant as can be seen from the transformation properties from Eqn. 1.1.23.

It is now clear why we have included $\mathcal{L}_{\text{Higgs}}$ in our Electroweak Lagrangian - to generate these masses. The theory allows mass terms via the Higgs mechanism, a spontaneously broken symmetry giving rise to masses of the gauge bosons and fermions and introduces a new boson, the Higgs boson.

1.1.4 The Higgs Mechanism

The Higgs mechanism is best explained first with a simple example before the full mechanism is added to the Electroweak Lagrangian [15,16]. The canonical example

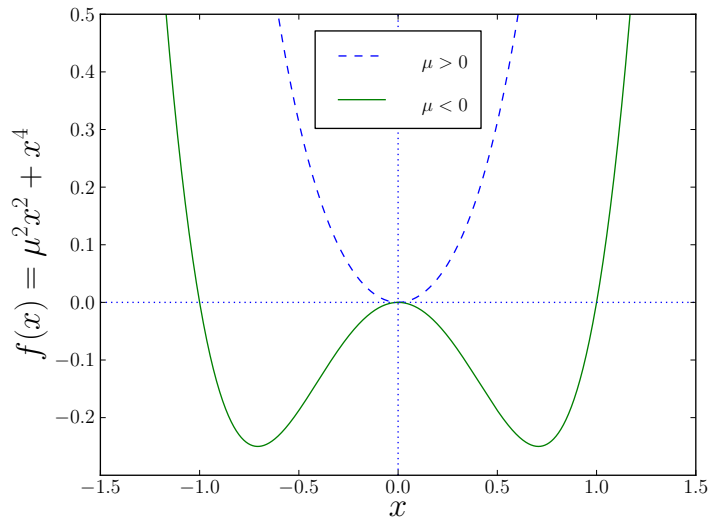


Figure 1.1: The shape of the potential $V(x) = \mu^2 x^2 + x^4$ for different values of μ .

is to consider a single complex scalar field ϕ with the Lagrangian

$$\mathcal{L} = D^\mu \phi^\dagger D_\mu \phi - \frac{1}{4} F^{\mu\nu} F_{\mu\nu} - \mu^2 \phi^\dagger \phi - \lambda (\phi^\dagger \phi)^2 \quad (1.1.31)$$

where $D_\mu = \partial_\mu + ieA_\mu$ and which we note has a global U(1) symmetry and we identify the potential as

$$V(\phi) = \mu^2 \phi^\dagger \phi + \lambda (\phi^\dagger \phi)^2. \quad (1.1.32)$$

For a classical field the ground state is found where the potential is minimum. If the vacuum energy is to be bounded from below, then we must take $\lambda > 0$ but we may choose μ^2 to be either sign. For $\mu^2 > 0$ then we obtain a parabolic shaped potential and the minimum is at the origin, however, if we take $\mu^2 < 0$, then we obtain the famous Mexican hat potential as seen in one-dimension in Fig. 1.1. We now see that the minimum of the potential lies on a circle where

$$V_{\min} = -\frac{\mu^2}{2\lambda} \quad (1.1.33)$$

and we can write

$$\phi_0 = \sqrt{-\frac{\mu^2}{2\lambda}} e^{i\phi}, \quad (1.1.34)$$

i.e. we have degeneracy in the energy states due to an azimuthal symmetry - the phase, ϕ , is arbitrary. A particular vacuum state must be realised though and

SU (2)	U (1)
$\Phi \rightarrow \exp \left(i \frac{g}{2} \alpha(x)_i \sigma^i \right) \Phi$	$\Phi \rightarrow \exp \left(i \frac{g'}{2} \alpha_0(x) \right) \Phi$

Table 1.2: The transformation of the Higgs doublet in the Electroweak theory.

choosing a vacuum state then breaks the U (1) symmetry, *i.e.* spontaneous symmetry breaking.

We choose the vacuum expectation value, v , to be real and we find the physical fields by expanding around the minimum by setting

$$\phi(x) = \frac{1}{\sqrt{2}} (v + \sigma(x) + i\eta(x)) , \quad (1.1.35)$$

where clearly the fields σ and η have zero vacuum expectation value. We then insert this into our Lagrangian and find that

$$\mathcal{L} = \frac{1}{2} \partial_\mu \sigma \partial^\mu \sigma + \frac{1}{2} \partial_\mu \eta \partial^\mu \eta - v^2 \lambda \sigma^2 + \frac{1}{2} e^2 v^2 A_\mu A^\mu - ev A_\mu \partial^\mu \eta - \frac{1}{4} F^{\mu\nu} F_{\mu\nu} + \mathcal{L}_{\text{int}} . \quad (1.1.36)$$

Now we see that we have one real massive field σ and one massless field, the Goldstone boson, η . We see the beginnings of what we want in order to generate a mass term for our physical field, as we have the term $\frac{1}{2} e^2 v^2 A_\mu A^\mu$ but we have the unwanted Goldstone boson, η . In practice, this unphysical field can be removed by an appropriate choice of gauge - the Unitary gauge.

We now apply the Higgs mechanism to the Electroweak Standard Model by introducing a weak isospin doublet of complex scalar fields, Φ , that have the transformation properties as outlined in Table 1.2.

We then add to the Lagrangian a component

$$\mathcal{L}_{\text{Higgs}} = (D_\mu \Phi)^\dagger (D^\mu \Phi) - \mu^2 \Phi^\dagger \Phi - \lambda (\Phi^\dagger \Phi)^2 , \quad (1.1.37)$$

where the covariant derivative is defined by

$$D_\mu = \partial_\mu + i \frac{g}{2} \sigma_i W_\mu^i + i \frac{g'}{2} B_\mu . \quad (1.1.38)$$

We choose the ground state to be

$$\Phi_0 = \frac{1}{\sqrt{2}} \begin{pmatrix} 0 \\ v \end{pmatrix} \quad (1.1.39)$$

and, in the unitary gauge, we expand $\Phi(x)$ as

$$\Phi(x) = \frac{1}{\sqrt{2}} \begin{pmatrix} 0 \\ v + \sigma(x) \end{pmatrix}. \quad (1.1.40)$$

Upon writing out the Lagrangian, we find that we can identify the photon and Z boson with

$$Z^\mu = \cos \theta_W W_3^\mu - \sin \theta_W B^\mu, \quad (1.1.41a)$$

$$A^\mu = \sin \theta_W W_3^\mu + \cos \theta_W B^\mu, \quad (1.1.41b)$$

where θ_W is the Weinberg angle, $m_z = \frac{m_W}{\cos \theta_W}$, there is no photon mass term and the W boson gains a mass $m_W = \frac{1}{2}vg$.

The down-type quarks and leptons gain their masses by noting that a Yukawa interaction of the form

$$\mathcal{L} = -g_d (\overline{Q}_L d_R \Phi + \Phi^\dagger \overline{d}_R Q_L) \quad (1.1.42)$$

is invariant under both the $SU(2)$ and $U(1)$ transformation, and the up-type quarks by

$$\mathcal{L} = -g_u (\overline{Q}_L u_R \tilde{\Phi} + \tilde{\Phi}^\dagger \overline{u}_R Q_L) \quad (1.1.43)$$

where $\tilde{\Phi} \equiv -i(\Phi^\dagger \sigma_2)^T$ transforms as

$$\tilde{\Phi} \rightarrow \exp(-ig\alpha(x)_i \sigma^i) \tilde{\Phi} \quad (1.1.44)$$

i.e. with opposite hypercharge compared to Φ and which can be written in Unitary gauge as

$$\tilde{\Phi}(x) = \frac{1}{\sqrt{2}} \begin{pmatrix} v + \sigma(x) \\ 0 \end{pmatrix}. \quad (1.1.45)$$

We therefore write a general gauge invariant expression for our quark masses as

$$\mathcal{L} = -\overline{Q}'_{Lm} G_{mn} d'_{Rn} \Phi - \overline{Q}'_{Lm} \tilde{G}_{mn} u'_{Rn} \tilde{\Phi} + \text{h.c.} \quad (1.1.46)$$

where now the primes indicate that the weak isospin eigenstates may not be the same as the physical mass eigenstates. We diagonalise the matrix G with a bi-unitary transformation $V^\dagger G U = D$, so we may write the Lagrangian in terms of the

Fermion	Isospin, T	T_3	Hypercharge, Y	Charge, $Q = T_3 + \frac{Y}{2}$
$\begin{pmatrix} u \\ d \end{pmatrix}_L$	$\frac{1}{2}$	$\begin{pmatrix} +\frac{1}{2} \\ -\frac{1}{2} \end{pmatrix}$	$+\frac{1}{3}$	$\begin{pmatrix} +\frac{2}{3} \\ -\frac{1}{3} \end{pmatrix}$
u_R	0	0	$+\frac{4}{3}$	$+\frac{2}{3}$
d_R	0	0	$-\frac{2}{3}$	$-\frac{1}{3}$
$\begin{pmatrix} \nu_e \\ e^- \end{pmatrix}_L$	$\frac{1}{2}$	$\begin{pmatrix} +\frac{1}{2} \\ -\frac{1}{2} \end{pmatrix}$	-1	$\begin{pmatrix} 0 \\ -1 \end{pmatrix}$
e_R^-	0	0	-2	-1

Table 1.3: The quantum numbers of the fermions of the SM.

physical mass eigenstates, *i.e.* we rotate the weak eigenstates into mass eigenstates. We make this transformation everywhere where we see the weak isospin eigenstates. This changes the non-flavour diagonal interaction terms in the Lagrangian, so now, in the interactions of the quarks and the W boson, determined by the covariant derivative, we find that in rotating to the physical mass states, we gain a factor of

$$\tilde{V}^\dagger V \equiv V_{\text{CKM}}. \quad (1.1.47)$$

This matrix, the Cabbibo-Kobayashi-Maskawa (CKM) [21, 22] matrix, allows us to work in the physical mass eigenstates, not the weak isospin eigenstates by inclusion of the appropriate factor. Unfortunately the SM has nothing to say about what values this matrix should take, and along with the masses of the fundamental particles, we must measure these quantities physically. To get a flavour for the CKM matrix, we can use the Wolfenstein parameterisation where (to $\mathcal{O}(\lambda^4)$) [23]

$$V_{\text{CKM}} = \begin{pmatrix} 1 - \lambda^2/2 & \lambda & A\lambda^3(\rho - i\eta) \\ -\lambda & 1 - \lambda^2/2 & A\lambda^2 \\ A\lambda^3(1 - \rho - i\eta) & -A\lambda^2 & 1 \end{pmatrix} \quad (1.1.48)$$

where $\lambda \approx 0.23$, $A \approx 0.81$, $\rho \approx 0.14$ and $\eta \approx 0.35$.

The lepton mass terms can be generated in a similar manner, but for massless neutrinos there is no lepton mixing matrix equivalent to the CKM matrix, as we may rotate the lepton fields to define the electron neutrino as *the* neutrino

		Generation				
		1	2	3		
Leptons	Quarks	u	c	t	Force Carriers	γ
		d	s	b		
		ν_e	ν_μ	ν_τ		Z^0
		e	μ	τ		W^\pm
H^0						

Figure 1.2: The particle content of the Standard Model.

field coupling to the electron. However, if we introduce massive neutrinos, then there is a lepton mixing matrix similar to the CKM matrix called the Pontecorvo-Make-Nakagawa-Sakate (PMNS) matrix [24], which is currently studied by neutrino oscillation experiments.

To summarise the host of quantum numbers we have encountered, the quantum numbers of the fermions of the SM can be found in Table 1.3. We also show in the Fig. 1.2 the known constituents of matter, separated into their three generations and the gauge bosons, the force carriers, and the Higgs boson.

1.1.5 Renormalization, Divergences and Running Couplings

Although we would like to solve our theory exactly, this is not possible and so in calculating quantities in the SM we make use of perturbative series, *i.e.* we view the interaction terms as a perturbation. Practically, we make a perturbative expansion in the coupling constant of the process we are interested in⁵, write down all the Feynman diagrams in the coupling expansion for the process we are interested in at a certain order, and then calculate them.

If the perturbative expansion series is asymptotic, then as we move higher in the series the magnitude of the contribution of the higher orders should be less than

⁵For this we rely upon the property of QCD known as asymptotic freedom, which is discussed next.

$$|\mathcal{M}|^2 = \left| \begin{array}{c} \text{tree} \\ + \\ \text{1-loop} \\ + \\ \text{2-loop} \\ + \dots \end{array} \right|^2$$

Figure 1.3: An example of a perturbative series in pQCD for $e^+e^- \rightarrow q\bar{q}$.

the preceding orders. So, if we wanted to calculate the total rate for $e^+e^- \rightarrow q\bar{q}$ in perturbative QCD (pQCD) we would form the series as shown in Fig. 1.3, where upon squaring, we have to be careful to only include the correct final states and only up to the order we desire in the coupling constant.

The leading-order process is generally easy to calculate, however, things become more complicated as we start to introduce quantum corrections into the calculation. Upon inclusion of a loop, we must integrate over all modes inside the loop and we see from the example [19] in Fig. 1.4 that we have a contribution

$$\int \frac{d^4k}{[(k+p)^2 - m^2] k^2} \sim \int d\Omega_3 \int dk k^3 \frac{1}{k^2 \cdot k^2} \sim \int^\Lambda \frac{dk}{k} \sim \ln \Lambda \quad (1.1.49)$$

where we have introduced an artificial cut-off on the integral, Λ to illustrate how the integral diverges as we take $\Lambda \rightarrow \infty$. Such problems are treated by the process of renormalization, whereby a regulator is introduced into the theory and then counter terms introduced to exactly balance the dependence on the regulator, thus leaving the integral finite [25]. In practice, we say that we don't measure the "bare" parameters of the Lagrangian and we only measure the physical, non-divergent, finite parameters. This amounts to us absorbing the divergences into our newly defined bare parameters, or, saying that the problem is not from the perturbative expansion itself but from the choice of parameter with which we expand [26].

The usual regulator used is the process of "dimensional regularization", whereby the calculation of the integral is done in $d = 4 - 2\epsilon$ dimensions, rendering the divergences as poles in ϵ . A subtraction scheme *e.g.* minimal subtraction bar -

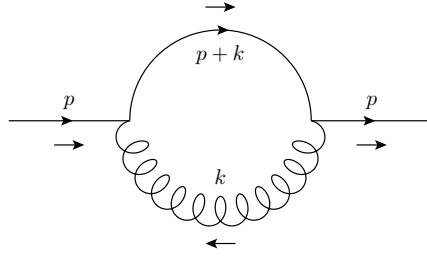


Figure 1.4: A simple loop in a propagator.

$\overline{\text{MS}}$, is then prescribed to conveniently absorb the divergences and other regularly featuring constants which vary between the schemes, thus rendering the integral finite.

The process of renormalization also introduces a new scale into the theory, the renormalization scale. Clearly a physical process cannot depend on this unphysical renormalization scale. We can express this fact by using the renormalization group equations.

If we consider the coupling of QED and define as usual

$$\alpha = \frac{e^2}{4\pi}, \quad (1.1.50)$$

the coupling has a dependence on the scale which we choose to measure it at. We define the beta function [26]

$$\beta(\alpha) = \mu^2 \frac{\partial \alpha}{\partial \mu^2}, \quad (1.1.51)$$

where the beta function is dependent on the theory in question and is calculated order by order in perturbation theory. It tells us how, in this case, the coupling evolves with the scale. In general the beta function can be written as

$$\beta(x) = bx^2 + \mathcal{O}(x^3), \quad (1.1.52)$$

then in QED, where $x = \alpha$ we find that [27]

$$b = \frac{2}{3\pi} + \mathcal{O}(\alpha^3) \quad (1.1.53)$$

and for QCD [28, 29], where $x = \alpha_s = \frac{g_s^2}{4\pi}$

$$b = - \left(\frac{11C_A - 2n_f}{12\pi} \right). \quad (1.1.54)$$

The general solution for our scale dependent coupling is

$$\alpha(Q^2) = \frac{\alpha(\mu^2)}{1 - \alpha(\mu^2) b \ln\left(\frac{Q^2}{\mu^2}\right)}. \quad (1.1.55)$$

The most remarkable thing to notice is that the negative sign of the QCD b gives rise to two, related, important properties:

- Asymptotic freedom - At high energies the coupling becomes small enough so that we may use a perturbative expansion in the coupling constant to calculate physical processes;
- Confinement - Quarks exist in bound states - hadrons. Free quarks are not seen experimentally. The reason being is that the coupling strength increases at low energies. Unfortunately, this means that we can no longer use a perturbative treatment for calculations in our theory, and so we must rely on either phenomenological models or numerical techniques with the discretization of space-time to describe hadronic properties.

Clearly, a full treatment of renormalization is beyond the scope of this thesis and for a more detailed treatment we refer to various books on the subject, *e.g.* Refs [16, 18, 19, 27, 30, 31].

Whilst renormalization deals with issues from the short range of the theory, *i.e.* high energies (U.V. divergences), we may similarly ask what happens to divergences when we move to low energies and long range interactions (I.R. divergences).

Infrared divergences are cancelled between the real and virtual contributions thanks to the Bloch-Nordsieck theorem [32] in QED and, for the SM as a whole, Kinoshita-Lee-Nauenberg (KLN) theorem [33, 34]. Schematically we write a next-to-leading order (NLO) cross section as

$$\sigma^{\text{NLO}} = \int_{n+1} d\sigma^{\text{R}} + \int_n d\sigma^{\text{V}} \quad (1.1.56)$$

where we have the real-emission terms integrated over the $n + 1$ parton phase space and the virtual contribution integrated over the n parton phase space. When we calculate these in dimensional regularization, we find that the infrared pole structure appears equally in both integrals, but crucially with the opposite sign in one

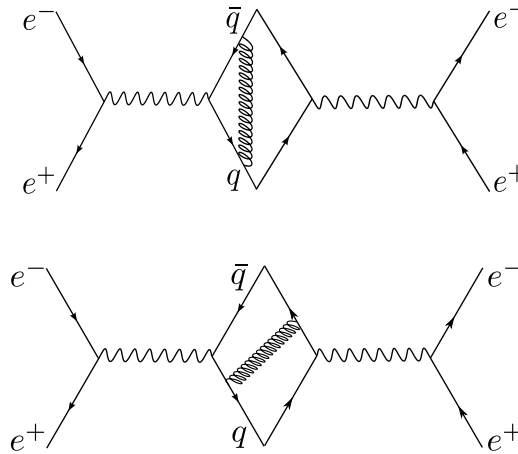


Figure 1.5: The cancellation of infrared divergences in the matrix element squared at the Next-to-Leading order level.

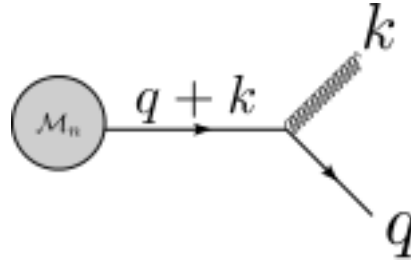
giving complete cancellation, thus rendering our calculation infrared finite. This can be seen diagrammatically when we consider the interference between both real contributions and the virtual tree-level contributions as shown in Fig. 1.5.

We need to be sufficiently inclusive, *i.e.* integrate over the appropriate phase space for these cancellations to occur. We therefore need to pick an experimental observable that is both soft and collinear safe, and this can have important consequences, *e.g.* for a particular choice of jet algorithm as discussed in Appendix B. Therefore any exclusive experimental observables, *e.g.* a central jet veto may pick up large logarithms due to incomplete cancellations.

1.2 Monte Carlo Simulations

As mentioned in the introduction to this Chapter, Monte Carlo simulations are an important tool of the modern collider experiments, and without them modern collider experiments would not be able to perform as they do. When one considers that the multiplicity of a final state at the LHC will be a few thousand particles, with multiple parton interactions, underlying event and pile-up, then one must use these state-of-the-art tools.

Below we will consider the construction of a Monte Carlo event generator in terms

Figure 1.6: The splitting of $q \rightarrow qg$.

of a hard-process and a parton shower - whereby the partons undergo branchings to form a cascade of particles producing highly complex final states.

1.2.1 Parton Splitting

One of the main features of any Monte Carlo event generator is the parton shower, whereby the incoming or outgoing partons from the hard process radiate particles in a cascade and those particles in turn go on to produce their own cascade of particles. In this way, complex final states are produced of many partons whilst summing up large contributions to the calculation in an approximation to the full pQCD calculation for such a complex process. The key in all this is therefore the splitting of a parent parton into other children partons, which then in turn split themselves. If we consider the propagator in the splitting of a quark to a quark and gluon as shown in Fig. 1.6 then there is a propagator associated with the internal quark, which in limit of vanishing mass, goes like

$$\frac{1}{(q+k)^2} = \frac{1}{2q \cdot k} = \frac{1}{2E_q E_k (1 - \cos \theta_{qk})}, \quad (1.2.1)$$

where θ_{qk} is the angle between the partons q and k . This propagator clearly has a divergence when either $\cos \theta_{qk} \rightarrow 1$ *i.e.* $\theta_{qk} \rightarrow 0$ (a collinear divergence), or when $E_q \rightarrow 0$ or $E_k \rightarrow 0$ (a soft divergence)⁶. We will examine these in turn below.

⁶For the cases where $t = (q+k)^2 > 0$ we refer to this as *timelike* branching, and for $t < 0$, we refer to this as *spacelike* branching.

Collinear Divergences

To understand more about the collinear divergences, we consider the above massless case and we write the \mathcal{M}_{n+1} matrix element as⁷

$$\mathcal{M}_{n+1} = g_s \mathbf{t}^a \epsilon^{*\alpha}(k) \bar{u}(q) \gamma^\alpha \frac{\not{q} + \not{k}}{2q \cdot k} \mathcal{M}'_n \quad (1.2.2)$$

where k is the momentum of the emitted gluon, q is the momentum of the external quark, $\epsilon^*(k)$ is the external polarization vector of the gluon and the matrix element \mathcal{M}'_n contains the remaining part of the matrix element and therefore contains spinors and gamma matrices describing the process which produced the quarks.

We now square this matrix element and sum over spins and polarizations of the gluon to obtain [19, 35]

$$|\mathcal{M}_{n+1}|^2 = \sum \epsilon^{*\alpha}(k) \epsilon^\beta(k) \frac{g_s^2 C_F}{4 (q \cdot k)^2} \text{Tr} [\mathcal{M}'_n{}^\dagger \gamma^0 (\not{q} + \not{k}) \gamma^\alpha \not{q} \gamma^\beta (\not{q} + \not{k}) \mathcal{M}'_n] , \quad (1.2.3)$$

and we will make use of the polarization relation in a physical gauge

$$\sum \epsilon^{*\alpha}(k) \epsilon^\beta(k) = -g^{\alpha\beta} + \frac{n^\alpha k^\beta + n^\beta k^\alpha}{n \cdot k} , \quad (1.2.4)$$

where n is a light like vector and upon which we apply the usual Dirac rules for gamma matrices, and keep in mind that we are treating massless particles⁸. When the smoke clears, we are left with the following expression [19, 35]

$$|\mathcal{M}_{n+1}|^2 = \frac{g_s^2 C_F}{(n \cdot k) (q \cdot k)} \text{Tr} [(\mathcal{M}'_n{}^\dagger \gamma^0) (n \cdot (k + q) (\not{k} + \not{q}) + (n \cdot q) \not{q} - \not{n} (q \cdot k)) \mathcal{M}'_n] . \quad (1.2.5)$$

At this point we introduce the Sudakov basis [37] where, in this basis, a general vector may be written as

$$q_i^\mu = \alpha_i p^\mu + \beta_i n^\mu + q_{\perp i}^\mu . \quad (1.2.6)$$

In a Monte Carlo event generator the vector p will be the momentum of the shower progenitor such that $p^2 = m^2$, the reference vector n is a light-like vector chosen

⁷We follow here the formalism of Ref. [19], except for final state branching as in Ref. [35]. An alternative derivation is given in Ref. [18].

⁸Gamma matrix algebra is often tedious and error prone for large expressions. FORM is an application which has inbuilt routines for efficiently handling gamma matrices and is used extensively throughout the work in this thesis [36].

such that $n \cdot p > m^2$, usually chosen anti-collinear to p and the q_\perp vector gives the remaining components of the momentum transverse to p and n . This means that we satisfy the following relations

$$\begin{aligned} q_{\perp i} \cdot p &= 0 & p^2 &= m^2 & q_{\perp i}^2 &= -\mathbf{p}_{\perp i}^2 \\ q_{\perp i} \cdot n &= 0 & n^2 &= 0 & n \cdot p &> m^2 \end{aligned} \quad (1.2.7)$$

We also define z to be the fraction of the parent's 4-momentum carried by the quark after the branching, *i.e.*

$$z = \frac{\alpha_i}{\alpha_{i-1}}, \quad (1.2.8)$$

meaning we can write our gluon momenta and our quark momentum in the above as

$$q^\mu = zp^\mu + \beta_q n^\mu + q_\perp \quad (1.2.9a)$$

$$k^\mu = (1-z)p^\mu + \beta_k n^\mu - q_\perp, \quad (1.2.9b)$$

and the β variables are found by the mass-shell condition $q^2 = k^2 = 0$ and Eqns. 1.2.7, such that

$$\beta_q = \frac{\mathbf{p}_\perp^2}{2zp \cdot n} \quad \text{and} \quad \beta_k = \frac{\mathbf{p}_\perp^2}{2(1-z)p \cdot n}. \quad (1.2.10)$$

Therefore, using Eqns. 1.2.9 and Eqns. 1.2.7 into Eqn. 1.2.5, we find the only non-trivial relation to be

$$q \cdot k = \frac{\mathbf{p}_\perp^2}{2z(1-z)} \quad (1.2.11)$$

and so retaining only the leading pieces, *i.e.* parts that go like $\mathcal{O}(1/\mathbf{p}_\perp^2)$, we find that

$$|\mathcal{M}_{n+1}|^2 = \frac{g_s^2 C_F}{(q \cdot k)} \frac{1+z^2}{1-z} \text{Tr} [(\mathcal{M}'_n \dagger \gamma^0) \not{p} \mathcal{M}'_n]. \quad (1.2.12)$$

Making use of the completeness relation for massless particles

$$\sum u(p)\bar{u}(p) = \not{p} \quad (1.2.13)$$

to re-insert the spinors back into \mathcal{M}'_n in Eqn. 1.2.12 leaves us with a factorized expression as [19, 35]

$$|\mathcal{M}_{n+1}|^2 = \frac{g_s^2 C_F}{(q \cdot k)} \frac{1+z^2}{1-z} |\mathcal{M}_n|^2. \quad (1.2.14)$$

This is starting to look like what we may want in terms of implementation in a Monte Carlo event generator, however, we need to consider the phase space associated with the extra emission. The $n + 1$ body phase space maybe written as [38]

$$d\Phi_n = \dots \frac{d^3\mathbf{p}}{2(2\pi)^3 E_p} \quad (1.2.15)$$

and so for our splitting $p \rightarrow q + k$ we have

$$d\Phi_{n+1} = \dots \frac{d^3\mathbf{q}}{2(2\pi)^3 E_q} \frac{d^3\mathbf{k}}{2(2\pi)^3 E_k}, \quad (1.2.16)$$

which at fixed k we may write

$$d\Phi_{n+1} = \dots \frac{d^3\mathbf{p}}{2(2\pi)^3 E_p} \frac{d^3\mathbf{k}}{2(2\pi)^3 E_k} \frac{E_p}{E_q}. \quad (1.2.17)$$

As our phase space is Lorentz invariant, we make the choice of basis [19]

$$p = E_p(1; 0, 0, 1), \quad n = (1; 0, 0, -1), \quad q_{\perp} = (0; p_{\perp} \cos \phi, p_{\perp} \sin \phi, 0) \quad (1.2.18)$$

which means that

$$k = \left((1-z)E_p + \frac{p_{\perp}^2}{4(1-z)E_p}; -p_{\perp} \cos \phi, -p_{\perp} \sin \phi, (1-z)E_p - \frac{p_{\perp}^2}{4(1-z)E_p} \right), \quad (1.2.19)$$

and similarly we see that $E_q = zE_p + \mathcal{O}(p_{\perp}^2)$ and we may write our phase space as

$$d\Phi_{n+1} = d\Phi_n \frac{1}{8\pi^2} \frac{dp_{\perp}^2}{2} \frac{d\phi}{2\pi} \frac{dk_z}{E_k} \frac{1}{z}. \quad (1.2.20)$$

We also have that

$$\frac{\partial k_z}{\partial z} = -\frac{E_k}{(1-z)} \quad (1.2.21)$$

and from Eqn. 1.2.11

$$\frac{p_{\perp}^2}{p^2} = \frac{p_{\perp}^2}{2q \cdot k} = z(1-z). \quad (1.2.22)$$

We therefore find that, after integrating over azimuthal angle,

$$d\Phi_{n+1} = d\Phi_n \frac{1}{4} \frac{1}{(2\pi)^2} dp^2 dz, \quad (1.2.23)$$

so now, for our extra emission we may write the cross-section as

$$d\sigma_{n+1} = d\sigma_n \frac{\alpha_s}{2\pi} C_F \frac{1+z^2}{1-z} dz \frac{dp^2}{p^2}. \quad (1.2.24)$$

This process can be generalised, and we may write

$$d\sigma_{n+1} = d\sigma_n \frac{\alpha_s}{2\pi} CP(z) dz \frac{dp^2}{p^2}, \quad (1.2.25)$$

where $P(z)$ are the so called Altarelli-Parisi splitting functions [39–41], and C is an appropriate colour factor for the splitting, usually part of the Altarelli-Parisi splitting functions. The other splitting functions can be derived in a similar way as above and it is found that the spin averaged functions are [42]

$$\begin{aligned} P_{qq}(z) &= C_F \frac{1+z^2}{1-z} & P_{gq}(z) &= C_F \frac{1+(1-z)^2}{z} \\ P_{gg}(z) &= C_A \frac{z^4+1+(1-z)^4}{z(1-z)} & P_{qg}(z) &= T_R(z^2+(1-z)^2) \end{aligned} \quad (1.2.26)$$

This approach also holds for an initial-state spacelike shower.

Now let us consider how the parton density changes when we have multiple branchings, as will be the case in our parton shower. To do so, we form the picture whereby a parton carrying a fraction x of the parent hadrons momentum undergoes branchings, moving to a lower momentum and a more negative virtual mass squared [18]. At some lower virtual mass squared, $t = -p^2$, the parton undergoes a hard scattering.

The change in parton density during this process is therefore the difference between the number of partons arriving in an element $(\delta t, \delta x)$ and the number leaving. Looking at Eqn. 1.2.24 we can therefore write

$$\begin{aligned} \delta f_{\text{in}} &= \frac{\delta t}{t} \int_x^1 dx' dz \frac{\alpha_s}{2\pi} P(z) f(x', t) \delta(x - zx'), \\ &= \frac{\delta t}{t} \int_0^1 \frac{dz}{z} \frac{\alpha_s}{2\pi} P(z) f\left(\frac{x}{z}, t\right), \end{aligned} \quad (1.2.27)$$

where we have integrated over all higher momentum fractions $x' = x/z$, which as $x' < 1$, we may write the lower range of the integral as 0. Now, turning our attention to the states leaving the element $(\delta t, \delta x)$, we have that

$$\begin{aligned} \delta f_{\text{out}} &= \frac{\delta t}{t} \int_0^x dx' dz \frac{\alpha_s}{2\pi} P(z) f(x, t) \delta(x - zx'), \\ &= \frac{\delta t}{t} \int_0^1 dz \frac{\alpha_s}{2\pi} P(z) f(x, t), \end{aligned} \quad (1.2.28)$$

so the total change may be written as [18]

$$\frac{\delta f_{\text{in}} - \delta f_{\text{out}}}{\delta t} = \frac{1}{t} \int_0^1 dz \frac{\alpha_s}{2\pi} P(z) \left[\frac{1}{z} f\left(\frac{x}{z}, t\right) - f(x, t) \right] \quad (1.2.29)$$

or

$$t \frac{\partial f}{\partial t} = \int_0^1 dz \frac{\alpha_s}{2\pi} P(z) \left[\frac{1}{z} f\left(\frac{x}{z}, t\right) - f(x, t) \right]. \quad (1.2.30)$$

Eqn. 1.2.30 is the famous DGLAP evolution equation that informs us how to evolve the parton distributions at one scale to another. We therefore want to be able to solve this in our Monte Carlo event generator in an iterative way to generate our parton splittings and for this, we turn to the Sudakov form factor, which is defined as

$$\Delta(t) \equiv \exp \left[- \int_{t_0}^t \frac{dt'}{t'} \int dz \frac{\alpha_s}{2\pi} P(z) \right]. \quad (1.2.31)$$

We now write the DGLAP equation Eqn. 1.2.30 in terms of this new function such that

$$\begin{aligned} t \frac{\partial f}{\partial t} &= \int \frac{dz}{z} \frac{\alpha_s}{2\pi} P(z) f\left(\frac{x}{z}, t\right) + \frac{f(x, t)}{\Delta(t)} t \frac{\partial \Delta(t)}{\partial t} \\ \Rightarrow t \frac{\partial}{\partial t} \left(\frac{f}{\Delta(t)} \right) &= \frac{1}{\Delta(t)} \int \frac{dz}{z} \frac{\alpha_s}{2\pi} P(z) f\left(\frac{x}{z}, t\right), \end{aligned} \quad (1.2.32)$$

which we now integrate to give the solution

$$f(x, t) = \Delta(t) f(x_0, t) + \int_{t_0}^t \frac{dt'}{t'} \frac{\Delta(t)}{\Delta(t')} \int \frac{dz}{z} \frac{\alpha_s}{2\pi} P(z) f\left(\frac{x}{z}, t\right). \quad (1.2.33)$$

The interpretation of Eqn. 1.2.33 will be how we implement our splittings in the Monte Carlo even generator. To aid in the interpretation, we turn to the example of radioactive decay [42]. In radioactive decay, we know simply that the number of atoms that have not decayed by a time t is given by $\exp\left(-\int_0^t \lambda dt'\right)$, and so by analogy, our Sudakov form factor in Eqn. 1.2.31 is the number of partons that haven't branched *i.e.* it is our no branching probability.

Therefore the interpretation of Eqn. 1.2.33, is that the first term is a contribution from paths in (t, x) space that do not branch between t_0 and t , and that the second term is the contribution from all paths that had their last branching at a scale t' [18]. Clearly in a parton shower, we have more than one parton type splitting, and so we include these effects by summing over parton splittings in the Sudakov form factor.

We have actually glossed over an important fact and that is that the splitting functions are unregularized and have singularities as $z \rightarrow 1$. To solve this problem, we introduce a cut-off on z which defines a resolvable emission, and so our Sudakov form factor now defines the probability of no resolvable emission.

In this way, we also include virtual corrections in the Sudakov form factor. We know from unitarity that the sum of branching and no branching probabilities must be unity and so our no resolvable branching probability tells us via unitarity the sum of unresolved and virtual corrections, which although individually divergent, have a finite sum as discussed earlier.

Using the Sudakov form factor to evolve our partons therefore allows us to sum the leading logarithms associated with the collinear divergences to all orders. Recalling from the introduction that α_s runs with scale, there is therefore still the question as what to take for the argument of α_s in our Sudakov form factor. Technically the choice of scale for α_s should be a higher order consideration, however, it can have important phenomenological implications. Naively, the natural scale choice for the process would seem to be the evolution variable scale t of the branching, however, typically we use the transverse momentum of the splitting. This is because by using the transverse momentum, it can be shown that it is possible to capture some higher terms in the series and sum some of the higher logarithms [43].

Having only considered collinear divergences so far, we must now turn our attention to the soft divergences.

Soft Divergences

We saw from earlier in Eqn. 1.2.1 that is also a soft divergence associated with the gluon energy, $E_k \rightarrow 0$. To understand the nature of these divergences, we turn again to the propagator associated with the emission of an extra gluon

$$\mathcal{M}_{n+1} = g_s \mathbf{t}^A \epsilon^{*\alpha}(k) \bar{u}(q) \gamma^\alpha \frac{\not{q} + \not{k}}{2q \cdot k} \mathcal{M}'_n$$

and now we apply the Dirac algebra to the top line and along with the eikonal approximation, *i.e.* assume the gluon momentum is small, and get

$$\begin{aligned}
\mathcal{M}_{n+1} &= g_s \mathbf{t}^A \epsilon^{*\alpha}(k) \bar{u}(q) \frac{(2q^\alpha - \not{q}\gamma^\alpha + \gamma^\alpha \not{k})}{2q \cdot k} \mathcal{M}'_n \\
&= g_s \mathbf{t}^A \epsilon^{*\alpha}(k) \bar{u}(q) \frac{(2q^\alpha + \gamma^\alpha \not{k})}{2q \cdot k} \mathcal{M}'_n \\
&= g_s \mathbf{t}^A \frac{q \cdot \epsilon^*}{q \cdot k} \bar{u}(q) \mathcal{M}'_n \\
&= g_s \mathbf{t}^A \frac{q \cdot \epsilon^*}{q \cdot k} \mathcal{M}_n.
\end{aligned} \tag{1.2.34}$$

The matrix element \mathcal{M}_{n+1} has factorized into a spin-independent soft eikonal factor multiplied by the matrix element \mathcal{M}_n . This factorization applies in general to any soft emission off an external leg. Internal off-shell lines do not receive this contribution as in that case $(p+k)^2 - m^2 \rightarrow p^2 - m^2 \neq 0$ as $k \rightarrow 0$. For emission off more than one leg, we end up with a series of dipoles, which we may express in terms of a radiation pattern.

We will compute here the basic pattern for $e^+e^- \rightarrow q\bar{q}$ with one extra gluon emission. Using the same approach as above, assuming massless quarks, we find that

$$\begin{aligned}
\mathcal{M}_{n+1} &= g_s \mathbf{t}_{ij}^A \bar{u}(p_i) \gamma^\mu \frac{(\not{p}_i + \not{k})}{2p_i \cdot k} \mathcal{M}'_n \epsilon^{*\mu}(k) \\
&\quad + g_s \mathcal{M}'_n \mathbf{t}_{ij}^A \frac{(-\not{p}_j - \not{k})}{2p_j \cdot k} \gamma^\mu v(p_j) \epsilon^{*\mu}(k)
\end{aligned} \tag{1.2.35}$$

which upon applying the Dirac algebra, squaring we get

$$|\mathcal{M}_{n+1}|^2 = |\mathcal{M}_n|^2 C_F \frac{2p_i \cdot p_j}{(p_i \cdot k)(p_j \cdot k)}. \tag{1.2.36}$$

We may now write this in terms of the radiation function W_{ij} where in general, *i.e.* for massive quarks, we define the Lorentz invariant [44]

$$\frac{2}{\omega^2} W_{ij}(k) = - \left(\frac{p_i^\mu}{p_i \cdot k} - \frac{p_j^\mu}{p_j \cdot k} \right)^2 = \frac{2}{\omega^2} \left(\frac{\xi_{ij}}{\xi_i \xi_j} - \frac{1}{2\gamma_i^2 \xi_i^2} - \frac{1}{2\gamma_j^2 \xi_j^2} \right), \tag{1.2.37}$$

where we follow convention with ω being the energy of the soft gluon and $p_{i,j}$ are the momenta of the particles forming the dipole, $\xi_{ij} = \frac{p_i \cdot p_j}{E_i E_j} = 1 - v_i v_j \cos \theta_{ij}$, $\xi_i = 1 - v_i \cos \theta_i$, $\gamma_i = E_i/m_i = 1/\sqrt{(1-v_i^2)}$, v_i is the velocity of parton i , θ_i is the

angle between the direction of motion of the soft gluon and the parton i , and θ_{ij} is the angle between the partons i and j .

We now see that we can write Eqn. 1.2.36 as

$$\begin{aligned} |\mathcal{M}_{n+1}|^2 &= |\mathcal{M}_n|^2 C_F \frac{2}{\omega^2} W_{ij} \\ &= |\mathcal{M}_n|^2 \mathcal{F}. \end{aligned} \quad (1.2.38)$$

In general for processes with more than one dipole

$$\frac{\omega^2}{2} \mathcal{F} = \sum_{ij} C_{ij} W_{ij}, \quad (1.2.39)$$

with the sum over the different W_{ij} , contributions, where C_{ij} is the associated colour factor. In general we define the leading-order matrix element,

$$\mathcal{M}_0(\{p_0\}) = \sum_n \mathcal{M}_0^n(\{p_0\}) \mathbf{T}^n, \quad (1.2.40)$$

in terms the colour-ordered amplitudes, \mathcal{M}_0^n , each with associated colour factor \mathbf{T}^n (which depends on the colours j of the external partons), where the sum is over the distinct colour-ordered amplitudes and p_0 are the momenta of the external particles.

In the eikonal limit, the emission of an extra external gluon may be written as

$$\mathcal{M}(\{p_0\}, k) = \sum_n \mathcal{M}_0^n \mathcal{J}^n \cdot \epsilon \quad (1.2.41)$$

where $\mathcal{M}(\{p_0\}, k)$ is the matrix element for the process with an extra gluon, depending on the set of leading-order momenta p_0 , the momenta of the gluon k and, ϵ_μ , the polarization vector of the radiated gluon.

The eikonal current is therefore

$$\mathcal{J}^\mu(\{p_0\}, k) = \sum_{i \in \{p_0\}} \left(\frac{p_i^\mu}{p_i \cdot k} \right) \mathbf{T}_j^n \mathbf{t}_{jk}^A, \quad (1.2.42)$$

where j/k are the colours of the i th external particle before/after the gluon emission and \mathbf{t}_{jk}^A is the colour matrix associated with the extra emission. The soft gluon distribution is then obtained by squaring the current *i.e.*

$$\frac{\omega^2}{2} \mathcal{F} = \mathcal{J}(k)^2 = \sum_{\text{spins}} (\mathcal{J}^\mu(k) \epsilon_\mu(k))^2. \quad (1.2.43)$$

Turning our attention back to the W_{ij} function, we begin by splitting it into two terms [44]

$$W_{ij} = W_{ij}^i + W_{ij}^j \quad (1.2.44)$$

such that each piece contains the leading collinear singularity

$$W_{ij}^i = \frac{1}{2\xi_i} \left(1 - \frac{1}{\gamma_i^2 \xi_i} + \frac{\xi_{ij} - \xi_i}{\xi_j} \right) = \frac{v_i}{2\xi_i} \left(\frac{A_i}{1 - v_i \cos \theta_i} + \frac{B}{1 - v_j \cos \theta_i} \right), \quad (1.2.45)$$

where $A_i = v_i - \cos \theta_i$ and $B_i = \cos \theta_i - v_j \cos \theta_{ij}$. Taking the massless case of W_{ij}^i we see that

$$W_{ij}^i = \frac{1}{2(1 - \cos \theta_i)} \left(1 + \frac{\cos \theta_i - \cos \theta_{ij}}{1 - \cos \theta_j} \right) \quad (1.2.46)$$

contains the collinear singularity as $\theta_i \rightarrow 0$. W_{ij}^i also has the remarkable property of angular ordering when we take the azimuthal average [18, 38]

$$\langle W_{ij}^i \rangle = \int_0^{2\pi} \frac{d\phi_i}{2\pi} W_{ij}^i. \quad (1.2.47)$$

To understand the angular dependence we choose the basis

$$\hat{\mathbf{p}}_i = (1, 0, 0), \quad (1.2.48a)$$

$$\hat{\mathbf{p}}_j = (\cos \theta_{ij}, \sin \theta_{ij}, 0), \quad (1.2.48b)$$

$$\hat{\mathbf{k}} = (\cos \theta_i, \cos \phi_i \sin \theta_i, \sin \phi_i \sin \theta_i), \quad (1.2.48c)$$

and we then find that all the azimuthal dependence comes from the $\cos \theta_j$ term

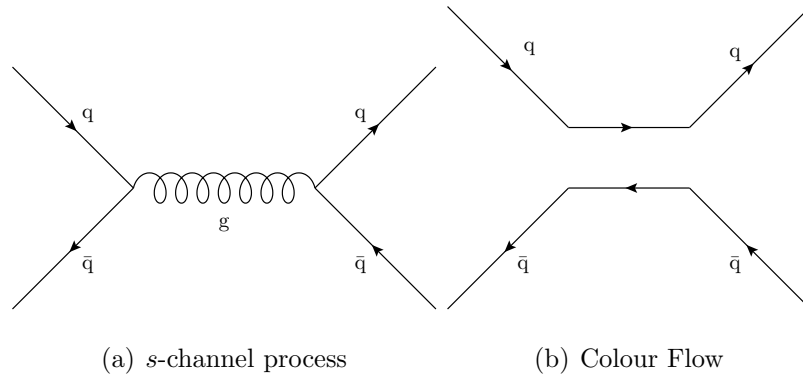
$$\cos \theta_j = \hat{\mathbf{k}} \cdot \hat{\mathbf{p}}_j = \cos \theta_{ij} \cos \theta_i + \sin \theta_{ij} \sin \theta_i \cos \phi_i. \quad (1.2.49)$$

We may use a contour integral to integrate over the ϕ_i dependence of the integral, as has been done in Ref. [18, 38]. The massive case gives the following result [44]

$$\langle W_{ij}^i \rangle = \frac{v_i}{2\xi_i} \left(\frac{A_i}{v_i A_i + \gamma_i^{-2}} + \frac{B_i}{\sqrt{B_i^2 + (\sin \theta_i / \gamma_j)^2}} \right) \quad (1.2.50)$$

which in the massless limit gives

$$\begin{aligned} \langle W_{ij}^i \rangle &= \frac{1}{2(1 - \cos \theta_i)} \left[1 + \frac{(\cos \theta_i - \cos \theta_{ij})}{|\cos \theta_i - \cos \theta_{ij}|} \right] \\ &= \begin{cases} \frac{1}{1 - \cos \theta_{ij}} & \text{if } \theta_i < \theta_{ij}, \\ 0 & \text{otherwise.} \end{cases} \end{aligned} \quad (1.2.51)$$

Figure 1.7: Feynman diagram and colour flow for $q\bar{q} \rightarrow g \rightarrow q\bar{q}$.

This tells us that soft radiation is suppressed at angles larger than θ_{ij} ⁹. We have only considered a very simple case here and it will be of benefit to see what happens in a more complicated case.

For this we now make the incoming state coloured and consider $q\bar{q} \rightarrow g \rightarrow q\bar{q}$ for which we find

$$\mathcal{J}^\mu = \frac{p_2^\mu}{p_2 \cdot k} \mathbf{t}_{mi}^A \mathbf{t}_{jm}^B \mathbf{t}_{kl}^A - \frac{p_1^\mu}{p_1 \cdot k} \mathbf{t}_{mi}^B \mathbf{t}_{jm}^A \mathbf{t}_{kl}^A + \frac{p_3^\mu}{p_3 \cdot k} \mathbf{t}_{ji}^A \mathbf{t}_{km}^B \mathbf{t}_{ml}^A - \frac{p_4^\mu}{p_4 \cdot k} \mathbf{t}_{ji}^A \mathbf{t}_{km}^A \mathbf{t}_{ml}^B, \quad (1.2.52)$$

which if we write out the colour matrices using the relation

$$\mathbf{t}_{ij}^A \mathbf{t}_{mn}^A = \frac{1}{2} \left(\delta_{in} \delta_{jm} - \frac{1}{N_C} \delta_{im} \delta_{jn} \right) \quad (1.2.53)$$

then the dipoles become explicit and

$$\begin{aligned} \mathcal{J}^\mu = & \frac{1}{2} \left(\mathbf{t}_{jl}^B \delta_{ik} \left(\frac{p_2^\mu}{p_2 \cdot k} - \frac{p_4^\mu}{p_4 \cdot k} \right) + \mathbf{t}_{ki}^B \delta_{jl} \left(\frac{p_3^\mu}{p_3 \cdot k} - \frac{p_1^\mu}{p_1 \cdot k} \right) \right) \\ & - \frac{1}{2N_C} \left(\mathbf{t}_{ji}^B \delta_{kl} \left(\frac{p_2^\mu}{p_2 \cdot k} - \frac{p_1^\mu}{p_1 \cdot k} \right) + \mathbf{t}_{kl}^B \delta_{ij} \left(\frac{p_3^\mu}{p_3 \cdot k} - \frac{p_4^\mu}{p_4 \cdot k} \right) \right), \end{aligned} \quad (1.2.54)$$

which upon squaring and dividing by the leading-order colour factor we get

$$\frac{\omega^2}{2} \mathcal{F} = \frac{N_C}{2} (W_{13} + W_{24}) + \frac{1}{2N_C} (2(W_{14} + W_{23}) - 2(W_{13} + W_{24}) - W_{12} - W_{34}). \quad (1.2.55)$$

⁹In Electrodynamics this is the well known Chudakov effect, where the photon cannot resolve the transverse separation of a pair of electrons unless the angle between the two electrons is greater than the angle of emission.

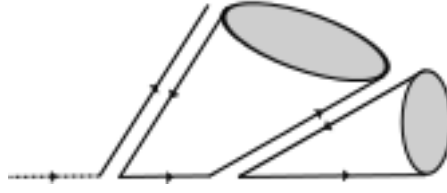


Figure 1.8: A diagrammatic representation of angular ordering in the shower, where radiation occurs in cones to the radiating particle's colour partner.

This seems like a disaster in terms of a Monte Carlo event generator, where we want to express things in terms of positive definite probabilities. To interpret Eqn. 1.2.55 we rewrite it as [44]

$$\frac{\omega^2}{2} \mathcal{F} = C_F (W_{13} + W_{24}) + \frac{1}{2N_C} (2(W_{14} + W_{23}) - W_{13} - W_{24} - W_{12} - W_{34}) , \quad (1.2.56)$$

where the last term in Eqn. 1.2.56 not only has no collinear singularities, it is also suppressed in the large N_C limit compared to the first term. We can therefore safely neglect the last term in interpreting the radiation pattern in terms of a probability, and we are left with a positive definite contribution.

We now introduce the concept of a colour partner in the large N_C limit, so in the case of the above process the colour partner of the incoming quark, is the outgoing quark and vice versa, as seen in Fig. 1.7. We therefore see that the quark can only radiate up to the angle of its colour partner, the outgoing quark. Now, for example, after the incoming quark has radiated, radiation off the daughter quark may only be up the angle of the new colour partner - the anti-colour line of the gluon. A diagram illustrating this idea is seen in Fig. 1.8. This angular ordering of the emissions gives rise to a colour coherent process, similar to the Chudakov effect. We will be seeing many examples of these radiation patterns in this thesis, and example plots are left to the appropriate sections. We should also consider the factorization of phase space in this soft limit. In the soft limit clearly

$$\frac{d^3\mathbf{p}}{2(2\pi)^3 E_p} \rightarrow \frac{d^3\mathbf{q}}{2(2\pi)^3 E_q} \quad (1.2.57)$$

and for the gluon

$$\frac{d^3\mathbf{k}}{2(2\pi)^3 E_k} = \frac{\mathbf{k}^2 dE_k d\Omega}{2(2\pi)^3 E_k} = \frac{E_k dE_k d\Omega}{16\pi^3} \quad (1.2.58)$$

and so our cross section is written in general as

$$d\sigma_{n+1} = d\sigma_n \frac{\alpha_s}{2\pi} \frac{d\Omega}{2\pi} \frac{dE_k}{E_k} \sum_{ij} C_{ij} W_{ij}. \quad (1.2.59)$$

Now we replace the $C_{ij} dE_k/E_k$ with $P(z) dz$ discussed earlier and we correctly treat both soft and collinear singularities.

To implement this effect in a Monte Carlo event generator, we should therefore order in angles, and so, instead of using $t = -p^2$ as our evolution variable, we should instead use some variable that has angular dependence.

1.2.2 A Monte Carlo Event Generator

Using the results of the last section, we can create a parton shower for a Monte Carlo event generator based on soft and collinear splittings, forming the cascade process we are interested in. In general Monte Carlo simulations describe high energy collisions using [42, 45]

1. a hard perturbative, either Leading- or Next-to-Leading-order, matrix element to simulate the fundamental hard collision process;
2. the parton shower algorithm which evolves from the scale of the hard process to a cut-off scale, $\mathcal{O}(1 \text{ GeV})$, via the successive radiation of soft and collinear quarks and gluons;
3. the generation of multiple perturbative scattering processes to simulate the underlying event;
4. the perturbative decay of any fundamental particles, with lifetimes shorter than the timescale for hadron formation, followed again by the simulation of QCD radiation from the coloured decay products using the parton shower formalism;
5. a hadronization model which describes the formation of hadrons at the cut-off scale from the quarks and gluons produced during the parton shower;
6. the decays of the unstable hadrons produced by hadronization.

So we need to understand how the hard process is implemented and how to actually proceed with generating the scales of the branchings for the parton shower from the methodology above. We also have the problem of how to efficiently evolve from the incoming hadron down towards the hard process giving us the momentum configuration we want in the hard process without rejecting too many events. In practice, we will see that this is solved by using backwards evolution from the hard process to the incoming hadron.

Hard process

Modern day calculations make use of the factorization theorem [46] which allows us to describe our cross section as a convolution between non-perturbative parton distribution function (PDFs) with a perturbative hard-scattering process. We write our cross section as

$$\begin{aligned}\sigma &= \int_0^1 dx_a dx_b \int f_a(x_a, \mu_F) f_b(x_b, \mu_F) d\hat{\sigma}_{ab \rightarrow n}(\mu_F, \mu_R) \\ &= \int_0^1 dx_a dx_b \int d\Phi_n f_a(x_a, \mu_F) f_b(x_b, \mu_F) \frac{1}{\mathcal{F}} |\mathcal{M}_{ab \rightarrow n}^2(\Phi_n, \mu_F, \mu_R)|\end{aligned}\quad (1.2.60)$$

where the $f_i(x_i, \mu_F)$ are the parton distribution functions (PDFs) of the respective incoming hadron(s), dependent on the light-cone fraction x_i of the parton i with respect to the incoming hadron. In addition $d\hat{\sigma}_{ab \rightarrow n}$ is the hard differential cross-section for the process we are interested in and we have introduced a new scale, the factorization scale μ_F along with the renormalization scale μ_R and we have introduced a flux factor \mathcal{F} associated with the phase-space integral.

In general the matrix element $|\mathcal{M}_{ab \rightarrow n}^2(\Phi_n, \mu_F, \mu_R)|$ may be either evaluated by hand and inputted into the Monte Carlo event generator or inbuilt routines may exist to calculate these from first principles, *e.g.* in **Herwig++** there is the helicity formalism - HELAS [47]. Most modern day event generators also come with an ability to read in matrix elements from an external program and then perform the subsequent parton shower and hadronization of the events.

The phase space is often complicated for processes involving $ab \rightarrow n$ where $n > 2$.

In general it is defined as

$$d\Phi_n = \prod_{i=1}^n \frac{d^3p_i}{(2\pi)^3 2E_i} \cdot (2\pi)^4 \delta^{(4)}(p_a + p_b - \sum_{i=1}^n p_i), \quad (1.2.61)$$

so we are left with a potentially complicated matrix element integrated over a complicated phase space. Often the phase space is transformed into something more suitable for computation and therefore we must include the appropriate Jacobian factor.

The Monte Carlo event generator samples the matrix element and integrates it using Monte Carlo methods, of which more information can be found in Appendix A. In general a crude estimate is performed at the start before event generation and this is used to decide the important parts of phase space and maximum weight to ensure that when events are generated, configurations are produced with the correct distribution. In general events are presented unweighted as Nature does not produce weighted events and it avoids complications with detector simulators. To produce the unweighted events, each momentum configuration can be accepted or rejected according to its probability, which is proportional to the maximum weight discovered during initialization.

We are still left with choices for the factorization scale and renormalization scale in the calculation. There are no correct methods for determining the correct scale for μ_F , but we are guided by intuition of our knowledge of logarithms of the hard process. If we have an s -channel scattering process with a scale Q^2 then generally we can set $\mu_F = \mu_R = Q^2$ and we can have a crude estimate of our errors by varying the factorization scale between $\frac{1}{2}\mu_F \rightarrow 2\mu_F$.

The PDFs are free for the user to decide and most event generators provide not only some inbuilt PDFs, but also an interface to the external LHAPDF package [48], who provide a plethora of PDFs from the various fitting groups through their website. In principle one may wish to use different PDFs for each beam, especially if one is scattering different particles but generally the same PDF set is used for both beam particles for processes at the LHC.

Final-state radiation

We first turn our attention to the final-state radiation, as this is simpler than the initial-state radiation, simply as we evolve away from the hard process without being constrained by what the final-state products should be.

For forward evolving time-like showers in `Herwig++` we make use of the variable [37]

$$\tilde{q}^2 = \frac{q_{\tilde{ij}}^2 - m_{\tilde{ij}}^2}{z(1-z)} \Big|_{q_i^2=m_i^2, q_j^2=m_j^2}, \quad (1.2.62)$$

and by the sub script \tilde{ij} we mean the parent of the splitting. We then find that

$$\tilde{q}^2 = \frac{-m_{\tilde{ij}}^2}{z(1-z)} + \frac{m_i^2}{z^2(1-z)} + \frac{m_j^2}{z(1-z)^2} - \frac{p_\perp^2}{z^2(1-z)^2} \quad (1.2.63)$$

which can be found from Eqn. 1.2.62, setting $q_{\tilde{ij}} = q_i + q_j$ and where

$$p_\perp = q_{i\perp} - z\tilde{q}_{\tilde{ij}\perp}. \quad (1.2.64)$$

We find that

$$\tilde{q}^2 \approx \frac{2E_{\tilde{ij}}^2(1 + \cos\theta_{\tilde{ij}})^2(1 - \cos\theta_{ij})}{(1 + \cos\theta_i)(1 + \cos\theta_j)}, \quad (1.2.65)$$

which for small angles gives

$$\tilde{q} = E_{\tilde{ij}}\theta_{\tilde{ij}}(1 - \mathcal{O}(\theta_x^2)). \quad (1.2.66)$$

We choose the starting scale for the shower based on the partons provided by the hard process in order to ensure colour coherence. The evolution will terminate at some point and we therefore need to choose what we mean by a resolvable emission. In `Herwig++` this is chosen with a parameterization based on a tuned parameter - a cut-off mass for the gluon. This now defines our new Sudakov form factor

$$\Delta(\tilde{q}, \tilde{q}_h) = \prod_{i,j} \Delta_{\tilde{ij} \rightarrow ij}(\tilde{q}, \tilde{q}_h) \quad (1.2.67)$$

where, in full

$$\Delta_{\tilde{ij} \rightarrow ij}(\tilde{q}, \tilde{q}_h) = \exp \left\{ - \int_{\tilde{q}}^{\tilde{q}_h} \frac{d\tilde{q}'^2}{\tilde{q}'^2} \int dz \frac{\alpha_S(z, \tilde{q}')}{2\pi} P_{\tilde{ij} \rightarrow ij}(z, \tilde{q}') \Theta(\mathbf{p}_\perp^2 > 0) \right\}. \quad (1.2.68)$$

The evolution from a scale \tilde{q}_h to \tilde{q} without a resolvable branching is given by our Sudakov form factor, $\Delta(\tilde{q}, \tilde{q}_h)$ and so we can generate the first branching of this scale by solving

$$\Delta(\tilde{q}, \tilde{q}_h) = \mathcal{R}, \quad (1.2.69)$$

where $\mathcal{R} \sim \text{Unif}[0, 1]$. This is solved by what is known as the veto algorithm, whereby we form a simple analytically integrable over-estimate of the integral and then we can solve for \tilde{q} . The veto algorithm is discussed in Appendix D.

To proceed with our evolution, we therefore solve [37]

$$\Delta_{\tilde{ij} \rightarrow ij}^{\text{over}}(\tilde{q}, \tilde{q}_h) = \exp \left\{ - \int_{\tilde{q}}^{\tilde{q}_h} \frac{d\tilde{q}'^2}{\tilde{q}'^2} \int_{z_-^{\text{over}}}^{z_+^{\text{over}}} dz \frac{\alpha_S^{\text{over}}(z, \tilde{q}')}{2\pi} P_{\tilde{ij} \rightarrow ij}^{\text{over}}(z) \right\} = \mathcal{R} \quad (1.2.70)$$

such that

$$\tilde{q}^2 = \tilde{q}_h^2 \mathcal{R}^{\frac{1}{r}} \quad (1.2.71)$$

where

$$r = \frac{\frac{d\tilde{q}'^2}{\tilde{q}'^2} \int_{z_-^{\text{over}}}^{z_+^{\text{over}}} dz \frac{\alpha_S^{\text{over}}(z, \tilde{q}')}{2\pi} P_{\tilde{ij} \rightarrow ij}^{\text{over}}(z)}{d \ln \tilde{q}^2}. \quad (1.2.72)$$

z is then solved from the over-estimate of its integral, $P_{\tilde{ij} \rightarrow ij}^{\text{over}}(z)$, by

$$z = I^{-1} [I(z_-^{\text{over}}) + \mathcal{R}' (I(z_-^{\text{over}}) - I(z_-^{\text{over}}))] \quad (1.2.73)$$

where $I(z)$ is the integral of $P_{\tilde{ij} \rightarrow ij}^{\text{over}}(z)$ over z , I^{-1} is its inverse and $\mathcal{R}' \sim \text{Unif}[0, 1]$.

We then reject the values of \tilde{q}_h and z if

- $\mathbf{p}_\perp < 0$;
- $\frac{\alpha_s(z, \tilde{q})}{\alpha_s^{\text{over}}} < \mathcal{R}_1$;
- $\frac{P_{\tilde{ij} \rightarrow ij}^{\text{over}}(z, \tilde{q})}{P_{\tilde{ij} \rightarrow ij}^{\text{over}}(z)} < \mathcal{R}_2$;

where again $\mathcal{R}_{1,2} \sim \text{Unif}[0, 1]$. If we reject \tilde{q} we set $\tilde{q}_h = \tilde{q}$ and repeat the process. In this way, we correctly distribute the variables \tilde{q} , z and ϕ describing the emission according to the Sudakov form factor [49]. The initial starting scales for the branching of the parent are determined to be $\tilde{q}_{hi} = z\tilde{q}$ and $\tilde{q}_{hj} = (1-z)\tilde{q}$, so that the ordering criteria moves us lower in \tilde{q} and therefore angular orders. The p_\perp of the splitting can then be found from Eqns. 1.2.63 (or Eqns. 1.2.75, depending on the

shower type). The azimuthal angle is chosen uniformly, so that we are neglecting spin correlations.

At the end of the shower each parton is left with a set of kinematic variables $(\tilde{q}, z, \phi, p_\perp)$. The progenitors of the shower are set to be on shell and α in the Sudakov decomposition set to one. We then proceed down the shower tree from the hard process calculating values of α for all partons by using the definition of z in Eqn 1.2.8 and momentum conservation *i.e.* $\alpha_{\tilde{ij}} = \alpha_i + \alpha_j$.

The q_\perp components can also be calculated in a similar way with the q_\perp of the progenitor being zero and using Eqn. 1.2.64. Then all we are left to calculate is β , which is calculated by setting the final state particles at the end of the shower on mass shell and iterating down the shower using the fact that $\beta_{\tilde{ij}} = \beta_i + \beta_j$. In this way we have reconstructed the momenta of our shower from the Sudakov basis.

Initial-state radiation

Initial-state radiation is similar to final state radiation, except we instead define

$$\tilde{q}^2 = \frac{m_i^2 - q_i^2}{(1-z)} \Bigg|_{q_{ij}^2 = m_{ij}^2, q_j^2 = m_j^2}, \quad (1.2.74)$$

which again using $q_{\tilde{ij}} = q_i + q_j$ gives

$$\tilde{q}^2 = \frac{-zm_{\tilde{ij}}^2}{(1-z)} + \frac{m_i^2}{(1-z)} + \frac{zm_j^2}{z(1-z)^2} - \frac{p_\perp^2}{(1-z)^2}, \quad (1.2.75)$$

which can be shown to have the same form as Eqn. 1.2.66.

In addition, for the initial-state radiation, ideally we want to evolve back from our hard process to the incoming hadron. We do this by being guided by the PDFs [18, 50, 51].

To see this consider $\mathcal{F}(t'; t, x)dt'$ to be the fraction of partons at t that came from the branching between $(t', t' + dt')$. Then, the number that did not branch is given by

$$\Pi(t_1, t_2, x) = 1 - \int_{t_1}^{t_2} \mathcal{F}(t'; t, x)dt'. \quad (1.2.76)$$

Now, we know from Eqn. 1.2.33 that

$$\begin{aligned} f(x, t_2) \mathcal{F}(t'; t, x) &= \int_{t_0}^t \frac{dt'}{t'} \frac{\Delta(t_2)}{\Delta(t')} \int \frac{dz}{z} \frac{\alpha_s}{2\pi} P(z) f\left(\frac{x}{z}, t\right) \\ &= dt \frac{\partial}{\partial t} \left[\frac{\Delta(t_2)}{\Delta(t')} f(x, t) \right], \end{aligned} \quad (1.2.77)$$

which is solved to give

$$\Pi(t_1, t_2, x) = \frac{\Delta(t_2) f(x, t_1)}{\Delta(t_1) f(x, t_2)}. \quad (1.2.78)$$

This allows us to evolve backwards from the hard process towards the incoming hadron, being guided by the PDFs.

We introduce a modified Sudakov form factor

$$\begin{aligned} \Delta_{\tilde{i}j \rightarrow ij}(x, \tilde{q}, \tilde{q}_h) &= \exp \left\{ - \int_{\tilde{q}}^{\tilde{q}_h} \frac{d\tilde{q}'^2}{\tilde{q}'^2} \int_x^{z_+} dz \frac{\alpha_S(z, \tilde{q}')}{2\pi} P_{\tilde{i}j \rightarrow ij}(z, \tilde{q}') \right. \\ &\quad \left. \times \frac{\frac{x}{z} f_{\tilde{i}j}\left(\frac{x}{z}, \tilde{q}'\right)}{x f_i(x, \tilde{q}')} \Theta(\mathbf{p}_\perp^2 > 0) \right\}, \end{aligned} \quad (1.2.79)$$

where the PDFs are now included in our definition of the Sudakov. In a similar way as to before solve

$$\Delta(x, \tilde{q}, \tilde{q}_h) = \mathcal{R} \quad (1.2.80)$$

using an over-estimate

$$\Delta_{\tilde{i}j \rightarrow ij}^{\text{over}}(x, \tilde{q}, \tilde{q}_h) = \exp \left\{ - \int_{\tilde{q}}^{\tilde{q}_h} \frac{d\tilde{q}'^2}{\tilde{q}'^2} \int_x^{z_+^{\text{over}}} dz \frac{\alpha_S^{\text{over}}}{2\pi} P_{\tilde{i}j \rightarrow ij}^{\text{over}}(z) \text{PDF}^{\text{over}}(z) \right\}, \quad (1.2.81)$$

where we have now included an overestimate of our PDF via

$$\text{PDF}^{\text{over}}(z) \geq \frac{\frac{x}{z} f_{\tilde{i}j}\left(\frac{x}{z}, \tilde{q}\right)}{x f_i(x, \tilde{q})}. \quad (1.2.82)$$

We solve in a similar way to above with one extra step in rejecting the values of \tilde{q}_h and z which is

$$\bullet \frac{\frac{x}{z} f_a\left(\frac{x}{z}, \tilde{q}'\right)}{\text{PDF}^{\text{over}}(z)} < \mathcal{R}_3;$$

with $\mathcal{R}_3 \sim \text{Unif}[0, 1]$.

We follow a similar reconstruction routine as in the final-state shower, except now it is the last backward branched parton, *i.e.* the one coming directly from the incoming hadron that is assumed to be on shell. We also have to start final-state showers from all necessary daughters that are produced in the backward evolution.

Hadronization

After the shower has finished the final-state partons must be hadronized. Hadronization is a model dependent process which is guided by physical principles. The hadronization model in **Herwig++** is based on the cluster model, which in turn is built on the concept of preconfinement [52].

Preconfinement shows that partons can be clustered at the cut-off scale in the shower into colour singlets that form an asymptotically universal invariant mass distribution. The idea behind this can be thought about in the large N_C limit where a gluon carries a colour and anti-colour line. During the shower process the flow of colour, via colour lines, is tracked. Although the colour is initially determined by the colour structure of the hard perturbative matrix elements, the emission of gluons during the shower introduces new colour structure.

At the end of the shower every colour line is connected to a colour partner. Colour singlets can then easily be formed by these lines. In practice this requires that at the end of the parton shower evolution all gluons are non-perturbatively split into quark-antiquark pairs. All the partons can then be formed into colour-singlet clusters which are assumed to be hadron precursors and decay according to phase space into the observed hadrons. There is a small fraction of heavy clusters for which this is not a reasonable approximation which are therefore first fissioned into lighter clusters.

The main advantage of this model, when coupled with the angular-ordered parton shower is that it has fewer parameters than the string model as implemented in the **PYTHIA** [49] event generator yet still gives a reasonable description of collider observables [42, 53]. Clearly such model dependency has to be fitted to data and there is therefore the concept of tuning the Monte Carlo event generator to observable data, often in a χ^2 minimization process. The tuning of a **Herwig++** will be presented later on in this thesis. Further details of the **Herwig++** hadronization process can be found in the **Herwig++** manual [37]. For the interested reader, **Pythia** uses the Lund string model of hadronization, whereby the colourlines between partons are viewed as strings [54, 55] under tension. **Sherpa** uses a cluster model also. A nice review of this, and other hadronization models can be found in Ref. [42].

1.3 Next-to-Leading Order Processes

As we have already seen, a next-to-leading order processes can be written as in Eqn. 1.1.56. We have also seen that there are two types of divergences, IR and UV. Clearly we would like to implement NLO processes in an event generator as it is another term in the perturbative series and we would expect to see an improvement in overall normalization of the cross section and the shape of distributions that are related to the first hard emission.

1.3.1 Numerical Integration

We have seen that the UV poles are removed by renormalization and that the IR poles cancel exactly between the real emission and the virtual contribution. In implementation, however, this cancellation of IR divergences is hard to implement numerically as we get large numerical components from both the virtual and the real contribution when integrating, that may become unstable. A solution is at hand though in the form of the dipole formalism.

The dipole formalism provides a way to deal with the poles appearing by cleverly subtracting and then adding an auxiliary component, $d\sigma^A$ to the NLO cross section [56–58]

$$\begin{aligned}\sigma^{\text{NLO}} &= \int_{n+1} \left[d\sigma^{\text{R}} - d\sigma^{\text{A}} \right] + \int_{n+1} d\sigma^{\text{A}} + \int_n d\sigma^{\text{V}} \\ &= \int_{n+1} \left[d\sigma^{\text{R}} - d\sigma^{\text{A}} \right] + \int_n \left[d\sigma^{\text{V}} + \int_1 d\sigma^{\text{A}} \right].\end{aligned}\quad (1.3.83)$$

The auxiliary component is chosen to match the point-wise singular behavior of the real contribution $d\sigma^{\text{R}}$ in d dimensions, therefore acting as a local counter-term for $d\sigma^{\text{R}}$. Importantly, $d\sigma^{\text{A}}$ is chosen to be analytically integrable in d dimensions over the phase-space regions that cause the soft and collinear divergences.

The choice of $d\sigma^{\text{A}}$ therefore means that $[d\sigma^{\text{R}} - d\sigma^{\text{A}}]$ is integrable over the $n + 1$ phase space, and the limit $\epsilon \rightarrow 0$ can safely be taken (as the divergent pieces have been subtracted). It also means that $\int_1 d\sigma^{\text{A}}$ contains all the poles that are required to cancel those of the virtual term $d\sigma^{\text{V}}$ therefore allowing that σ^{NLO} can be safely

integrated numerically in a Monte-Carlo procedure [58]. We can therefore write

$$\sigma^{\text{NLO}} = \int_{n+1} \left[\left(d\sigma^{\text{R}} \right)_{\epsilon=0} - \left(d\sigma^{\text{A}} \right)_{\epsilon=0} \right] + \int_n \left[d\sigma^{\text{V}} + \int_1 d\sigma^{\text{A}} \right]_{\epsilon=0} \quad (1.3.84)$$

where the first term under the $n + 1$ integral and second term under the n integral appearing in Eqn. 1.3.84 are integrable numerically in 4 dimensions.

It is worth noting at this point that no approximation has taken place. A “fake” cross section has been added and subtracted to regularise the integrals but the final answer for σ^{NLO} contains no approximation and therefore the total cross section contains no approximation.

The construction of the appropriate auxiliary cross section is clearly the key to implementing this method. Originally this was outlined using the dipole method for massless partons in Ref. [56] and then extended to massive partons in Ref. [57]. In both cases the auxiliary cross section is formulated by a sum of different contributions causing the IR singularities - the dipoles. As the IR singularities are caused by soft and collinear emissions from partons, the dipoles therefore encapsulate the description of these processes. The pair of partons are described by an emitter and a spectator, where it is the emitter’s kinematics that lead to the collinear singularities and both for the soft singularities.

The process of splitting may be thought of as the leading-order event occurring and producing the emitter and spectator. The emitter, naturally, then emits a parton (giving rise to an IR singularity). The spectator is used to balance momentum conservation [57] and contains information on the colour and spin correlations of the real cross section. The auxiliary cross section may then be written as

$$d\sigma^{\text{A}} = \sum_{\text{dipoles}} d\sigma^{\text{B}} \otimes dV_{\text{dipole}}, \quad (1.3.85)$$

where dV_{dipole} are obtained from QCD factorisation formulae in the IR limits and \otimes symbol is used to describe the fact that spin and colour correlations are preserved.

In writing Eqn. 1.3.85 there is an implicit assumption that the phase space can be factorised into one involving the n parton kinematics of the LO process and a process independent single particle phase space associated with the decay of the dipole. The single particle phase space therefore encapsulates the dependencies

that lead to the IR singularities. This factorisation allows the dipole term to be analytically integrable and the auxiliary cross section may then be written as

$$\int_{n+1} d\sigma^A = \sum_{\text{dipoles}} \int_n d\sigma^b \otimes \int_1 dV_{\text{dipole}} = \int_n [d\sigma^b \otimes \mathbf{I}], \quad (1.3.86)$$

where the \mathbf{I} is clearly defined as

$$\mathbf{I} = \sum_{\text{dipoles}} \int_1 dV_{\text{dipole}}. \quad (1.3.87)$$

We may therefore write the master equation for the NLO process as

$$\sigma^{\text{NLO}} = \int_{n+1} \left[\left(d\sigma^{\text{R}} \right)_{\epsilon=0} - \left(\sum_{\text{dipoles}} d\sigma^{\text{B}} \otimes dV_{\text{dipole}} \right)_{\epsilon=0} \right] + \int_n [d\sigma^{\text{V}} + d\sigma^{\text{B}} \otimes \mathbf{I}]_{\epsilon=0}, \quad (1.3.88)$$

which can be integrated safely in a numerical procedure.

1.3.2 POWHEG

We would like to interface this ability to calculate NLO cross sections in a stable numerical way with the parton shower to give us the total rate and hardest emission accurate to NLO. There are two major ways of doing this - the first is the MC@NLO method as described in Ref. [59] and the second is the POWHEG method first described in Ref. [60]. We will briefly outline the POWHEG method here and invite the reader to consult Ref. [59] for more information on MC@NLO.

In more detail, the NLO differential decay rate in the POWHEG [60,61] approach is

$$d\sigma = \overline{B}(\Phi_n) d\Phi_{\text{B}} \left[\Delta_{\text{R}}^{\text{NLO}}(p_T^{\text{min}}) + \Delta_{\text{R}}^{\text{NLO}}(p_T) \frac{R(\Phi_n, \Phi_1)}{B(\Phi_n)} d\Phi_1 \right], \quad (1.3.89)$$

where

$$\overline{B}(\Phi_n) = B(\Phi_n) + V(\Phi_n) + \int \left(R(\Phi_n, \Phi_1) - \sum_i D_i(\Phi_n, \Phi_1) \right) d\Phi_1. \quad (1.3.90)$$

Here $B(\Phi_n)$ is the leading-order Born differential decay rate, $V(\Phi_n)$ the regularized virtual contribution, $D_i(\Phi_n, \Phi_1)$ the counter terms regularizing the real emission and $R(\Phi_n, \Phi_1)$ the real emission contribution. The leading-order process has n outgoing partons, with associated phase space Φ_n . The virtual and Born contributions depend

only on this n -body phase space. The real emission phase space, Φ_{n+1} , is factorised into the n -body phase space and the phase space, Φ_1 , describing the radiation of an extra parton.

The Sudakov form factor in the POWHEG method is

$$\Delta_{\text{R}}^{\text{NLO}} = \exp \left[- \int d\Phi_1 \frac{R(\Phi_n, \Phi_1)}{B(\Phi_n)} \theta(k_{\perp}(\Phi_n, \Phi_1) - p_{\perp}) \right], \quad (1.3.91)$$

where $k_T(\Phi_n, \Phi_1)$ is the transverse momentum of the emitted parton.

In the POWHEG method, the hardest emission is calculated first and then the shower generates subsequent radiation. The reason for this is that the shower in **Herwig++** is not p_{\perp} ordered, but is instead ordered in angles. It is therefore possible to have soft emissions before the hardest in the shower, however, in the POWHEG approach, the first emission is meant to be the hardest.

The solution of this is the inclusion of what is called a vetoed truncated shower. Firstly, as mentioned, the hardest emission is generated and then mapped back into the shower variables $(\tilde{q}_h, z_h, \phi_h)$, where we use h to denote the hardest. Then, we start the shower as usual from the corresponding Born configuration and evolve down to a state \tilde{q}_h , vetoing any emission that has k_{\perp} greater than the hard p_{\perp} of the hardest emission. Then, the hardest emission is inserted into the shower, and the showering process continued from the \tilde{q}_h scale as usual, however, any emissions with k_{\perp} greater than the p_{\perp} of the hardest emission are again vetoed.

We therefore generate an event according to Eqn. 1.3.90 and the associated momenta. Then, we map the hardest emission into the variables used in the **Herwig++** shower. Then the truncated shower occurs, evolving down to the hardest emission, where care is made to ensure that the flavour of the branching does not change and then the hardest emission is inserted into the shower. The shower then restarts with $\tilde{q} = \tilde{q}_h$ and all other external legs are showered with the condition that $k_{\perp} < p_{\perp}$ [37, 62–64]. This method has been shown to preserve the leading-log accuracy of the shower in Ref. [61], in which also the NLO accuracy of Eqn. 1.3.90 is shown. We will use the POWHEG method later in this thesis.

Chapter 2

Jet Substructure and Boosted Higgs Studies

As mentioned in the introduction, Monte Carlo event generators contain a large number of both perturbative and non-perturbative parameters which are tuned to a wide range of experimental data. While significant effort has been devoted to the tuning of the parameters to produce a best fit there has been much less effort understanding the uncertainties in these results. Historically a best fit result, or at best a small number of tunes, are produced and used to predict observables making it difficult to assess the uncertainty on any prediction. The “Perugia” tunes [65,66] have addressed this by producing a range of tunes by varying specific parameters in the PYTHIA [49] event generator to produce an uncertainty.

Here we will make use of the Professor Monte Carlo tuning system [67] to give an assessment of the uncertainty from tuning by varying all the parameters simultaneously about the best-fit values by diagonalizing the error matrix. This then allows us to systematically estimate the uncertainty on any Monte Carlo prediction from the tuning of the event generator. We will illustrate this by considering the uncertainty on jet substructure searches for the Higgs boson at the LHC.

Jet substructure is set to play an important role in future studies of the Higgs boson at the LHC. As the LHC takes increasing amounts of data it will be vital to explore all channels for the Higgs boson decay and determine if the properties of the observed Higgs boson are consistent with the Standard Model. As we clearly see in

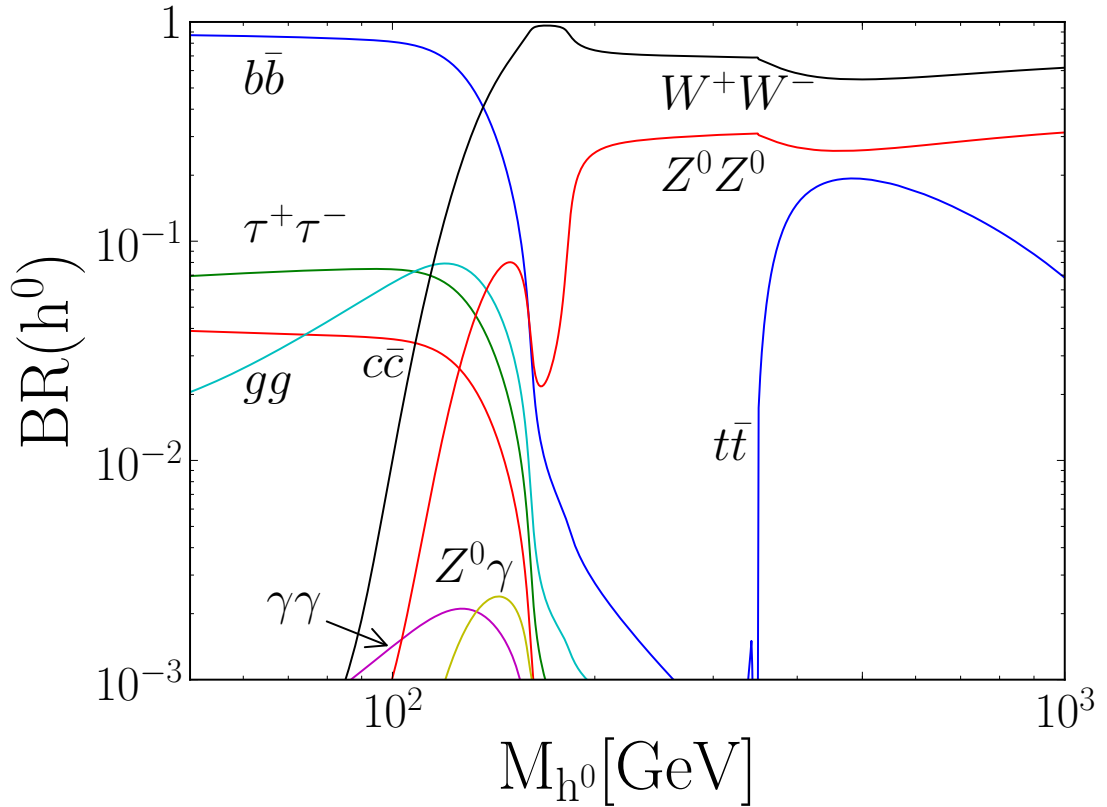


Figure 2.1: The branching ratio of the Higgs boson with respect to mass using results from Ref. [1].

Fig.2.1 the $h^0 \rightarrow b\bar{b}$ mode is the largest for a light Higgs boson mass, however, for many years it was believed that it would be difficult, if not impossible, to observe the dominant $h^0 \rightarrow b\bar{b}$ decay mode of a light Higgs boson. However, in recent years the use of jet substructure [68–83] offers the possibility of observing this mode.

Jet substructure for $h^0 \rightarrow b\bar{b}$ as a Higgs boson search channel, was first studied in Ref. [68] building on previous work of a heavy Higgs boson decaying to W^\pm bosons [79], high-energy WW scattering [84] and SUSY decay chains [85], and subsequently reexamined in Refs. [71, 78]. Recent studies at the LHC [86–88] have also shown this approach to be promising.

The study in Ref. [68] was carried out using the (FORTRAN) HERWIG 6.510 event generator [89, 90] together with the simulation of the underlying event using JIMMY 4.31 [91]. In order to allow the inclusion of new theoretical developments

and improvements in non-perturbative modelling a new simulation based on the same physics philosophy **Herwig++**, currently version 2.6 [37, 92], is now preferred for the simulation of hadron–hadron collisions.

Herwig++ includes both an improved theoretical description of perturbative QCD radiation, in particular for radiation from heavy quarks, such as bottom, together with improved non-perturbative modelling, especially of multiple parton–parton scattering and the underlying event. In FORTRAN HERWIG a crude implementation of the dead-cone effect [44] meant that there was no radiation from heavy quarks for evolution scales below the quark mass, rather than a smooth suppression of soft collinear radiation. In **Herwig++** an improved choice of evolution variable [93] allows evolution down to zero transverse momentum for radiation from heavy particles and reproduces the correct soft limit. There have also been significant developments of the multiple-parton scattering model of the underlying event [94, 95], including colour reconnections [96] and tuning to LHC data [97].

The background to jet substructure searches for the Higgs boson comes from QCD jets which mimic the decay of a boosted heavy particle. Although **Herwig++** has performed well in some early studies of jet substructure [88, 98, 99], it is important that we understand the uncertainties in our modelling of the background jets which lie at the tail of the jet mass distribution.

In addition we improve the simulation of Higgs boson decay by implementing the NLO corrections to Higgs boson decay to heavy quarks in the POWHEG [60, 61] formalism.

In the next section we outline the method of simulation for the $h^0 \rightarrow b\bar{b}$ decays and the POWHEG method. We then present our approach for the tuning of the parameters, which effect QCD radiation and hadronization, in **Herwig++** together with the results of our new tune. We then recap the key features of the Butterworth, Davison, Rubin and Salam (BDRS) jet substructure technique of Ref. [68]. This is followed by our results using both the leading and next-to-leading-order matrix elements in **Herwig++** with implementation of the next-to-leading-order Higgs boson decays and our estimate on the uncertainties.

We present an investigation of the dependence of searches for boosted Higgs

bosons using jet substructure on the perturbative and non-perturbative parameters of the Herwig++ Monte Carlo event generator. Values are presented for a new tune of the parameters of the event generator, together with an estimate of the uncertainties based on varying the parameters around the best-fit values.

2.1 Simulation of $h^0 \rightarrow b\bar{b}$ using the POWHEG Method

The POWHEG approach has already been covered briefly in the introduction to this thesis. Here, we will look at it in slightly more detail and with respect to the Higgs boson decay into a bottom quark anti-quark pair.

To recapitulate, the NLO differential decay rate in the POWHEG [60] approach is

$$d\sigma = \bar{B}(\Phi_n) d\Phi_B \left[\Delta_R^{\text{NLO}}(p_T^{\text{min}}) + \Delta_R^{\text{NLO}}(p_T^{\text{min}}) \frac{R(\Phi_n, \Phi_1)}{B(\Phi_n)} d\Phi_1 \right], \quad (2.1.1)$$

where

$$\bar{B}(\Phi_n) = B(\Phi_n) + V(\Phi_n) + \int \left(R(\Phi_n, \Phi_1) - \sum_i D_i(\Phi_n, \Phi_1) \right) d\Phi_1. \quad (2.1.2)$$

Here $B(\Phi_n)$ is the leading-order Born differential decay rate, $V(\Phi_n)$ the regularized virtual contribution, $D_i(\Phi_n, \Phi_1)$ the counter terms regularizing the real emission and $R(\Phi_n, \Phi_1)$ the real emission contribution. The leading-order process has n outgoing partons, with associated phase space Φ_n . The virtual and Born contributions depend only on this n -body phase space. The real emission phase space, Φ_{n+1} , is factorised into the n -body phase space and the phase space, Φ_1 , describing the radiation of an extra parton.

In order to implement the decay of the Higgs boson in the POWHEG scheme in Herwig++ we need to generate the Born configuration according to Eqn. 2.1.2 and the subsequent hardest emission according to Eqn. 1.3.91. The generation of the truncated and vetoed parton showers from these configurations then proceeds as described in Refs. [37, 62–64].

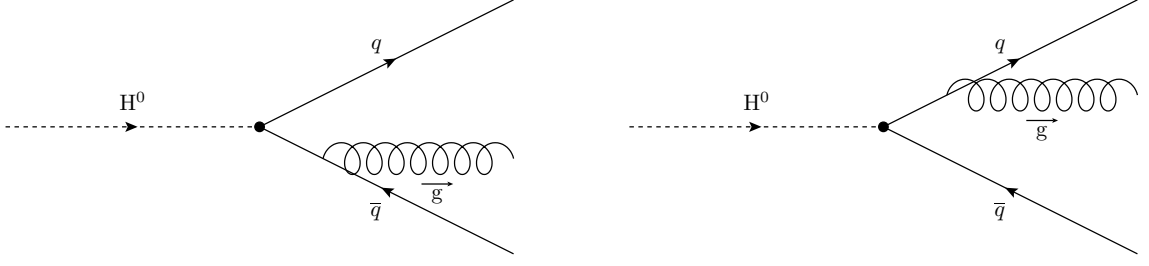


Figure 2.2: The two real-emission processes contributing to the NLO decay rate.

The virtual contribution for $h^0 \rightarrow b\bar{b}$ was calculated in Ref. [100]. The corresponding real emission contribution, see Fig. 2.2, is

$$|\mathcal{M}_R|^2 = |\mathcal{M}_2|^2 \frac{C_F 8\pi\alpha_s}{M_H^2(1-4\mu^2)} \left[2 + \frac{1-x_q}{1-x_{\bar{q}}} + \frac{(8\mu^4 - 6\mu^2 + 1)}{(1-x_q)(1-x_{\bar{q}})} - 2(1-4\mu^2) \frac{1}{1-x_q} - 2\mu^2(1-4\mu^2) \frac{1}{(1-x_q)^2} + (x_q \leftrightarrow x_{\bar{q}}) \right], \quad (2.1.3)$$

where \mathcal{M}_2 is the leading-order matrix element, m_q is the mass of the bottom quark, M_H is the mass of the Higgs boson, $\mu = \frac{m_q}{M_H}$ and $x_i = \frac{2E_i}{M_H}$. We use the Catani-Seymour subtraction scheme [57] where the counter terms are

$$D_i = C_F \frac{8\pi\alpha_S}{s} |\mathcal{M}_2|^2 \times \frac{1}{1-x_j} \left\{ \frac{2(1-2\mu^2)}{2-x_i-x_j} - \sqrt{\frac{1-4\mu^2}{x_j^2-4\mu^2}} \frac{x_j-2\mu^2}{1-2\mu^2} \left[2 + \frac{x_i-1}{x_j-2\mu^2} + \frac{2\mu^2}{1-x_j} \right] \right\}, \quad (2.1.4)$$

where for D_i , i is the emitting parton and j is the spectator parton. In practice, as the counter terms can become negative in some regions, we use

$$R(\Phi_n, \Phi_1) - \sum_i D_i(\Phi_n, \Phi_1) = \sum_i \left[\frac{R(\Phi_n, \Phi_1) |D_i(\Phi_n, \Phi_1)|}{\sum_j |D_j(\Phi_n, \Phi_1)|} - D_i(\Phi_n, \Phi_1) \right]. \quad (2.1.5)$$

We have also regulated singularities in the virtual term $V(\Phi_n)$ with the integrated counter terms from the Catani-Seymour subtraction scheme allowing us to generate the Born configuration according to $\bar{B}(\Phi_n)$.

The hardest emission for each leg is generated according to

$$\Delta_{iR}^{\text{NLO}} = \exp \left[- \frac{M_H^2}{16\pi^2(1-4\mu^2)^{\frac{1}{2}}} \times \int dx_1 dx_2 d\phi \frac{R(\Phi_{n+1})}{B(\Phi_n)} \frac{|D_i|}{\sum_j |D_j|} \theta(k_T(\Phi_n, \Phi_1) - p_T) \right]. \quad (2.1.6)$$

However, this form is not suitable for the generation of the hardest emission. Instead we perform a Jacobian transformation and use the transverse momentum, p_T , rapidity, y , and azimuthal angle, ϕ , of the radiated gluon to define the phase space Φ_1 .

The momenta of the Higgs boson decay products are

$$p_1 = \frac{M_H}{2} \left(x_1; -x_\perp \cos(\phi), -x_\perp \sin(\phi), \pm \sqrt{x_1^2 - x_\perp^2 - 4\mu^2} \right), \quad (2.1.7a)$$

$$p_2 = \frac{M_H}{2} \left(x_2; 0, 0, -\sqrt{x_2^2 - 4\mu^2} \right), \quad (2.1.7b)$$

$$p_3 = \frac{M_H}{2} \left(x_3; x_\perp \cos(\phi), x_\perp \sin(\phi), \pm \sqrt{x_3^2 - x_\perp^2} \right), \quad (2.1.7c)$$

where partons 1, 2, 3 are the radiating bottom quark, spectator antibottom quark and radiated gluon, respectively. The energy fractions $x_i = \frac{2E_i}{M_H}$ and $x_\perp = \frac{2p_T}{M_H}$. Using the conservation of momentum in the z -direction and $x_1 + x_2 + x_3 = 2$ gives

$$x_\perp^2 = (2 - x_1 - x_2)^2 - \frac{(-2 + 2x_1 + 2x_2 - x_2x_1 - x_2^2)^2}{x_2^2 - 4\mu^2}. \quad (2.1.8)$$

Together with the definition, $x_3 = x_\perp \cosh y$, we obtain the Jacobian

$$\left| \frac{\partial x_1 \partial x_2}{\partial p_T \partial y} \right| = \frac{x_\perp}{M_H} \frac{x_\perp (x_2^2 - 4\mu^2)^{\frac{3}{2}}}{(x_1 x_2 - 2\mu^2(x_1 + x_2) + x_2^2 - x_2)}, \quad (2.1.9)$$

for the transformation of the radiation variables.

We can then generate the additional radiation according to Eqn. 2.1.6 using the veto algorithm [49]. To achieve this we use an overestimate of the integrand in the Sudakov form factor, $f(p_T) = \frac{c}{p_T}$, where c is a suitable constant. We first generate an emission according to

$$\Delta_R^{\text{over}}(p_T) = \exp \left[- \int_{p_T}^{p_T^{\text{max}}} \int_{y_{\text{min}}}^{y_{\text{max}}} d p_T d y \frac{c}{p_T} \right], \quad (2.1.10)$$

using this overestimate, where $y_{\max} = \cosh^{-1} \left(\frac{M_H}{2p_T^{\min}} \right)$, $y_{\min} = -y_{\max}$, p_T^{\max} is the maximum possible transverse momentum of the gluon and p_T^{\min} is a parameter set in the model, taken to be 1 GeV.

The trial value of the transverse momentum is obtained by solving $\mathcal{R} = \Delta_R^{\text{over}}$, where \mathcal{R} is a random number in $[0, 1]$, *i.e.*

$$p_T = p_T^{\max} \mathcal{R}^{\frac{1}{c(y_{\max} - y_{\min})}}. \quad (2.1.11)$$

Once the trial p_T has been generated, y and ϕ are also generated uniformly between $[y_{\min}, y_{\max}]$ and $[0, 2\pi]$, respectively. The energy fractions of the partons are obtained using the definition $x_3 = x_{\perp} \cosh y$,

$$x_1 = \frac{1}{2(x_3 - 1) - \frac{x_{\perp}^2}{2}} \left\{ 3x_3 - 2 + \frac{x_{\perp}^2}{2}x_3 - x_{\perp}^2 - x_3^2 \right. \\ \left. \pm \sqrt{(x_3^2 - x_{\perp}^2)((x_3 - 1)(4\mu^2 + x_3 - 1) - \mu^2 x_{\perp}^2)} \right\}, \quad (2.1.12)$$

and x_2 using energy conservation. As there are two solutions for x_1 both solutions must be kept and used to calculate the weight for a particular trial p_T . The signs of the z -components of the momenta are fixed by the sign of the rapidity and momentum conservation. Any momentum configurations outside of the physically allowed phase space are rejected and a new set of variables generated. The momentum configuration is accepted with a probability given by the ratio of the true integrand to the overestimated value. If the configuration is rejected, the procedure continues with p_T^{\max} set to the rejected p_T until the trial value of p_T is accepted or falls below the minimum allowed value, p_T^{\min} . This procedure generates the radiation variables correctly as shown in Ref. [49].

This procedure is used to generate a trial emission from both the bottom and antibottom. The hardest potential emission is then selected which correctly generates events according to Eqn. 2.1.6 using this competition algorithm.

As a first check on our results, we can check the jet merging scale, where the jet goes from a $n \rightarrow n + 1$ jet event, comparing the Herwig++ default mode for the decays and the new POWHEG implementation. The e^+e^- jet measure, for the

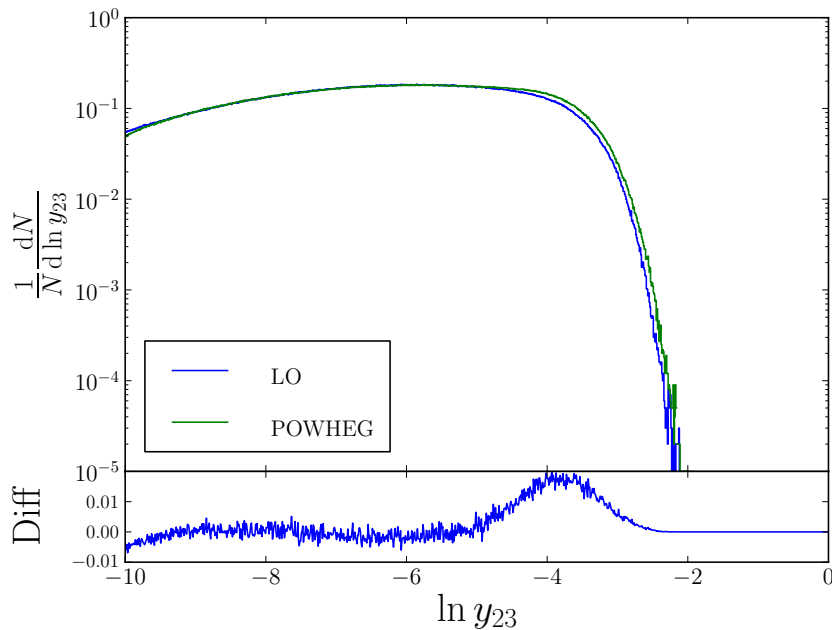


Figure 2.3: The scale at which we go from a two to a three jet event for Higgs boson decays using the LO and new POWHEG implementation in Herwig++.

simulated $e^+e^- \rightarrow h^0 \rightarrow b\bar{b}$ process is defined as [5]¹.

$$y_{ij} = \frac{2\min(E_i^2, E_j^2)(1 - \cos\theta_{ij})}{Q^2}. \quad (2.1.13)$$

We would clearly expect to see more three jet events with the POWHEG method, and this is seen in Fig. 2.1 where the POWHEG method causes the scale at which we go from a two to a three jet event to be higher than in the LO case.

2.2 Tuning Herwig++

Any jet substructure analysis is sensitive to changes in the simulation of initial- and final-state radiation, and hadronization. In particular the non-perturbative nature of the phenomenological hadronization model means there are a number of parameters which are tuned to experimental results. We have already seen that Herwig++

¹ More information on jet algorithms and jets in general can be found in Appendix B.

uses an improved angular-ordered parton shower algorithm [37, 93] to describe perturbative QCD radiation together with a cluster hadronization model [37, 53].

To tune Herwig++, and investigate the dependency of observables on the shower and hadronization parameters, the Professor Monte Carlo tuning system [67] was used. Professor uses the Rivet analysis framework [101] and a number of simulated event samples, with different Monte Carlo parameters, to parameterise the dependence of each observable² used in the tuning on the parameters of the Monte Carlo event generator. A heuristic chi-squared function

$$\chi'^2(\mathbf{p}) = \sum_{\mathcal{O}} w_{\mathcal{O}} \sum_{b \in \mathcal{O}} \frac{(f^b(\mathbf{p}) - \mathcal{R}_b)^2}{\Delta_b^2}, \quad (2.2.14)$$

is constructed where \mathbf{p} is the set of parameters being tuned, \mathcal{O} are the observables used each with weight $w_{\mathcal{O}}$, b are the different bins in each observable distribution with associated experimental measurement \mathcal{R}_b , error Δ_b and Monte Carlo prediction $f^b(\mathbf{p})$. Weighting of those observables for which a good description of the experimental result is particularly important is used in most cases. The parameterisation of the event generator response, $f(\mathbf{p})$, is then used to minimize the χ'^2 and find the optimum parameter values.

There are ten main free parameters which affect the shower and hadronization in Herwig++. These are shown in Table 2.1 along with their default values and allowed ranges.

The gluon mass, `GluonMass`, is required to allow the non-perturbative decay of gluons into $q\bar{q}$ pairs and controls the energy release in this process. `PSplitLight`, `ClPowLight` and `ClMaxLight` control the mass distributions of the clusters produced during the fission of heavy clusters. `ClSmrLight` controls the smearing of the direction of hadrons containing a (anti)quark from the perturbative evolution about the direction of the (anti)quark. `AlphaMZ` is strong coupling at the Z^0 boson mass and controls the amount of QCD radiation in the parton shower, while `Qmin` controls the infrared behaviour of the strong coupling. `pTmin` is the minimum allowed transverse momentum in the parton shower and controls the amount of radiation and the scale

²Normally this is either an observation such as a multiplicity or a bin in a measured distribution.

Parameter	Default Value	Allowed Range	Scanned Range	Optimum Value
<code>Qmin</code>	0.935	≥ 0	0.500 – 2.500	Fixed at default
<code>GluonMass</code>	0.95	0 – 1	0.75 – 1.00	Fixed at default
<code>ClSmrLight</code>	0.78	0 – 2	0.30 – 3.00	Fixed at default
<code>ClPowLight</code>	1.28	0 – 10	0.50 – 4.00	Fixed at default
<code>pTmin</code>	1.00	≥ 0	0.50 – 1.50	0.88
<code>AlphaMZ</code>	0.12	≥ 0	0.10 – 0.12	0.11
<code>ClMaxLight</code>	3.25	0 – 10	3.00 – 4.20	3.60
<code>PSplitLight</code>	1.20	0 – 10	1.00 – 2.00	0.90
<code>PwtDIquark</code>	0.49	0 – 10	0.10 – 0.50	0.33
<code>PwtSquark</code>	0.68	0 – 10	0.50 – 0.80	0.64

Table 2.1: The ten parameters to which the jet substructure is most sensitive with their default values, the allowed range of these values in **Herwig++**, the range scanned over and the new optimum value found from minimizing χ'^2 .

at which the perturbative evolution terminates. `PwtDIquark` and `PwtSquark` are the probabilities of selecting a diquark-antidiquark or $s\bar{s}$ quark pair from the vacuum during cluster splitting, and affect the production of baryons and strange hadrons respectively.

Previous experience of tuning **Herwig++** has found that `Qmin`, `GluonMass`, `ClSmrLight`, and `ClPowLight` to be flat, and so it was chosen to fix these at their default values [37].

To determine the allowed variation of these parameters **Professor** was used to tune the variables in Table 2.1 to the observables and weights found in Tables 2.2, 2.3, 2.4 and 2.5. The dependence of χ'^2 on the various parameters, about the minimum χ'^2 value, is then diagonalized.

The variation of the parameters along the eigenvectors in parameter space obtained corresponding to a certain change, $\Delta\chi'^2$, in χ'^2 can then be used to predict the uncertainty in the Monte Carlo predictions for specific observables.

In theory, if the χ'^2 measure for the parameterised generator response is actually distributed as a true χ^2 , then a change in the goodness of fit of one will correspond to a one sigma deviation from the minima, *i.e.* the best tune. In practice, even the

Observable	Weight	Observable	Weight
$K^{*\pm}(892)$ spectrum	1.0	Λ^0 spectrum	1.0
ρ spectrum	1.0	π^0 spectrum	1.0
$\omega(782)$ spectrum	1.0	p spectrum	1.0
Ξ^- spectrum	1.0	η' spectrum	1.0
$K^{*0}(892)$ spectrum	1.0	$\Xi^0(1530)$ spectrum	1.0
ϕ spectrum	1.0	π^\pm spectrum	1.0
$\Sigma^\pm(1385)$ spectrum	1.0	η spectrum	1.0
γ spectrum	1.0	K^0 spectrum	1.0
K^\pm spectrum	1.0		

Table 2.2: Observables used in the tuning and associated weights for observables taken from [6].

Observable	Weight
Sphericity, S	1.0
Energy-energy correlation, EEC	1.0
Aplanarity, A	2.0
Mean out-of-plane p_\perp in GeV w.r.t. thrust axes vs. x_p	1.0
Mean charged multiplicity	150.0
Mean p_\perp in GeV vs. x_p	1.0
Planarity, P	1.0
Thrust major, M	1.0
Oblateness = $M - m$	1.0
Out-of-plane p_\perp in GeV w.r.t. sphericity axes	1.0
D parameter	1.0
1 - Thrust	1.0
Out-of-plane p_\perp in GeV w.r.t. thrust axes	1.0
Log of scaled momentum, $\log(1/x_p)$	1.0
In-plane p_\perp in GeV w.r.t. sphericity axes	1.0
In-plane p_\perp in GeV w.r.t. thrust axes	1.0
Thrust minor, m	2.0
C parameter	1.0
Scaled momentum, $x_p = p / p_{\text{beam}} $	1.0

Table 2.3: Observables used in the tuning and associated weights for observables taken from [2].

Observable	Weight	Observable	Weight
Mean $\rho^0(770)$ multiplicity	10.0	Mean $\chi_{c1}(3510)$ multiplicity	10.0
Mean $\Delta^{++}(1232)$ multiplicity	10.0	Mean D^+ multiplicity	10.0
Mean $K^{*+}(892)$ multiplicity	10.0	Mean Σ^+ multiplicity	10.0
Mean Σ^0 multiplicity	10.0	Mean $f_1(1285)$ multiplicity	10.0
Mean Λ_b^0 multiplicity	10.0	Mean $f_2(1270)$ multiplicity	10.0
Mean K^+ multiplicity	10.0	Mean $J/\psi(1S)$ multiplicity	10.0
Mean $\Xi^0(1530)$ multiplicity	10.0	Mean B_u^+ multiplicity	10.0
Mean $\Lambda(1520)$ multiplicity	10.0	Mean B^* multiplicity	10.0
Mean $D_s^{*+}(2112)$ multiplicity	10.0	Mean Λ_c^+ multiplicity	10.0
Mean $\Sigma^-(1385)$ multiplicity	10.0	Mean D^0 multiplicity	10.0
Mean $f_1(1420)$ multiplicity	10.0	Mean $f_2'(1525)$ multiplicity	10.0
Mean $\phi(1020)$ multiplicity	10.0	Mean Σ^\pm multiplicity	10.0
Mean $K_2^{*0}(1430)$ multiplicity	10.0	Mean D_{s2}^+ multiplicity	10.0
Mean Ω^- multiplicity	10.0	Mean $K^{*0}(892)$ multiplicity	10.0
Mean $\Sigma^\pm(1385)$ multiplicity	10.0	Mean Σ^- multiplicity	10.0
Mean $\psi(2S)$ multiplicity	10.0	Mean π^+ multiplicity	10.0
Mean $D^{*+}(2010)$ multiplicity	10.0	Mean $f_0(980)$ multiplicity	10.0
Mean B^* multiplicity	10.0	Mean $\Sigma^+(1385)$ multiplicity	10.0
Mean π^0 multiplicity	10.0	Mean D_s^+ multiplicity	10.0
Mean η multiplicity	10.0	Mean p multiplicity	10.0
Mean $a_0^+(980)$ multiplicity	10.0	Mean B_s^0 multiplicity	10.0
Mean D_{s1}^+ multiplicity	10.0	Mean K^0 multiplicity	10.0
Mean $\rho^+(770)$ multiplicity	10.0	Mean B^+, B_d^0 multiplicity	10.0
Mean Ξ^- multiplicity	10.0	Mean Λ multiplicity	10.0
Mean $\omega(782)$ multiplicity	10.0	Mean $\eta'(958)$ multiplicity	10.0
Mean $\Upsilon(1S)$ multiplicity	10.0		

Table 2.4: Multiplicities used in the tuning and associated weights for observables taken from [7].

Observable	Weight
b quark fragmentation function $f(x_B^{\text{weak}})$	7.0
Mean of b quark fragmentation function $f(x_B^{\text{weak}})$	3.0

Table 2.5: Observables used in the tuning and associated weights for observables taken from [8].

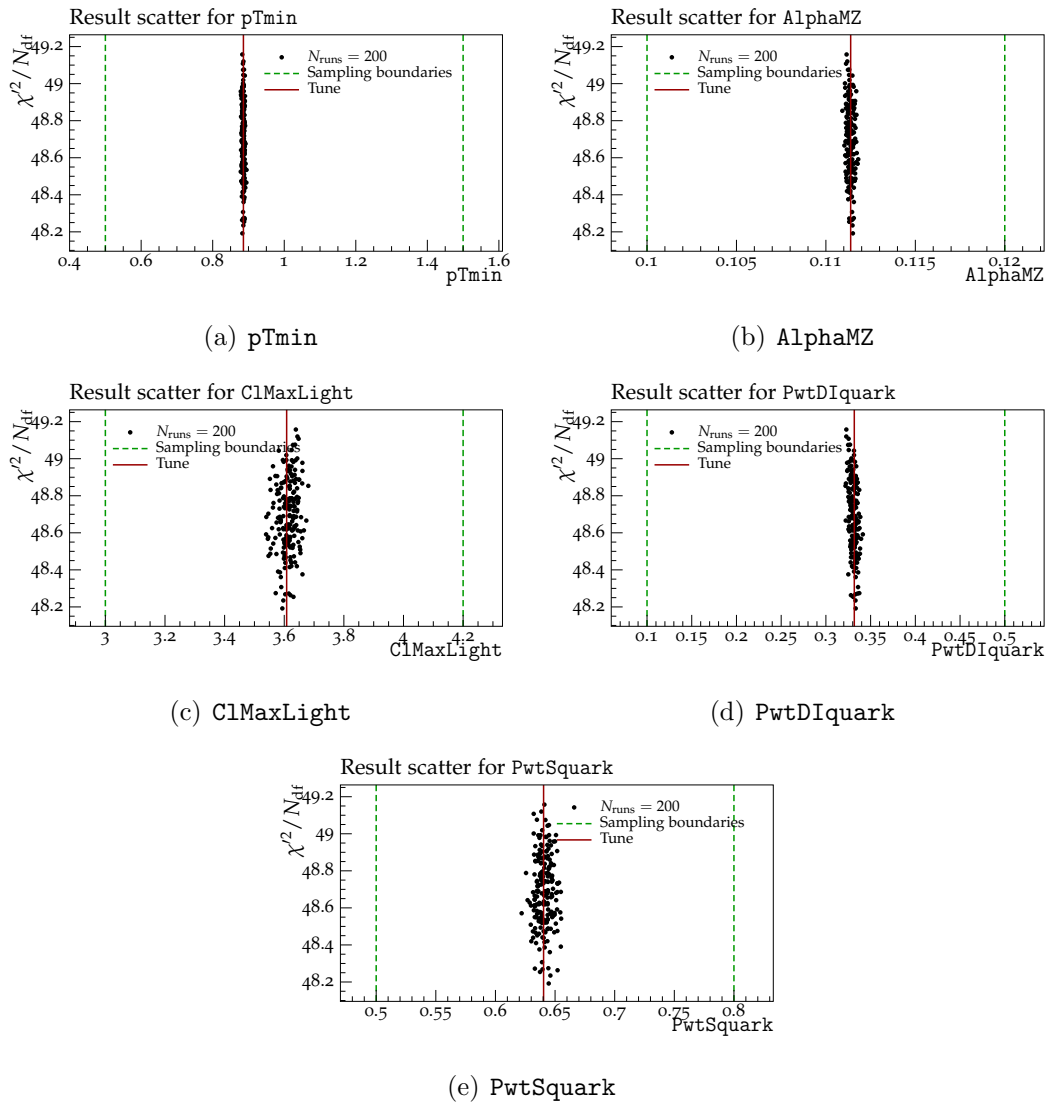


Figure 2.4: The χ^2/N_{df} distributions for the parameters that were varied from their default values whilst determining the error tune. The scatter of the results gives a representation of the systematics of tuning procedure.

best tune does not fit the data ideally and nor is the χ'^2 measure actually distributed according to a true χ^2 distribution. This means that one cannot just use Professor to vary the parameters about the minima to a given deviation in the χ'^2 measure without using some subjective opinion on the quality of the results.

We simulated one thousand event samples with different randomly selected values of the parameters we were tuning. Six hundred of these were used to interpolate the generator response. All the event samples were used to select two hundred samples

randomly two hundred times in a bootstrapping type process in order to assess the systematics of the interpolation and tuning procedure. A cubic interpolation of the generator response was used as this has been shown to give a good description of the Monte Carlo behaviour in the region of best generator response [67]. The parameters were varied between values shown in Table 2.1. The quality of the interpolation was checked by comparing the χ'^2/N_{df} , where N_{df} is the number of observable bins used in the tune, in the allowed parameter range on a parameter by parameter basis for the observables by comparing the interpolation response with actual generator response at the simulated parameter values. Bad regions were removed and the interpolation repeated leaving a volume in the 5-dimensional parameter space where the interpolation worked well.

Fig. 2.4 shows the χ'^2/N_{df} distributions for two hundred tunes based on two hundred randomly selected event samples points for the cubic interpolation. The spread of these values gives an idea of the systematics of the tuning process showing that we have obtained a good fit for our parameterisation of the generator response.

The line indicates the tune which is based on a cubic interpolation from six hundred event samples. It is this interpolation which was used to vary χ'^2 about the minimum to assess the uncertainty on the measured distributions. During the tune it was discovered that `PSplitLight` was relatively insensitive to the observables used in the tune. As such, `PSplitLight` was fixed at the default value of 1.20 during the tune and subsequent χ'^2 variation.

`Professor` was used to vary χ'^2 about the minimum value, as described above, determining the allowed range for the parameters. As five parameters were eventually varied, there are 10 new sample points - one “+” and one “-” along each eigenvector direction in parameter space.

We follow the example set by the parton distribution function (PDF) fitting groups in determining how much to allow χ'^2 to vary. Our situation is different to the PDF fitters in that we are using leading-order calculations with leading-log accuracy in the parton shower, where they fit to next-to-leading order calculations which gives better overall agreement with the observables used. Generally, PDF groups fit to fully inclusive variables, where as we have fitted to more exclusive processes and by

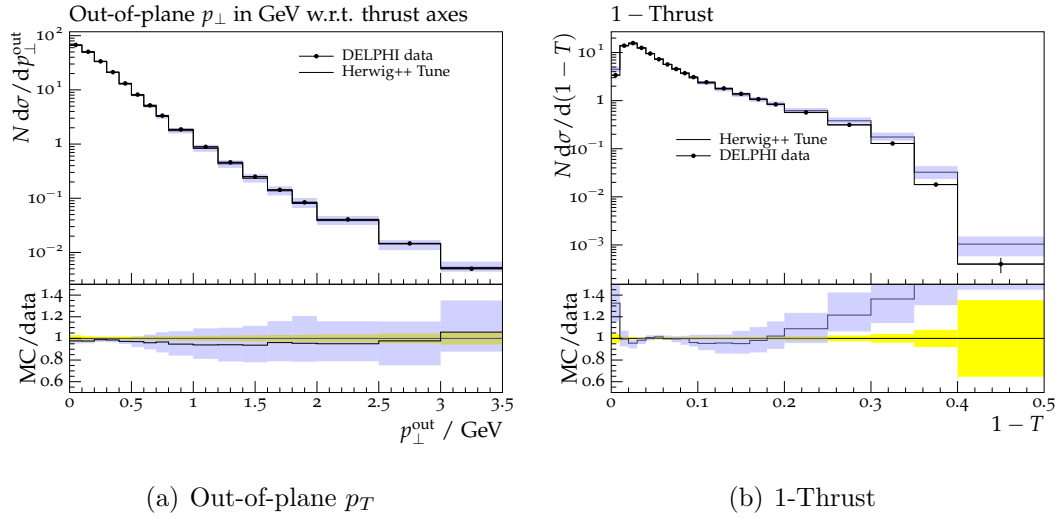


Figure 2.5: Results from the DELPHI [2] analysis of out-of-plane p_T with-respect-to the thrust axis and 1-thrust showing the new tune and the envelopes corresponding to a change in $\Delta\chi'^2/N_{\text{df}} = 5$.

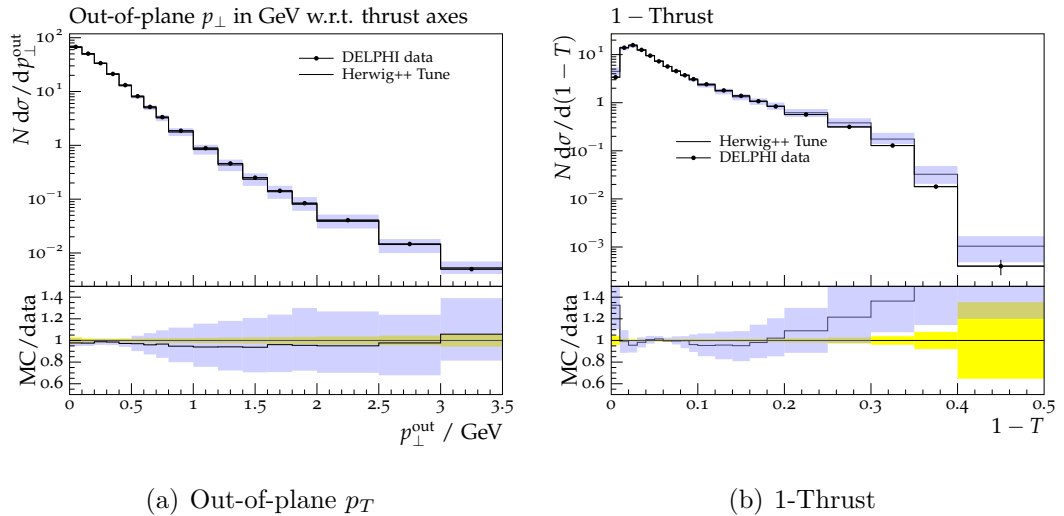


Figure 2.6: Results from the DELPHI [2] analysis of out-of-plane p_T with-respect-to the thrust axis and 1-thrust showing the new tune and the envelopes corresponding to a change in $\Delta\chi'^2/N_{\text{df}} = 10$.

nature, these are more model dependent in particular hadronization effects.

In Refs. [102, 103] these issues are explored in terms of PDFs and the allowed

variation is related to a tolerance parameter T , where

$$\Delta\chi'_{\text{global}} \leq T^2. \quad (2.2.15)$$

A tolerance parameter of $T \approx 10$ to 15 is generally chosen for the PDF groups, where they are fitting to around 1300 data points. As our fit is likely to have a higher χ^2 than their fit due to the aforementioned reasons, and that we fit to a greater number of observables, we will have a higher tolerance parameter.

In our fit, we have 1665 degrees-of-freedom and we examined various changes in χ'^2 , whilst considering the effects of the precision data from LEP. A variation of $\Delta\chi'^2/N_{\text{df}} = 5$, equivalent to $T \approx 90$ seems, subjectively to keep the LEP data within reasonable limits while a variation of $\Delta\chi'^2/N_{\text{df}} = 10$, *i.e.* $T \approx 130$ is too large. Anything less than $T \approx 40$ had very little variation and was therefore deemed inappropriate. The values for both $\Delta\chi'^2/N_{\text{df}} = 5$ and $\Delta\chi'^2/N_{\text{df}} = 10$ are shown in Tables 2.6 and Tables 2.7 respectively.

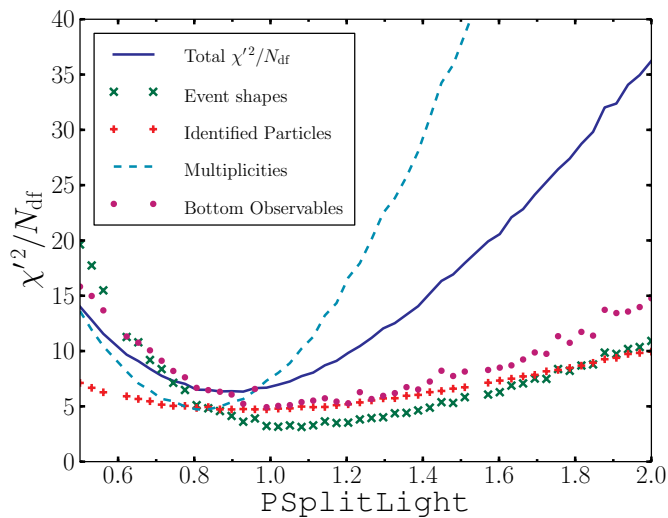


Figure 2.7: A scan of `PSplitLight` using the internal `Herwig++` tuning system with the other parameters fixed at their new tuned value. From the total χ'^2/N_{df} we see that a value of 0.90 for `PSplitLight` is favoured at the new tuned parameters driven by the multiplicities.

The `Professor` tune was then compared with the internal `Herwig++` tuning procedure [37] as not all analyses that are in the internal `Herwig++` tuning system are

Parameter	Direction									
	1		2		3		4		5	
	+	-	+	-	+	-	+	-	+	-
pTmin	0.88	0.88	0.88	0.88	0.84	0.93	0.87	0.90	0.89	0.87
AlphaMZ	0.11	0.11	0.10	0.12	0.12	0.11	0.12	0.11	0.12	0.11
ClMaxLight	3.61	3.61	3.61	3.61	3.60	3.62	3.66	3.55	3.54	3.67
PwtDIquark	0.46	0.23	0.33	0.33	0.33	0.33	0.33	0.33	0.33	0.33
PwtSquark	0.64	0.64	0.64	0.64	0.64	0.64	0.62	0.67	0.51	0.78

Table 2.6: The five directions corresponding to the error tune for a $\Delta\chi'^2/N_{\text{df}} = 5$ and the values the parameters take in each direction.

Parameter	Direction									
	1		2		3		4		5	
	+	-	+	-	+	-	+	-	+	-
pTmin	0.88	0.88	0.88	0.88	0.82	0.95	0.86	0.90	0.89	0.87
AlphaMZ	0.11	0.11	0.10	0.12	0.12	0.10	0.12	0.10	0.12	0.11
ClMaxLight	3.61	3.61	3.61	3.61	3.59	3.63	3.68	3.52	3.52	3.70
PwtDIquark	0.51	0.19	0.33	0.33	0.33	0.33	0.33	0.33	0.33	0.33
PwtSquark	0.64	0.64	0.64	0.64	0.65	0.64	0.61	0.68	0.46	0.84

Table 2.7: The five directions corresponding to the error tune for a $\Delta\chi'^2/N_{\text{df}} = 10$ and the values the parameters take in each direction.

available in Rivet and subsequently accessible to Professor. Looking at Fig. 2.7 it is found that `PSplitLight` at a value of 0.90 is favoured and gives a significant reduction in the χ'^2/N_{df} . It was therefore decided to use the values obtained from minimisation procedure, but using the value of 0.90 for `PSplitLight` to maintain a good overall description of the data. The new minima for the QCD parameters are summarized in the Table 2.1. Examples of the new tune and the uncertainty band are shown in Figs. 2.5 and 2.6 for the out-of-plane transverse momentum and thrust measured by DELPHI [2].

These error tune values can now be used to predict the uncertainty from the tuning of the shower parameters on any observable. In the next section we will present an example of using these tunes to estimate the uncertainty on the predictions for

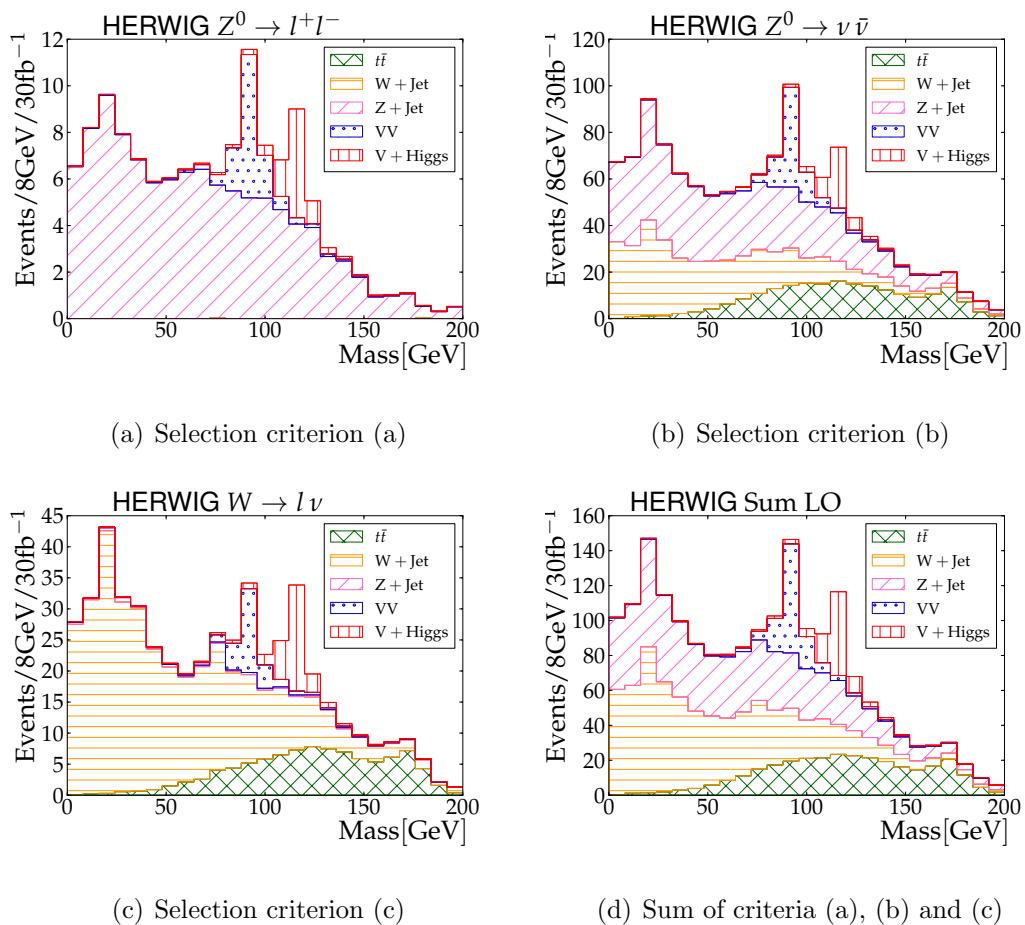


Figure 2.8: Results for the reconstructed Higgs boson mass distribution using HERWIG leading-order matrix elements for top quark pair production, and the production of W^\pm and Z^0 bosons in association with a hard jet. A SM Higgs boson was assumed with a mass of 115 GeV.

searches for the Higgs boson using the BDRS jet substructure method.

2.3 Jet Substructure of Boosted Higgs

The analysis of Ref. [68] uses a number of different channels for the production of the Higgs boson decaying to $b\bar{b}$ in association with an electroweak gauge boson, *i.e.* the production of $h^0 Z^0$ and $h^0 W^\pm$. Ref. [68] uses the fact that the Higgs boson predominantly decays to $b\bar{b}$ in a jet substructure analysis to extract the signal of a boosted Higgs boson above the various backgrounds. Their study found that the

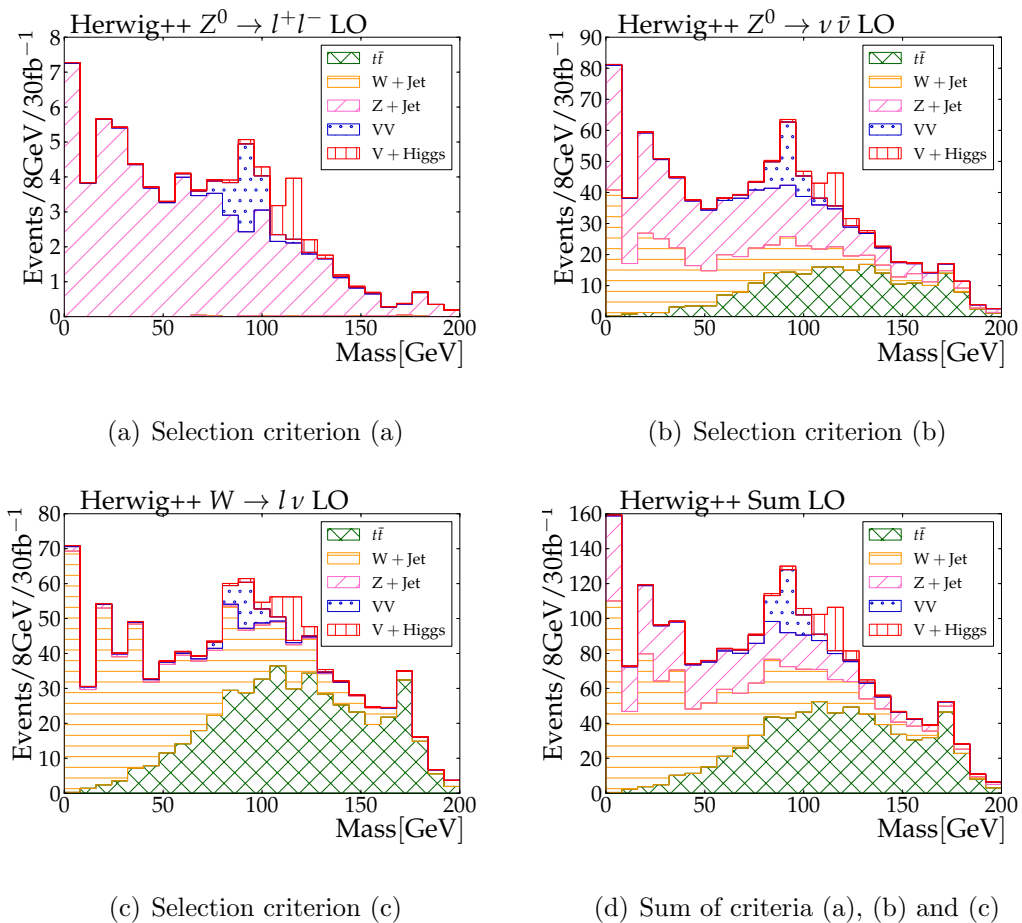


Figure 2.9: Results for the reconstructed Higgs boson mass distribution using leading-order matrix elements. A SM Higgs boson was assumed with a mass of 115 GeV. In addition to the full result the contribution from top quark pair production ($t\bar{t}$), the production of W^\pm (W+Jet) and Z^0 (Z+Jet) bosons in association with a hard jet, vector boson pair production (VV) and the production of a vector boson in association with the Higgs boson (V+Higgs), are shown.

Cambridge-Aachen algorithm [104, 105] with radius parameter $R = 1.2$ gave the best results when combined with their jet substructure technique. For our study, we used the Cambridge-Aachen algorithm as implemented in the **FastJet** package [106]. Three different event selection criteria are used:

- (a) a lepton pair with $80 \text{ GeV} < m_{l^+l^-} < 100 \text{ GeV}$ and $p_T > p_T^{\min}$ to select events for $Z^0 \rightarrow l^+l^-$;
- (b) missing transverse momentum $\cancel{p}_T > p_T^{\min}$ to select events with $Z^0 \rightarrow \nu\bar{\nu}$;

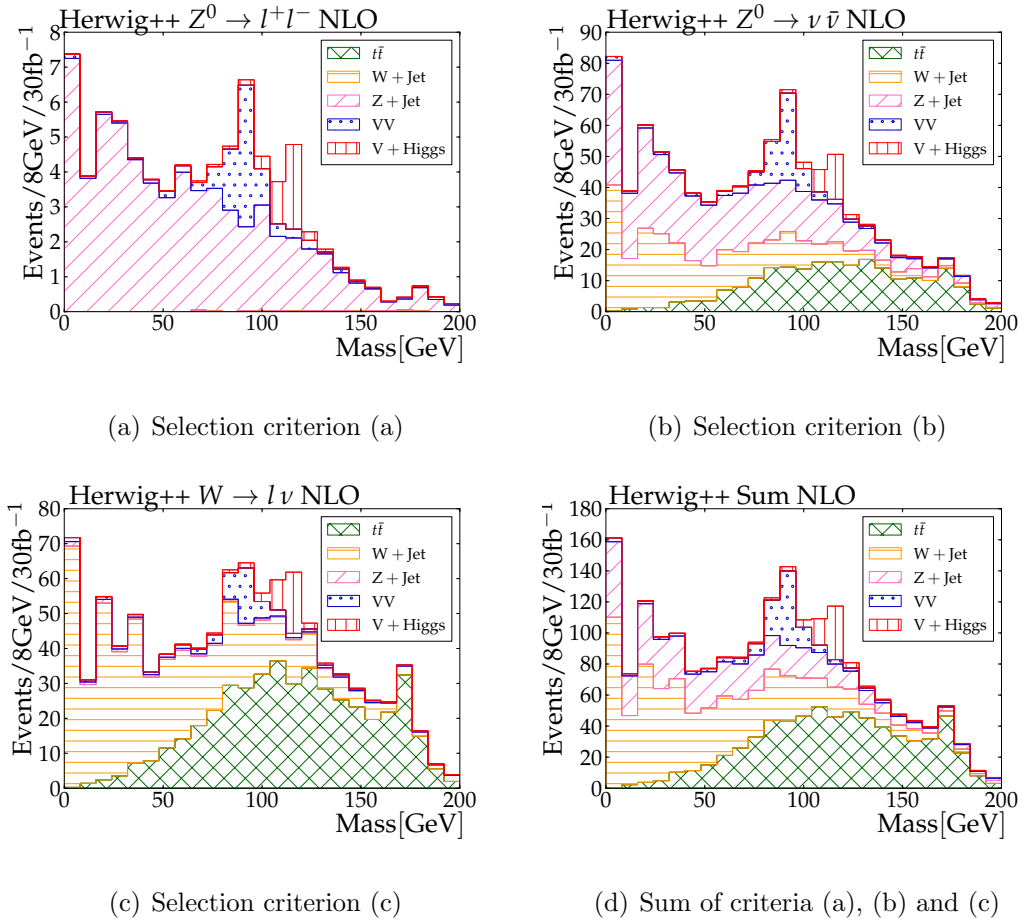


Figure 2.10: Results for the reconstructed Higgs boson mass distribution using leading-order matrix elements for top quark pair production ($t\bar{t}$), and the production of W^\pm (W+Jet) and Z^0 (Z+Jet) bosons in association with a hard jet. The next-to-leading-order corrections are included for vector boson pair production (VV) and the production of a vector boson in association with the Higgs boson (V+Higgs) as well as in the decay of the Higgs boson, $h^0 \rightarrow b\bar{b}$. A SM Higgs boson was assumed with a mass of 115 GeV.

(c) missing transverse momentum $\cancel{p}_T > 30$ GeV and a lepton with $p_T > 30$ GeV consistent with the presence of a W boson with $p_T > p_T^{\min}$ to select events with $W \rightarrow \ell\nu$;

where $p_T^{\min} = 200$ GeV.

In addition the presence of a hard jet with $p_{T_j} > p_T^{\min}$ with substructure is required. The substructure analysis of Ref. [68] proceeds with the hard jet j with

Significance			
Process	Order	$\frac{S}{\sqrt{B}}$	$\frac{S}{\sqrt{B}}$
		Herwig++ default	Herwig++ tune
$Z^0 \rightarrow l^+l^-$	LO	1.17	$1.24^{+0.36}_{-0.11}$
	NLO	1.57	$1.96^{+0.29}_{-0.30}$
$Z^0 \rightarrow \nu\bar{\nu}$	LO	1.77	$2.30^{+0.17}_{-0.38}$
	NLO	2.41	$3.24^{+0.24}_{-0.61}$
$W \rightarrow l\nu$	LO	1.88	$2.32^{+0.15}_{-0.27}$
	NLO	2.63	$3.20^{+0.29}_{-0.36}$
Total	LO	2.75	$3.43^{+0.27}_{-0.46}$
	NLO	3.79	$4.81^{+0.41}_{-0.70}$

Table 2.8: The significance of the different processes for the leading- and next-to-leading-order matrix elements. The significance is calculated using all masses in the range 112-120 GeV.

some radius R_j , a mass m_j and in a mass-drop algorithm:

1. the two subjets which were merged to form the jet, ordered such that the mass of the first jet m_{j_1} is greater than that of the second jet m_{j_2} , are obtained;
2. if $m_{j_1} < \mu m_j$ and

$$y = \frac{\min(p_{Tj_1}^2, p_{Tj_2}^2)}{m_j^2} \Delta R_{j_1, j_2}^2 > y_{\text{cut}}, \quad (2.3.16)$$

where $\Delta R_{j_1, j_2}^2 = (y_{j_1} - y_{j_2})^2 + (\phi_{j_1} - \phi_{j_2})^2$, and $p_{Tj_{1,2}}$, $\eta_{j_{1,2}}$, $\phi_{j_{1,2}}$ are the transverse momenta, rapidities and azimuthal angles of jets 1 and 2, respectively, then j is in the heavy particle region. If the jet is not in the heavy particle region the procedure is repeated using the first jet.

This algorithm requires that $j_{1,2}$ are b -tagged and takes $\mu = 0.67$ and $y_{\text{cut}} = 0.09$. A uniform b -tagging efficiency of 60% was used with a uniform mistagging probability

of 2%. The heavy jet selected by this procedure is considered to be the Higgs boson candidate jet. Finally, there is a filtering procedure on the Higgs boson candidate jet, j . The jet, j , is resolved on a finer scale by setting a new radius $R_{\text{filt}} = \min(0.3, R_{b\bar{b}}/2)$, where from the previous mass-drop condition, $R_{b\bar{b}} = \Delta R_{j_1, j_2}^2$. The three hardest subjets of this filtering process are taken to be the Higgs boson decay products, where the two hardest are required to be b -tagged.

All three analyses require that:

- after the reconstruction of the vector boson, there are no additional leptons with pseudorapidity $|\eta| < 2.5$ and $p_T > 30$ GeV;
- other than the Higgs boson candidate, there are no additional b -tagged jets with pseudorapidity $|\eta| < 2.5$ and $p_T > 50$ GeV.

In addition, due to top contamination, criterion (c) requires that other than the Higgs boson candidate, there are no additional jets with $|\eta| < 3$ and $p_T > 30$ GeV. For all events, the candidate Higgs boson jet should have $p_T > p_T^{\text{min}}$. The analyses were implemented using the Rivet system [101].

The simulations in this Chapter were produced before the announcement of the discovery of a new boson of mass around 125 GeV [107, 108], which is a candidate SM Higgs boson, and so the mass of the Higgs boson was assumed to be 115 GeV from the LEP bounds. We expect a difference in mass of 10 GeV to have no significant effect on the results presented.

First we show in Fig. 2.8 the results of the analyses when used with HERWIG as a proof of methodology, when compared to the plots in Ref. [68]. The plots shown in Fig. 2.9 use the leading-order matrix elements for the production and decay of Higgs boson but the W , Z and top [109] have matrix element corrections for their decays. The plots shown in Fig. 2.10 have leading-order $t\bar{t}$ production, leading-order vector boson plus jet production (with the same matrix element corrections as the LO matrix elements) but the NLO vector boson pair production [110] and NLO vector and Higgs boson associated production [63]. In addition we have implemented the corrections to the decay $h^0 \rightarrow b\bar{b}$ in the POWHEG scheme, as described earlier. The signal significances are outlined in Table 2.8.

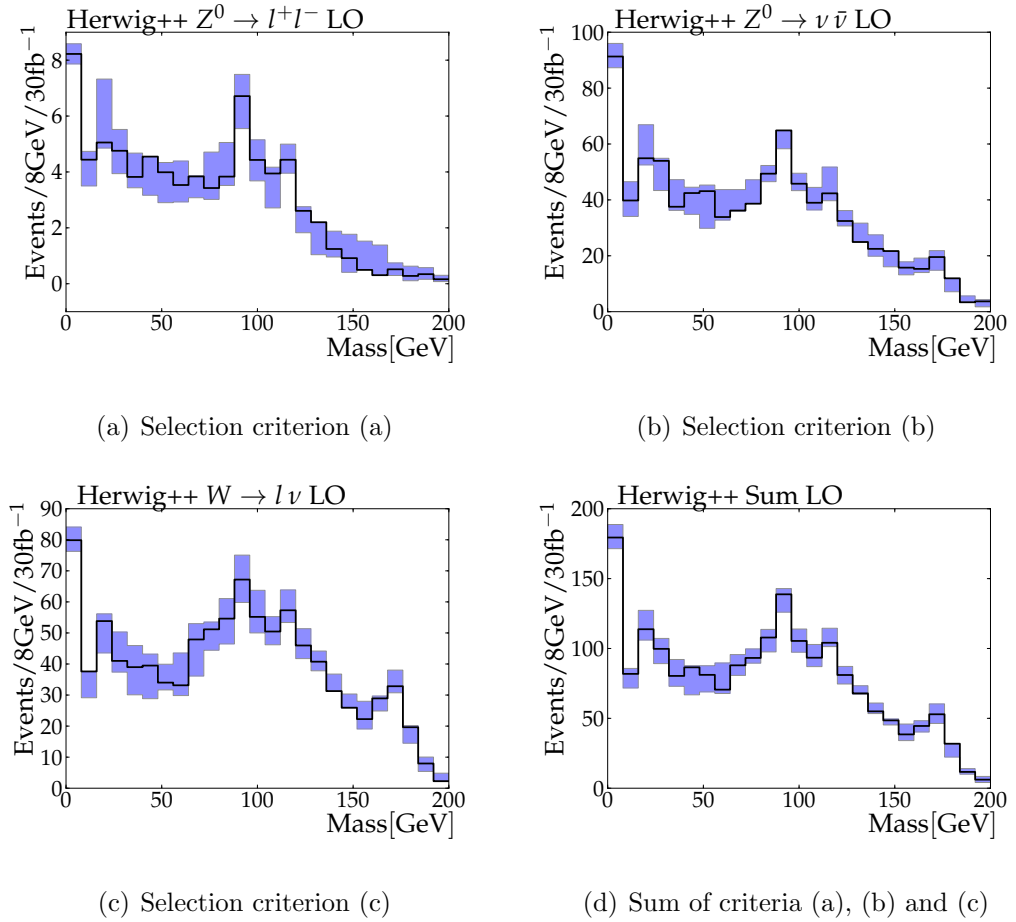


Figure 2.11: Results for the reconstructed Higgs boson mass distribution using leading-order matrix elements. A SM Higgs boson was assumed with a mass of 115 GeV. The envelope shows the uncertainty from the Monte Carlo simulation. We have not shown the statistical error.

The uncertainties due to the Monte Carlo simulation are shown as bands in Figs. 2.11 and 2.12. As there are correlations between the different processes the uncertainty is determined for the sum of all processes. Whilst it would be possible to show the envelope for the individual processes, this would not offer any information on the envelope for the sum of the processes which is the result of interest. In addition the uncertainty on the significance is shown in Table 2.8.

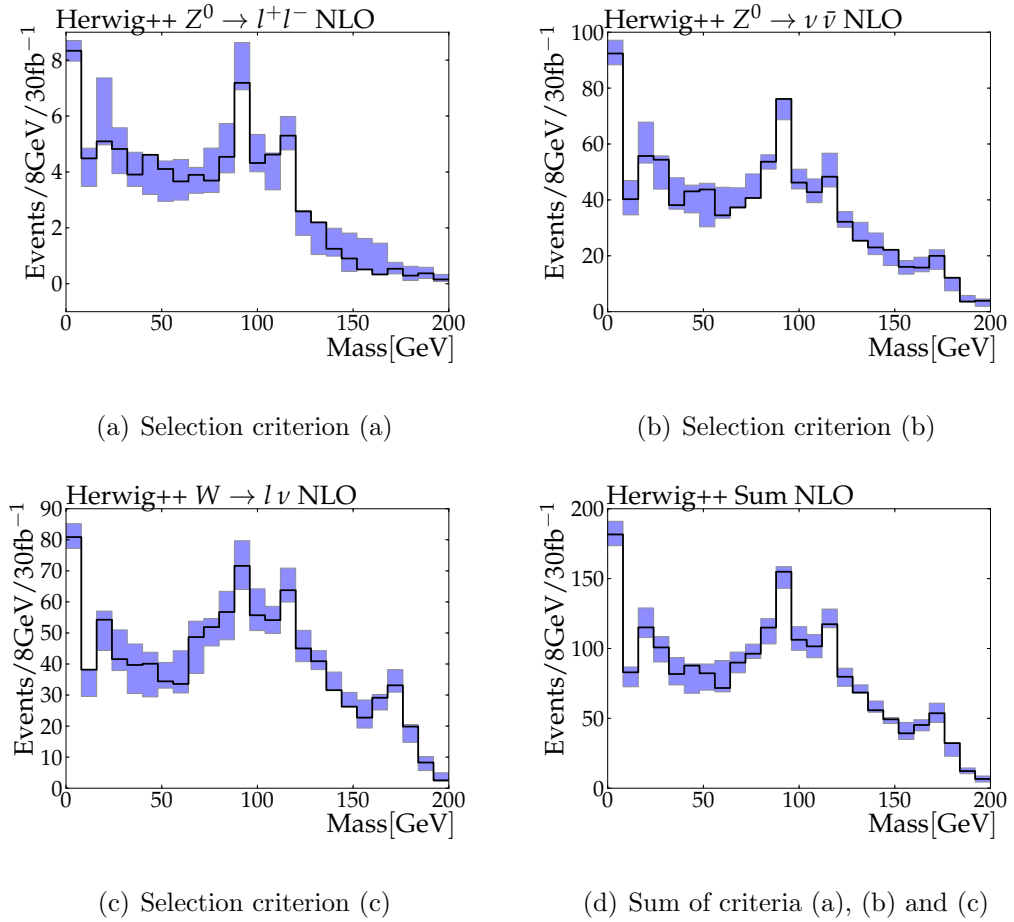


Figure 2.12: Results for the reconstructed Higgs boson mass distribution using leading-order matrix elements for top quark pair production, and the production of W^\pm and Z^0 bosons in association with a hard jet. The next-to-leading-order corrections are included for vector boson pair production and the production of a vector boson in association with the Higgs boson as well as in the decay of the Higgs boson, $h^0 \rightarrow b\bar{b}$. A SM Higgs boson was assumed with a mass of 115 GeV. The envelope shows the uncertainty from the Monte Carlo simulation. We have not shown the statistical error.

2.4 Conclusions

While significant effort has been devoted to the tuning of the parameters to produce a best fit there has been much less effort understanding the uncertainties in these results. In this chapter we have produced a set of tunes which can be used to assess this uncertainty using the Herwig++ Monte Carlo event generator. We note

that usually statistical errors are the only errors shown on results produced with a Monte Carlo event generator, however, we have not shown these here as the aim is to emphasise the new tuning errors we have produced.

We then used these tunes to assess the uncertainties on the mass-drop analysis of Ref. [68] using `Herwig++` with both leading- and next-to-leading-order matrix elements including a POWHEG simulation of the decay $h^0 \rightarrow b\bar{b}$.

We have verified the results of Ref. [68] and extended this by using improved simulation of certain aspects of the radiation. Although not currently being used at the LHC as a discovery channel, we have seen that there is potential, with further improvements, to use the predominant decay of a light Higgs boson to bottom quarks, via jet substructure, as a discovery channel. This technique may also be used to gain insight into the coupling of a light Higgs boson to bottom quarks.

However, before we can embark on large studies using jet substructure we need to be confident of our tunes to investigate this with Monte Carlo simulations and it is the process undertaken here that gives us that confidence. In addition, the error tunes and procedure outlined in this chapter can now be used in other analyses where the uncertainty due to the Monte Carlo simulation is important.

There is still room for improvement in the simulation of process that will affect a jet substructure analysis. This includes, for example, a better study of the $g \rightarrow b\bar{b}$ splitting as implemented in a Monte Carlo event generator. Clearly the $g \rightarrow b\bar{b}$ splitting is important in an analysis as undertaken here, so further study including topics such as choice of scale for the coupling and whether to angular order this splitting would be beneficial.

Also, as further data comes out from the LHC with its complex hadronic final states, including effects of underlying event in the tune would also be helpful as any study of jet substructure will be sensitive to underlying event. This could include the effects of new and different underlying event models and their effect on jet substructure and any effects from the tuning of the underlying event models to data.

Chapter 3

Improved Simulation of Soft Radiation in the Production and Decay of Unstable Particles

Following the discovery of the top quark [111, 112] the measurement of the top quark mass has been refined using a succession of ever more sophisticated analysis techniques. The latest result, $m_t = 173.18 \pm 0.56$ (stat) ± 0.75 (syst) GeV, [113] from the Tevatron experiments, has an error of less than 1 GeV. While the early measurements by the LHC experiments had larger errors the latest CMS preliminary measurement using a combination of channels, $m_t = 173.36 \pm 0.38$ (stat) ± 0.91 (syst) GeV [114], and ATLAS measurement in the lepton plus jets channel, $m_t = 174.5 \pm 0.6$ (stat) ± 2.3 (syst) GeV [115], have errors which are approaching that of the Tevatron measurement. These results rely on Monte Carlo simulations of top quark production and decay either directly in *Template methods* [116–118] or in extracting corrections in *Matrix Element Methods* [119–121].

As the top quark is heavier than the W^\pm boson its lifetime is shorter than hadronization timescale making it unique in decaying before the formation of top hadrons. In Monte Carlo simulations this is simulated by first simulating the hard process in which the top quark is produced, followed by the subsequent evolution, via perturbative gluon radiation, to the cut-off scale. The decay of the top quark is

then simulated as a hard perturbative process, due to the large perturbative scale provided by the top quark mass, and evolved to the cut-off scale using the parton-shower algorithm.

As the error on the top quark mass decreases it is essential that we understand the relationship between the experimentally measured quantity and the perturbative top quark mass defined in a rigorous renormalisation scheme [122–125]¹. An alternative to measuring the top quark mass using kinematic variables is to extract it from the top quark pair production cross section [126], however while defined in a specific renormalisation scheme the current results from this approach have a much larger error, *e.g.* $m_t = 170 \pm 7$ GeV [127]

In particular from the point of view of Monte Carlo simulations, in addition to the top mass and infrared cut-off scale, the top quark width (Γ_t) provides an additional scale in the production and subsequent decay of the top quark. While gluons with energies above the top quark width ($E \gg \Gamma_t$) can resolve the production and decay of the top quark, gluons with very low energies ($E \ll \Gamma_t$) cannot resolve the presence of the top quark and in terms of a Monte Carlo simulation should be regarded as if they are emitted from the top decay products without any knowledge of the top quark. First studies of this effect for e^+e^- initiated top quark production process can be found in Ref. [128].

While in top quark production this may not be a significant effect because the top quark width ($\Gamma_t \sim 1.4$ GeV) is already close to the infrared cut-off scale given the ever decreasing error on the top quark mass, it must be investigated. Equally, while this may not be an important effect in the Standard Model in models of physics Beyond the Standard Model (BSM) there are often heavy strongly interacting particles with much larger widths where these effects will be greater.

In this chapter we present a systematic approach to include the width in these simulations. We start by recalculating the existing radiation patterns, using techniques from chapter 1, for single gluon emission in the soft limit in top quark production from quark–quark, gluon–gluon and e^+e^- initial states, followed by extending

¹The interested reader can find a review of these issues in Appendix C of Ref. [42].

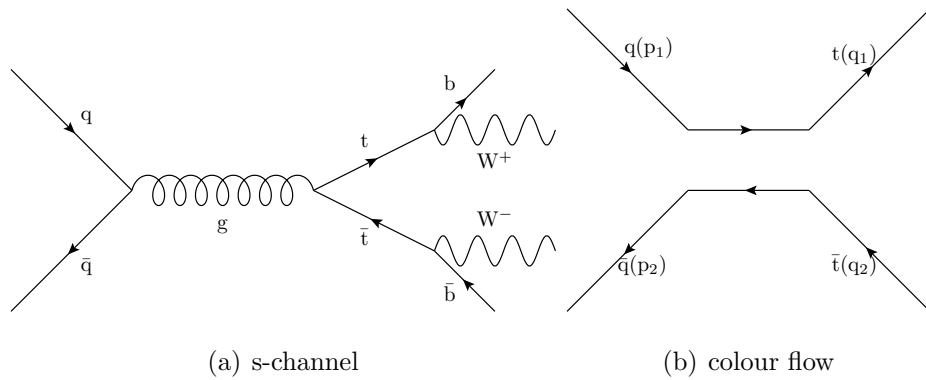


Figure 3.1: The tree level initial state quark-quark initiated top quark production process and associated colour flow.

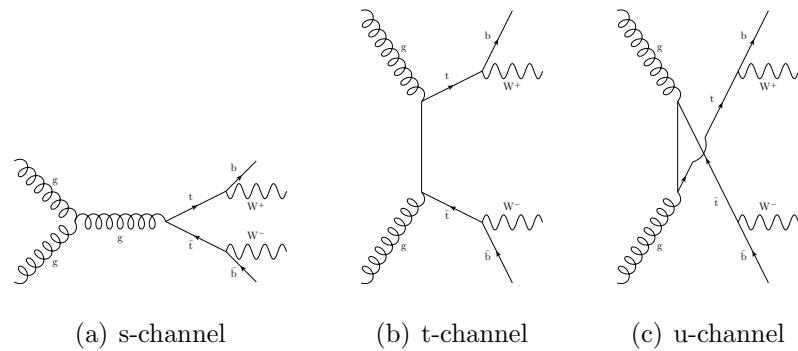


Figure 3.2: The tree level initial state gluon-gluon top quark production processes.

these calculations to double gluon emission in the same limit for both processes. We also calculate the patterns for stop production. This allows us to interpret the patterns in terms of an algorithm for implementation in a Monte Carlo event generator. Finally, we show the effect of implementing the new algorithm in the `Herwig++` Monte Carlo event generator on the determination of the top mass.

3.1 Radiation Patterns

3.1.1 Top Quark Pair Production in Hadron–Hadron Collisions

The main production mechanisms for top quarks in hadron–hadron collisions are shown in Figs. 3.1 and 3.2. At the Tevatron the quark-antiquark production mech-

anism is dominant due to the presence of valance antiquarks in the incoming antiproton, while at the LHC due to the large gluon parton density at higher energies and proton–proton initial state the gluon-gluon production mechanism dominates.

The radiation patterns for single gluon emission have already been covered in detail in the literature [44, 129–131], however, we repeat it here as validation of our methodology² and in order to interpret the radiation patterns in terms of implementation in a Monte Carlo simulation.

We first consider the soft radiation from the process $q\bar{q} \rightarrow t\bar{t}$ including the decays of the top quark, $t \rightarrow bW^+$, and anti-top quark $\bar{t} \rightarrow \bar{b}W^-$. The leading-order Feynman diagram and unique colour flow for this process are shown in Fig. 3.1. We make use of the results from Ref. [131] and, as we will be using the same basic approach for a number of processes, we give the details of the calculation for this process.

The current is

$$\begin{aligned} \mathcal{J}^\mu(p_1, p_2, p_b, p_{\bar{b}}, k) = & \frac{1}{2} \left[\mathbf{t}_{ki}^B \delta_{jl} P_t(q_t^2) P_{\bar{t}}((q_t + k)^2) \left(\frac{p_b^\mu}{p_b \cdot k} - \frac{q_t^\mu}{q_t \cdot k} \right) \right. \\ & + \mathbf{t}_{ji}^B \delta_{ik} P_t(q_t^2) P_{\bar{t}}((q_{\bar{t}} + k)^2) \left(\frac{q_{\bar{t}}^\mu}{q_{\bar{t}} \cdot k} - \frac{p_{\bar{b}}^\mu}{p_{\bar{b}} \cdot k} \right) \\ & + \mathbf{t}_{jl}^B \delta_{ik} P_t(q_t^2) P_{\bar{t}}(q_{\bar{t}}^2) \left(\frac{p_2^\mu}{p_2 \cdot k} - \frac{q_{\bar{t}}^\mu}{k \cdot q_{\bar{t}}} \right) \\ & \left. + \mathbf{t}_{ki}^B \delta_{jl} P_t(q_t^2) P_{\bar{t}}(q_{\bar{t}}^2) \left(\frac{q_t^\mu}{k \cdot q_t} - \frac{p_1^\mu}{p_1 \cdot k} \right) \right] \\ & - \frac{1}{2N_C} \left[\mathbf{t}_{ji}^B \delta_{kl} P_t(q_t^2) P_{\bar{t}}(q_{\bar{t}}^2) \left(\frac{p_2^\mu}{p_2 \cdot k} - \frac{p_1^\mu}{p_1 \cdot k} \right) \right. \\ & + \mathbf{t}_{kl}^B \delta_{ij} P_t(q_t^2) P_{\bar{t}}(q_{\bar{t}}^2) \left(\frac{q_t^\mu}{k \cdot q_t} - \frac{q_{\bar{t}}^\mu}{k \cdot q_{\bar{t}}} \right) \\ & \left. + \mathbf{t}_{kl}^B \delta_{ij} P_{\bar{t}}(q_{\bar{t}}^2) P_t((q_t + k)^2) \left(\frac{p_b^\mu}{p_b \cdot k} - \frac{q_t^\mu}{q_t \cdot k} \right) \right] \end{aligned}$$

²We automated the calculation of the Feynman diagrams and associated currents. We first used FeynArts [132] to produce the Feynman diagrams for the processes with the appropriate number of external gluons. The FORM [36] output of FeynArts was then taken and a set of eikonal rules applied within FORM to generate the set of dipoles for each diagram. The resulting expression was then manipulated in Mathematica using FeynCalc [133] to produce an expression for the radiation pattern.

$$+\mathbf{t}_{kl}^B \delta_{ij} P_t(q_t^2) P_{\bar{t}}((q_{\bar{t}} + k)^2) \left(\frac{q_{\bar{t}}^\mu}{q_{\bar{t}} \cdot k} - \frac{p_{\bar{b}}^\mu}{p_{\bar{b}} \cdot k} \right) \Big], \quad (3.1.1)$$

where $p_{1,2}$ are the 4-momenta of the incoming quark and anti-quark, respectively. The bottom and anti-bottom quarks have 4-momenta p_b and $p_{\bar{b}}$, respectively. The 4-momenta of the top and anti-top quarks are q_t and $q_{\bar{t}}$, respectively. In general we will neglect sub-leading terms in the number of colours $N_C = 3$, but they are included here for completeness. The propagator factor for a heavy particle is

$$P_a(q_a^2) = \frac{1}{(q_a^2 - M_a^2) + \Gamma_a^2 M_a^2}, \quad (3.1.2)$$

where q_a , M_a and Γ_a , are the 4-momenta, mass and width of the particle, respectively. This current, from Ref. [131], is derived by only retaining the gluon momentum in the propagator factors and using

$$P_a(q^2) P_a((q+k)^2) = \frac{1}{2q \cdot k} (P_a(q^2) - P_a((q+k)^2)). \quad (3.1.3)$$

Using the same approach as Ref. [131] we can integrate over the off-shell masses of the top quark and antiquark

$$\int dq_t^2 dq_{\bar{t}}^2 \sum_{\text{spins}} |\mathcal{M}(\{p_0\}, p_k)|^2 \approx g_s^2 \left(\frac{\pi}{M_t \Gamma_t} \right)^2 \sum_{\text{spins}} |\mathcal{M}_0^n(\{p_0\})|^2 \mathcal{F}_n. \quad (3.1.4)$$

with

$$\mathcal{F}_n \equiv \left(\frac{M_t \Gamma_t}{\pi} \right)^2 \int dq_t^2 dq_{\bar{t}}^2 [-J^n \cdot J^{n*}], \quad (3.1.5)$$

where the neglected cross terms are sub-leading in N_C with respect to the leading term.

Here there is only one colour flow and the leading contribution in N_C to the radiation pattern is

$$\begin{aligned} \frac{\omega^2}{2} \mathcal{F} = \frac{C_A}{2} & [(1 - C_t) (W_{p_1, t} + W_{b, t}) + C_t W_{p_1, b} + \\ & (1 - C_{\bar{t}}) (W_{p_2, \bar{t}} + W_{\bar{b}, \bar{t}}) + C_{\bar{t}} W_{p_2, \bar{b}}], \end{aligned} \quad (3.1.6)$$

where $W_{ij} = W_{ij}(p_g)$ and the coefficients $C_{t, \bar{t}}$ are

$$C_t(k) = \frac{M_t^2 \Gamma_t^2}{M_t^2 \Gamma_t^2 + (q_t \cdot k)^2}, \quad (3.1.7a)$$

$$C_{t,\bar{t}}(k) = \frac{M_t^2 \Gamma_t^2}{M_t^2 \Gamma_t^2 + (q_{\bar{t}} \cdot k)^2}. \quad (3.1.7b)$$

There are two important limits of this result. The first is $q_{t,\bar{t}} \cdot k \gg M_t \Gamma_t$. In this limit $C_{t,\bar{t}}(k) \rightarrow 0$ and the radiation pattern is

$$\frac{\omega^2}{2} \mathcal{F} = \frac{C_A}{2} [W_{p_1,t} + W_{b,t} + W_{p_2,\bar{t}} + W_{\bar{b},\bar{t}}]. \quad (3.1.8)$$

In this case we have radiation from the dipole formed by the light and top quarks, and light antiquark and anti-top quark in the hard process and between the top-bottom dipole in both the top quark and antiquark decays.

The second limit is $q_{t,\bar{t}} \cdot k \ll M_t \Gamma_t$. In this limit $C_{t,\bar{t}}(k) \rightarrow 1$ and the radiation pattern is

$$\frac{\omega^2}{2} \mathcal{F} = \frac{C_A}{2} [W_{p_1,b} + W_{p_2,\bar{b}}], \quad (3.1.9)$$

which corresponds to the case where the radiation cannot resolve the production of the top quarks and is from the dipoles formed by the incoming (anti)quark and outgoing (anti)bottom quark.

In order to interpret that radiation pattern in terms of a parton-shower algorithm the standard approach is to split the dipole radiation function into two parts as in Eqn. 1.2.37.

In the FORTRAN version of **HERWIG** the decomposition [44]

$$W_{ij}^i = \frac{1}{2\xi_i} \left(1 - \frac{1}{\gamma_i^2 \xi_i} + \frac{\xi_{ij} - \xi_i}{\xi_j} \right) \quad (3.1.10)$$

was used. However, in **Herwig++** different shower variables [37] are used and there is no corresponding exact decomposition in the soft limit. The **Herwig++** shower algorithm is constructed by requiring that the upper limits of the parton-shower evolution variable for the two colour-connected particles are chosen in order to cover the phase space in the soft limit, with the best possible approximation to the correct angular distribution. This leads to a different approximation to the eikonal result in the two disjoint regions of phase space filled by radiation from the two particles. However, the approximations to the radiation functions $W_{ij}^{i,\text{shower}}$ and $W_{ij}^{j,\text{shower}}$ in the **Herwig++** shower algorithm still ensure that $W_{ij}^{i,\text{shower}}$ contains the collinear singularity for emission from i and $W_{ij}^{j,\text{shower}}$ contains the collinear singularity for emission from j in the ij dipole.

In both the FORTRAN HERWIG and Herwig++ this decomposition is done in different frames for the different dipoles, *e.g.* in the centre-of-mass frame for the production of the top quarks and in their rest frame for the decay. We can calculate the shower decomposition of the radiation functions in the Herwig++ shower variables using the kinematics outlined in Ref. [93], upon which the Herwig++ shower is based. We now look at each of these cases in turn.

Shower Approximation

Final-Final Connection

In a final-final colour connection, for a colour singlet in the process $a \rightarrow b + c$ the momentum of a is preserved and, working in its rest frame [93],

$$p_a = Q(1, 0, 0, 0), \quad p_b = \frac{1}{2}Q(1 + b - c, 0, 0, \lambda), \quad p_c = \frac{1}{2}Q(1 - b + c, 0, 0, -\lambda), \quad (3.1.11)$$

where $p_a^2 = Q^2$, $b = m_b^2/Q^2$, $c = m_c^2/Q^2$ and

$$\lambda = \lambda(1, b, c) \equiv \sqrt{(1 + b - c)^2 - 4b} = \sqrt{(1 - b + c)^2 - 4c}. \quad (3.1.12)$$

Making use of the $e^+e^- \rightarrow t\bar{t}$ process, in the new variables the emission probability from the top in the dipole, formed by the $t\bar{t}$ pair is

$$dP = \frac{1}{2(2\pi)^3} \frac{d\omega}{\omega} d\cos\theta d\phi g_s^2 C_F W_{ij}^{i,\text{shower}} \quad (3.1.13)$$

where θ is the angle between the emitting particle, b , and the gluon, the angle ϕ is the azimuthal angle and ω the gluon's energy. From these we find that the shower approximation to the radiation function is

$$W_{t\bar{t}}^{t,\text{shower}} = \frac{2(1 + b - c + \lambda)}{(1 + \cos\theta)(1 + b - c - \lambda \cos\theta)} - \frac{4b}{(1 + b - c - \lambda \cos\theta)^2}. \quad (3.1.14)$$

Decay Colour Connection

For processes where the decay is colour connected, *e.g.* the process $b \rightarrow c + a$ where a is a colour singlet and the decaying parton b and outgoing parton c are colour-connected, the momentum of the decaying parton b is preserved, therefore we work

in its rest frame,

$$p_b = m_b(1, 0, 0, 0), \quad p_c = \frac{1}{2}m_b(1 - a + c, 0, 0, \lambda), \quad p_a = \frac{1}{2}m_b(1 + a - c, 0, 0, -\lambda), \quad (3.1.15)$$

where $a = m_a^2/m_b^2$, $c = m_c^2/m_b^2$ and now

$$\lambda = \lambda(1, a, c) = \sqrt{(1 + a - c)^2 - 4a} = \sqrt{(1 - a + c)^2 - 4c}. \quad (3.1.16)$$

Making use of the $t \rightarrow W^+b$ process, in the new variables the emission probability from the top quark in the dipole, formed by the tb pair is,

$$dP = \frac{1}{2(2\pi)^3} \frac{d\omega}{\omega} d\cos\theta d\phi g_s^2 C_F W_{tb}^{t,\text{shower}}, \quad (3.1.17)$$

where θ is the angle of the gluon with respect to the bottom quark in the rest frame of the decaying top and [109]

$$W_{tb}^{t,\text{shower}} = \frac{1 + \cos\theta}{1 - \cos\theta}. \quad (3.1.18)$$

The radiation from the bottom, in the top rest frame has the same form as for the top in the final-final colour connection.

Initial-Initial Colour Connection

For processes where the initial state particles are colour connected, the inverse process $b + c \rightarrow a$ where a is a colour singlet of invariant mass Q and b, c are beam jets, is considered. The beam jets are taken to be massless in the centre of mass frame and we therefore have

$$p_a = Q(1, 0, 0, 0), \quad p_b = \frac{1}{2}Q(1, 0, 0, 1), \quad p_c = \frac{1}{2}Q(1, 0, 0, -1). \quad (3.1.19)$$

Making use of the $q\bar{q} \rightarrow Z^0$ process, in the new variables the emission probability from the top in the dipole, formed by the $q\bar{q}$ pair is,

$$dP = \frac{1}{2(2\pi)^3} \frac{d\omega}{\omega} d\cos\theta d\phi g_s^2 C_F W_{q\bar{q}}^{q,\text{shower}} \quad (3.1.20)$$

where

$$W_{q\bar{q}}^{q,\text{shower}} = \frac{4}{\sin^2\theta} \quad (3.1.21)$$

where θ is the angle of the gluon with respect to the emitting particle. The radiation off the anti-quark has the same form as radiation off the quark.

Initial-Final Colour Connection

For a process with an initial-final colour connection, we consider the process $a+b \rightarrow c$ where a is a colour singlet. We need to preserve the momentum of a and therefore work in the Breit frame:

$$p_a = Q(0, 0, 0, -1), \quad p_b = \frac{1}{2}Q(1+c, 0, 0, 1+c), \quad p_c = \frac{1}{2}Q(1+c, 0, 0, -1+c), \quad (3.1.22)$$

where $p_a^2 = -Q^2$, $p_b^2 = 0$, and $m_c^2 = cQ^2$. The beam parton b is *always* taken as massless, but the outgoing parton c can be massive.

Making use of the DIS $q_i\gamma^* \rightarrow q_f$ process, in the new variables the emission probability from initial state quark in the dipole, formed by the q_iq_f pair is,

$$dP = \frac{1}{2(2\pi)^3} \frac{d\omega}{\omega} d\cos\theta d\phi g_s^2 C_F W_{q_iq_f}^{q_i, \text{shower}} \quad (3.1.23)$$

where

$$W_{q_iq_f}^{q_i, \text{shower}} = \frac{4}{\sin^2\theta} \quad (3.1.24)$$

where θ is the angle of the gluon with respect to the emitting particle.

The radiation off the final state quark q_f takes the form

$$W_{q_iq_f}^{q_f, \text{shower}} = \frac{4(1 - \cos\theta)}{(1 + \cos\theta)(1 + c - \cos\theta(1 - c))^2}, \quad (3.1.25)$$

where the emission probability takes a similar form.

Armed with this knowledge, we are now in a position to calculate radiation patterns. In producing the radiation patterns below, we use the configuration as shown in Fig. 3.3 [131]. We take the mass of the top $m_t = 174.2$ GeV and the width of the top $\Gamma_t = 1.4$ GeV. The energy of each beam particle was $2m_t$, giving a total centre-of-mass energy $\sqrt{s} = 4m_t$. This ensures the top quarks are produced above threshold.

In Fig. 3.4 we show the radiation pattern associated with this process. Throughout, the full result is the full calculation including all subleading terms, the full shower approximation is the full expression with the W functions replaced by the shower approximation, the leading term is the leading N_C approximation and the

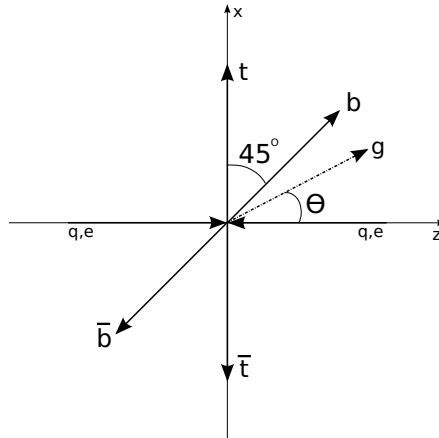


Figure 3.3: A schematic of the kinematics used to plot the $t\bar{t}$ single gluon emission radiation patterns shown below. The incoming beam particles depend on the process being studied.

leading shower approximation is the shower approximation to the leading N_C contribution. We note on the plot the suppression of radiation associated with emission around the bottom quarks at 45° and 225° , owing to the bottom quark having finite mass. We also see the singularity associated with the incoming quarks at 180° and 0° along with the top quarks at 90° and 270° .

We can interpret this radiation pattern as the radiation from the incoming quark and outgoing top quark dipole being suppressed by $(1 - C_t)$ and radiation from the dipole formed by the incoming quark and bottom being suppressed by C_t . The same applies for the other colour dipoles in the radiation pattern, but with C_t being replaced with $C_{\bar{t}}$. It is also worth noting that the leading colour contribution is very similar to the full result and therefore taking the leading contribution is actually providing a good approximation.

The gluon-gluon initial state is more complicated because the leading-order matrix element decomposes into two terms corresponding to t -channel and u -channel colour flows as shown in Fig. 3.5. The interference of these two terms makes identifying the colour flows in the planar limit difficult [131]. However, in the large N_C limit this interference is suppressed and we are left with a separation into two positive definite colour flows as discussed in Ref. [129].

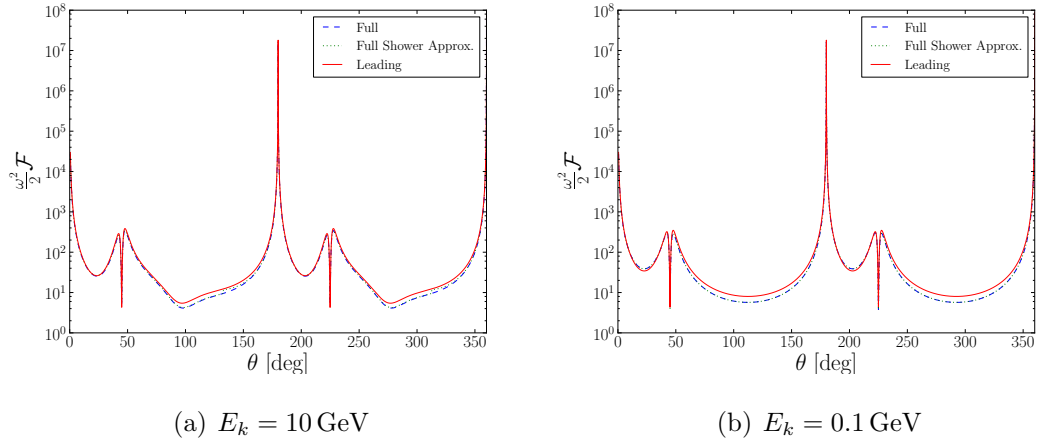


Figure 3.4: The radiation pattern for single emission from $q\bar{q} \rightarrow t\bar{t}$. Noting the logarithmic scale, we show the full radiation pattern, the shower approximation to the full radiation pattern and the leading N_C contribution. E_k is the energy of the emitted gluon. The dips in the pattern are associated with the finite bottom quark mass and we see singularities with the incoming quarks at 0° and 180° . These features are repeated in the other radiation patterns we will display here. We also note that the leading approximation as employed in the shower interpretation is performing well, meaning in the collinear region of interest the approximation is good.

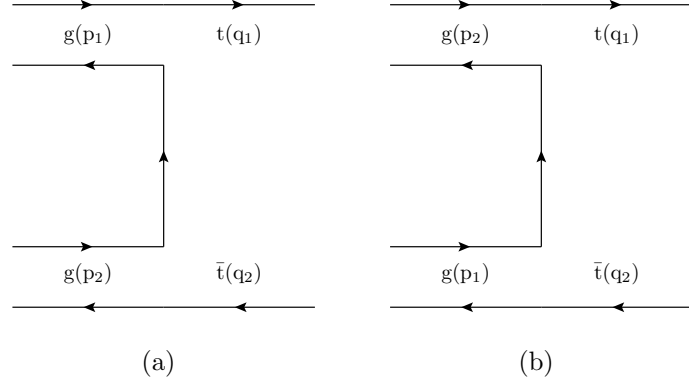


Figure 3.5: Colour flow diagrams for the gluon-gluon initiated processes.

The leading-order spin-summed colour averaged amplitude is [131]

$$\sum_{\text{spins}} |\mathcal{M}_0(\{p_0\})|^2 = \frac{1}{2N_C} \left(\frac{t^2 + u^2}{s^2} - \frac{\mu^2 s^2}{tu} + 2\mu \right) \left(\frac{s^2}{tu} - \frac{N_C}{C_F} \right), \quad (3.1.26)$$

where the Mandelstam variables $s = (p_1 + p_2)$, $t = (p_1 - q_t)^2$, $u = (p_1 - q_{\bar{t}})^2$, $\mu = \frac{2m_{\bar{t}}^2}{s}$ and $p_{1,2}$ are the 4-momenta of the incoming gluons

The leading N_C contribution to the radiation pattern can then be expressed in terms of two kinematic functions, corresponding to the t - and u -channel colour flows and is given by

$$\begin{aligned} \frac{\omega^2 \sum_{\text{spins}} |\mathcal{M}_0^n(\{p_0\})|^2 \mathcal{F}_n}{2 \sum_{\text{spins}} |\mathcal{M}_0(\{p_0\})|^2} = & h(t, s) \frac{C_A^4}{8} [W_{p_1, p_2} + (W_{p_1, t} + W_{b, t}) (1 - C_t) \\ & + (W_{p_2, \bar{t}} + W_{\bar{b}, \bar{t}}) (1 - C_{\bar{t}}) + C_t W_{p_1, b} + C_{\bar{t}} W_{p_2, \bar{b}}] \\ & + h(u, s) \frac{C_A^4}{8} [W_{p_1, p_2} + (W_{p_2, t} + W_{b, t}) (1 - C_t) + \\ & + (W_{p_1, \bar{t}} + W_{\bar{b}, \bar{t}}) (1 - C_{\bar{t}}) + C_{\bar{t}} W_{p_1, \bar{b}} + C_t W_{p_2, b}], \end{aligned} \quad (3.1.27)$$

where [44]

$$h(t, s) = -\frac{2(\mu^2 s^4 + 2\mu s^2 t(s+t) + t(s^3 + 3s^2 t + 4st^2 + 2t^3))}{\sum_{\text{spins}} |\mathcal{M}_0(\{p_0\})|^2 (N_C - 1)^2 s^2 t^2}. \quad (3.1.28)$$

We have chosen to normalise the $h(t, s)$ and $h(u, s)$ functions by the leading-order cross section. The radiation pattern produced by this process is shown in Fig. 3.6.

We can interpret the radiation pattern as the radiation from the top quark gluon and top-bottom dipoles being suppressed by $(1 - C_t)$. The same applies for the anti-particles, but with $(1 - C_t) \rightarrow (1 - C_{\bar{t}})$. There is additional soft radiation from the

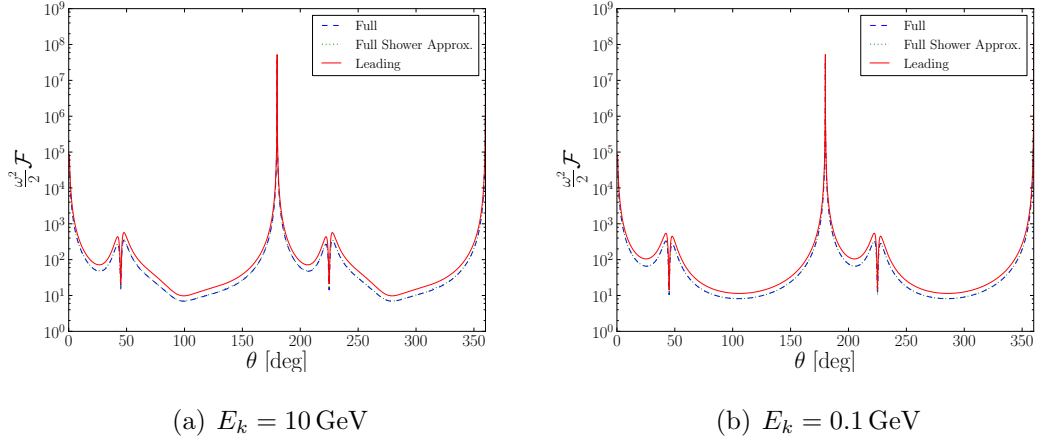


Figure 3.6: The radiation pattern for single emission from $gg \rightarrow t\bar{t}$. We show the full radiation pattern, the shower approximation to the full radiation pattern and the leading N_C contribution to the radiation pattern. E_k is the energy of the emitted gluon.

bottom (anti)quark dipole with radiation suppressed by amount C_t , or $C_{\bar{t}}$ depending on whether it is the bottom or anti-bottom radiating. The radiation from the dipole formed between the two incoming gluons is not suppressed.

In calculating the radiation patterns for two gluons, we work in the strongly ordered limit, where the first emission is harder than the second. We introduce the notation below as $W_{ij} = W_{ij}(k_1)$, $W'_{ij} = W_{ij}(k_2)$, $C_{t(\bar{t})} = C_{t(\bar{t})}(k_1)$ and $D_{t(\bar{t})} = C_{t(\bar{t})}(k_2)$ and, as we are in the strongly ordered limit, $k_1 \gg k_2$ where $k_{1,2}$ are the 4-momenta for the first and second gluon emission, respectively. In the radiation patterns produced below, we fix the first gluon at 340° to the incoming beam, away from the other particles, and we vary the angle of the second gluon as before.

Here,

$$\int dq_t^2 dq_{\bar{t}}^2 \sum_{\text{spins}} |\mathcal{M}(\{p_0\}, k_1, k_2)|^2 \approx g_s^4 \left(\frac{\pi}{M_t \Gamma_t} \right)^2 \sum_{\text{spins}} |\mathcal{M}_0^n(\{p_0\})|^2 \mathcal{F}_n, \quad (3.1.29)$$

where we have introduced two extra factors of g_s and

$$\mathcal{F}_n \equiv \left(\frac{M_t \Gamma_t}{\pi} \right)^2 \int dq_t^2 dq_{\bar{t}}^2 [J^n \cdot J^{n*}]. \quad (3.1.30)$$

The radiation pattern for $q\bar{q} \rightarrow t\bar{t}gg$ is

$$\frac{\omega^2}{2} \mathcal{F}_g = \frac{C_A^2}{4} [W_{p_1, t} (1 - C_t) (W'_{p_1, k_1} + D_t W'_{b, k_1} + D_{\bar{t}} W'_{p_2, \bar{b}} + \dots)] \quad (3.1.31)$$

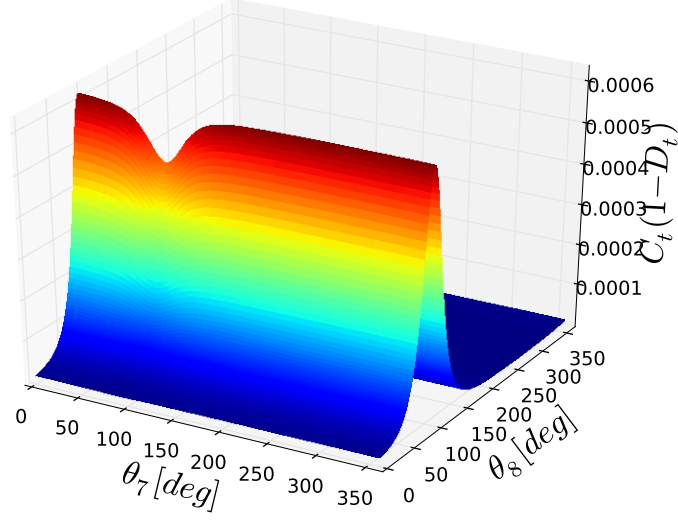
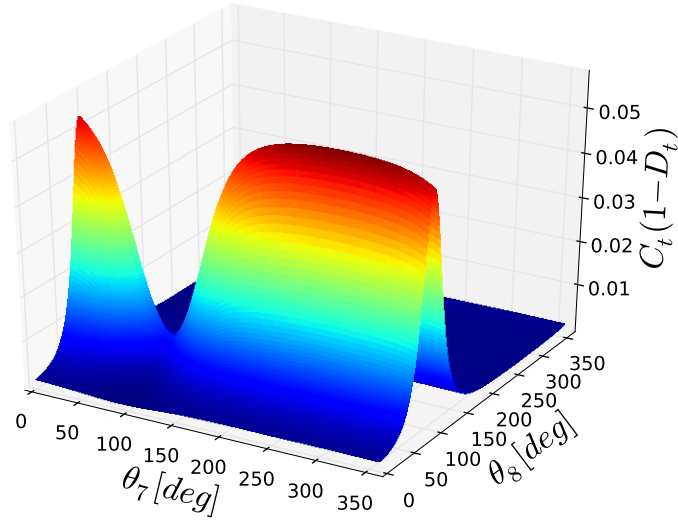
$$\begin{aligned}
& (1 - D_t) (W'_{b,t} + W'_{t,k_1}) + \\
& (1 - D_{\bar{t}}) (W'_{\bar{b},\bar{t}} + W'_{p_2,\bar{t}}) + \\
& W_{p_2,\bar{t}} (1 - C_{\bar{t}}) (W'_{p_2,k_1} + D_{\bar{t}} W'_{\bar{b},k_1} + D_t W'_{p_1,b} + \\
& (1 - D_{\bar{t}}) (W'_{\bar{b},\bar{t}} + W'_{t,k_1}) + \\
& (1 - D_t) (W'_{b,t} + W'_{p_1,t})) + \\
& W_{b,t} (1 - C_t) (W'_{b,k_1} + D_t W'_{p_1,k_1} + D_{\bar{t}} W'_{p_2,\bar{b}} + \\
& (1 - D_t) (W'_{p_1,t} + W'_{t,k_1}) + \\
& (1 - D_{\bar{t}}) (W'_{p_2,\bar{t}} + W'_{\bar{b},\bar{t}})) + \\
& W_{\bar{b},\bar{t}} (1 - C_{\bar{t}}) (W'_{\bar{b},k_1} + D_{\bar{t}} W'_{p_2,k_1} + D_t W'_{p_1,b} + \\
& (1 - D_{\bar{t}}) (W'_{p_2,\bar{t}} + W'_{t,k_1}) + \\
& (1 - D_t) (W'_{p_1,t} + W'_{b,t})) + \\
& W_{p_2,\bar{b}} C_{\bar{t}} (W'_{p_2,k_1} + D_t W'_{p_1,b} + W'_{\bar{b},k_1} + (1 - D_t) (W'_{p_1,t} + W'_{b,t})) \\
& W_{p_1,b} C_t (W'_{p_1,k_1} + D_{\bar{t}} W'_{p_2,\bar{b}} + W'_{b,k_1} + (1 - D_{\bar{t}}) (W'_{p_2,\bar{t}} + W'_{\bar{b},\bar{t}})) \\
& + \overline{\mathcal{F}}_{q\bar{q} \rightarrow t\bar{t}}.
\end{aligned}$$

Despite calculating the full pattern including subleading terms, owing to the size and number of terms of the full radiation pattern, we only show the leading N_C contribution in Eq. 3.1.31 and show numerically the comparison to the full result in Fig. 3.8.

We have included a remainder function, $\overline{\mathcal{F}}_{q\bar{q} \rightarrow t\bar{t}}$, in Eqn. 3.1.31 where

$$\begin{aligned}
\overline{\mathcal{F}}_{q\bar{q} \rightarrow t\bar{t}} = \frac{C_A^2}{4} [& W_{p_1,t} C_t (1 - D_t) (W'_{b,t} + W'_{t,k_1} - W'_{b,k_1}) + \\
& W_{p_2,\bar{t}} C_{\bar{t}} (1 - D_{\bar{t}}) (W'_{\bar{b},\bar{t}} + W'_{t,k_1} - W'_{\bar{b},k_1}) + \\
& W_{b,t} C_t (1 - D_t) (W'_{p_1,t} + W'_{t,k_1} - W'_{p_1,k_1}) + \\
& W_{\bar{b},\bar{t}} C_{\bar{t}} (1 - D_{\bar{t}}) (W'_{p_2,\bar{t}} + W'_{t,k_1} - W'_{p_2,k_1})].
\end{aligned} \tag{3.1.32}$$

We omit the remainder function as they have no light-parton collinear singularities, which unless the top is significantly boosted, means we have only a single soft logarithm here. However, these terms are also small from the competing nature of the C_t and $1 - D_t$ functions. Recalling that $k_1 \gg k_2$ as we are in the strongly ordered limit, and that $C_t = C_t(k_1)$ and $D_t = C_t(k_2)$, the competing nature of the C_t and

(a) $E_{k_1} = 100 \text{ GeV}$ $E_{k_2} = 5 \text{ GeV}$ (b) $E_{k_1} = 10 \text{ GeV}$ $E_{k_2} = 1 \text{ GeV}$ Figure 3.7: $C_t(1 - D_t)$ for different gluon energies.

$1 - D_t$ terms mean that is C_t if large, then $1 - D_t$ is small. Fig. 3.7 shows a plot of $C_t(1 - D_t)$ for gluons of varying energies displaying these properties.

The interpretation of this radiation pattern is more complicated than in the single gluon emission case, but guides us in developing our algorithm. The dipoles from the single emission case are suppressed by the same amount, and now multiplying them, is radiation from the second emission which is suppressed in a similar way as

in the single emission case. We see new dipoles formed by, for example, the incoming quark and outgoing gluon that are unsuppressed and dipoles formed by the outgoing gluon and top quark being suppressed by $(1 - D_t)$, and between the outgoing gluon and bottom quark by D_t .

Similarly the radiation pattern for $gg \rightarrow t\bar{t}gg$ is

$$\begin{aligned}
& \frac{\omega^2 \sum_{\text{spins}} |\mathcal{M}_0^n(\{p_0\})|^2 \mathcal{F}_n}{2 \sum_{\text{spins}} |\mathcal{M}_0(\{p_0\})|^2} = \tag{3.1.33} \\
& \frac{C_A^5}{16} h(t, s) [W_{p_1, t} (1 - C_t) (W'_{p_1, p_2} + W'_{p_1, k_1} + D_t W'_{b, k_1} + D_{\bar{t}} W'_{p_2, \bar{b}} + \\
& \quad (1 - D_t) (W'_{b, t} + W'_{t, k_1}) + \\
& \quad (1 - D_{\bar{t}}) (W'_{\bar{b}, \bar{t}} + W'_{p_2, \bar{t}}) + \\
& \quad W_{b, t} (1 - C_t) (W'_{p_1, p_2} + W'_{b, k_1} + D_t W'_{p_1, k_1} + D_{\bar{t}} W'_{p_2, \bar{b}} + \\
& \quad (1 - D_t) (W'_{p_1, t} + W'_{t, k_1}) + \\
& \quad (1 - D_{\bar{t}}) (W'_{p_2, \bar{t}} + W'_{b, \bar{t}}) + \\
& \quad W_{p_2, \bar{t}} (1 - C_{\bar{t}}) (W'_{p_1, p_2} + W'_{p_2, k_1} + D_{\bar{t}} W'_{b, k_1} + D_t W'_{p_1, b} + \\
& \quad (1 - D_{\bar{t}}) (W'_{b, \bar{t}} + W'_{t, k_1}) + \\
& \quad (1 - D_t) (W'_{b, t} + W'_{p_1, t})) + \\
& \quad W_{\bar{b}, \bar{t}} (1 - C_{\bar{t}}) (W'_{p_1, p_2} + W'_{b, k_1} + D_{\bar{t}} W'_{p_2, k_1} + D_t W'_{p_1, b} + \\
& \quad (1 - D_{\bar{t}}) (W'_{p_2, \bar{t}} + W'_{t, k_1}) + \\
& \quad (1 - D_t) (W'_{p_1, t} + W'_{b, t})) + \\
& \quad W_{p_2, \bar{b}} C_{\bar{t}} (W'_{p_2, k_1} + W'_{p_1, p_2} + W'_{b, k_1} + D_t W'_{p_1, b} + \\
& \quad (1 - D_t) (W'_{p_1, t} + W'_{b, t})) + \\
& \quad W_{p_1, b} C_t (W'_{p_1, k_1} + W'_{p_1, p_2} + W'_{b, k_1} + D_{\bar{t}} W'_{p_2, \bar{b}} + \\
& \quad (1 - D_{\bar{t}}) (W'_{p_2, \bar{t}} + W'_{b, \bar{t}}) + \\
& \quad W_{p_1, p_2} (W'_{p_1, k_1} + W'_{p_2, k_1} + (1 - D_{\bar{t}}) (W'_{p_2, \bar{t}} + W'_{b, \bar{t}}) + \\
& \quad (1 - D_t) (W'_{p_1, t} + W'_{b, t}) + D_t W'_{p_1, b} + D_{\bar{t}} W'_{p_2, \bar{b}})] \\
& + \frac{C_A^5}{16} h(u, s) [W_{p_1, \bar{t}} (1 - C_{\bar{t}}) (W'_{p_1, p_2} + W'_{p_1, k_1} + D_{\bar{t}} W'_{b, k_1} + D_t W'_{p_2, b} + \\
& \quad (1 - D_{\bar{t}}) (W'_{b, \bar{t}} + W'_{t, k_1}) + \\
& \quad (1 - D_t) (W'_{b, t} + W'_{p_2, t})) +
\end{aligned}$$

$$\begin{aligned}
& W'_{\bar{b},\bar{t}}(1 - C_{\bar{t}}) (W'_{p_1,p_2} + W'_{\bar{b},k_1} + D_{\bar{t}} W'_{p_1,k_1} + D_t W'_{p_2,b} + \\
& \quad (1 - D_{\bar{t}}) (W'_{p_1,\bar{t}} + W'_{\bar{t},k_1}) + \\
& \quad (1 - D_t) (W'_{p_2,t} + W'_{b,t})) + \\
& W'_{p_2,t} (1 - C_t) (W'_{p_1,p_2} + W'_{p_2,k_1} + D_t W'_{b,k_1} + D_{\bar{t}} W'_{p_1,\bar{b}} + \\
& \quad (1 - D_t) (W'_{b,t} + W'_{t,k_1}) + \\
& \quad (1 - D_{\bar{t}}) (W'_{\bar{b},\bar{t}} + W'_{p_1,\bar{t}})) + \\
& W'_{b,t} (1 - C_t) (W'_{p_1,p_2} + W'_{b,k_1} + D_t W'_{p_2,k_1} + D_{\bar{t}} W'_{p_1,\bar{b}} + \\
& \quad (1 - D_t) (W'_{p_2,t} + W'_{t,k_1}) + \\
& \quad (1 - D_{\bar{t}}) (W'_{p_1,\bar{t}} + W'_{\bar{b},\bar{t}})) + \\
& W'_{p_2,b} C_t (W'_{p_2,k_1} + W'_{p_1,p_2} + W'_{b,k_1} + D_{\bar{t}} W'_{p_1,\bar{b}} + \\
& \quad (1 - D_{\bar{t}}) (W'_{p_1,\bar{t}} + W'_{\bar{b},\bar{t}})) + \\
& W'_{p_1,\bar{b}} C_{\bar{t}} (W'_{p_1,k_1} + W'_{p_1,p_2} + W'_{\bar{b},k_1} + D_t W'_{p_2,b} + \\
& \quad (1 - D_t) (W'_{p_2,t} + W'_{b,t})) + \\
& W'_{p_1,p_2} (W'_{p_1,k_1} + W'_{p_2,k_1} + (1 - D_t) (W'_{p_2,t} + W'_{b,t}) + \\
& \quad (1 - D_{\bar{t}}) (W'_{p_1,\bar{t}} + W'_{\bar{b},\bar{t}}) + D_{\bar{t}} W'_{p_1,\bar{b}} + D_t W'_{p_2,b})] \\
& + \bar{\mathcal{F}}_{gg \rightarrow t\bar{t}}
\end{aligned}$$

As with the quark-quark case owing to the complexity of the full radiation pattern, we only show the leading N_C contribution in Eq. 3.1.33 and show numerically the comparison to the full result in Fig. 3.9. Here the remainder terms, $\bar{\mathcal{F}}_{gg \rightarrow t\bar{t}}$ are given by

$$\begin{aligned}
\bar{\mathcal{F}}_{gg \rightarrow t\bar{t}} = & \frac{C_A^5}{16} h(t, s) [W'_{p_1,t} C_t (1 - D_t) (W'_{b,t} + W'_{t,k_1} - W'_{b,k_1}) + \\
& W'_{b,t} C_t (1 - D_t) (W'_{p_1,t} + W'_{t,k_1} - W'_{p_1,k_1}) + \\
& W'_{p_2,\bar{t}} C_{\bar{t}} (1 - D_{\bar{t}}) (W'_{\bar{b},\bar{t}} + W'_{\bar{t},k_1} - W'_{\bar{b},k_1}) + \\
& W'_{\bar{b},\bar{t}} C_{\bar{t}} (1 - D_{\bar{t}}) (W'_{p_2,\bar{t}} + W'_{\bar{t},k_1} - W'_{p_2,k_1})] \\
& + \frac{C_A^5}{16} h(u, s) [W'_{p_1,\bar{t}} C_{\bar{t}} (1 - D_{\bar{t}}) (W'_{\bar{b},\bar{t}} + W'_{\bar{t},k_1} - W'_{\bar{b},k_1}) + \\
& W'_{\bar{b},\bar{t}} C_{\bar{t}} (1 - D_{\bar{t}}) (W'_{p_1,\bar{t}} + W'_{\bar{t},k_1} - W'_{p_1,k_1}) + \\
& W'_{p_2,t} C_t (1 - D_t) (W'_{b,t} + W'_{t,k_1} - W'_{b,k_1}) +
\end{aligned}$$

$$W_{b,t} C_t (1 - D_t) (W'_{p_2,t} + W'_{t,k_1} - W'_{p_2,k_1})].$$

which are omitted for exactly the same reasons as those in Eqn. 3.1.32.

The interpretation of this radiation pattern is similar to the $q\bar{q}$ case. The dipoles from the single emission case are suppressed by the same amount, and now multiplying them, is radiation from the second emission which is suppressed in a similar way as to the single case. We see new dipoles formed by, for example, the incoming quark and outgoing gluon that are unsuppressed and dipoles formed by the outgoing gluon and top quark being suppressed by $(1 - D_t)$, and between the outgoing gluon and bottom quark by D_t .

3.1.2 $e^+e^- \rightarrow t\bar{t}$

For the e^+e^- initiated process, the radiation pattern is [134]

$$\begin{aligned} \frac{\omega^2}{2} \mathcal{F} = C_F [& W_{t\bar{t}} (1 + C_{t\bar{t}} - C_t - C_{\bar{t}}) + W_{tb} (1 - C_t) + W_{t\bar{b}} (1 - C_{\bar{t}}) + W_{b\bar{b}} C_{t\bar{t}} + \\ & W_{\bar{t}b} (C_t - C_{t\bar{t}}) + W_{\bar{t}\bar{b}} (C_{\bar{t}} - C_{t\bar{t}})], \end{aligned} \quad (3.1.34)$$

and the new coefficient

$$C_{ij}(k) = M_i \Gamma_i M_j \Gamma_j [M_i \Gamma_i M_j \Gamma_j \pm q_i \cdot k q_j \cdot k] \frac{1}{M_i^2 \Gamma_i^2 + (q_i \cdot k)^2} \frac{1}{M_j^2 \Gamma_j^2 + (q_j \cdot k)^2}, \quad (3.1.35)$$

where the $+$ case is when both particles are in the hard process, and $-$ otherwise.

For the previous radiation patterns it was not necessary to decompose the dipole radiation functions into the two shower contributions. However doing so here allows us to extract a part of the $t\bar{t}$, tb and $t\bar{b}$ dipoles such that the collinear singularities in the interference term cancel. This gives

$$\begin{aligned} \frac{\omega^2}{2} \mathcal{F}_{e^+e^- \rightarrow t\bar{t}} = C_F [& (W_{t\bar{t}}^t + W_{t\bar{b}}^t) (1 - C_t) + (W_{t\bar{t}}^{\bar{t}} + W_{t\bar{b}}^{\bar{t}}) (1 - C_{\bar{t}}) + \\ & (1 - C_t) W_{t\bar{b}}^b + (1 - C_{\bar{t}}) W_{t\bar{b}}^{\bar{b}} + C_t W_{b\bar{b}}^b + C_{\bar{t}} W_{b\bar{b}}^{\bar{b}}] \\ & + \bar{\mathcal{F}}_{e^+e^- \rightarrow t\bar{t}}, \end{aligned} \quad (3.1.36)$$

where

$$\bar{\mathcal{F}}_{e^+e^- \rightarrow t\bar{t}} = C_F [(C_t - C_{t\bar{t}}) (W_{t\bar{b}}^b - W_{b\bar{b}}^b + W_{t\bar{b}}^{\bar{t}} - W_{t\bar{t}}^{\bar{t}}) + \quad (3.1.37)$$

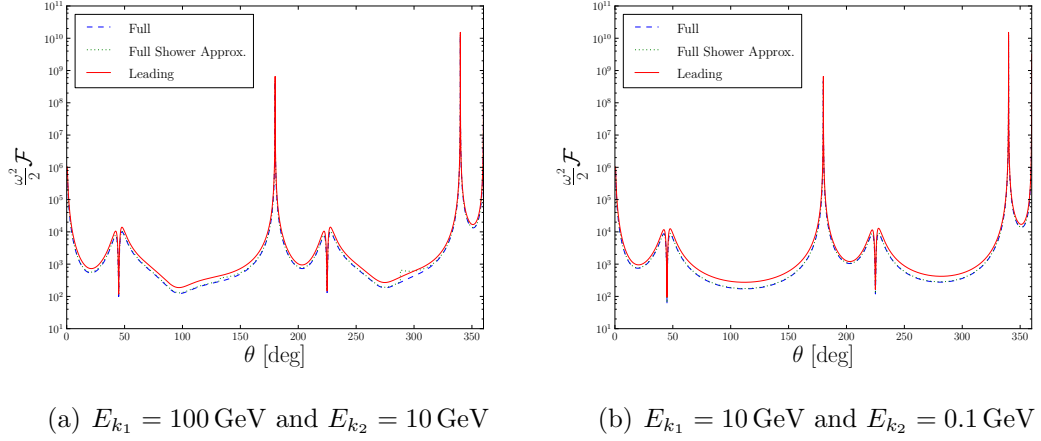


Figure 3.8: The radiation pattern for double emission from $q\bar{q} \rightarrow t\bar{t}$. We show the full radiation pattern, the shower approximation to the full radiation pattern and the leading N_C contribution. E_{k_1} is the energy of the gluon from the first emission and E_{k_2} is the energy of the gluon from the second emission.

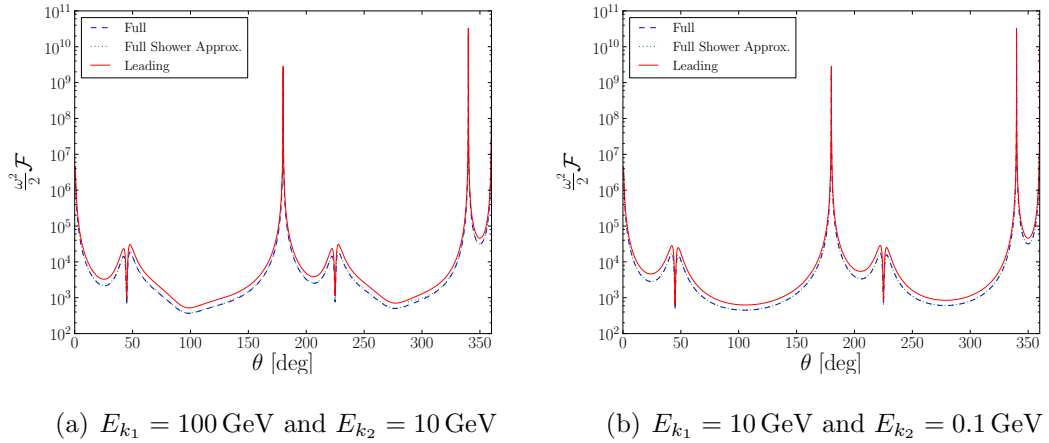


Figure 3.9: The radiation pattern for double emission from $gg \rightarrow t\bar{t}$. We show the full radiation pattern, the shower approximation to the full radiation pattern and the leading N_C contribution. E_{k_1} is the energy of the gluon from the first emission and E_{k_2} is the energy of the gluon from the second emission.

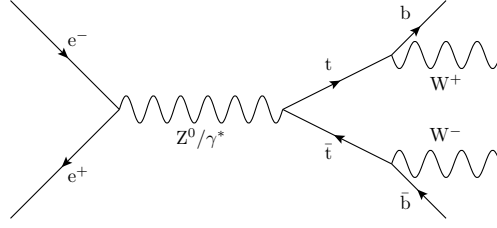
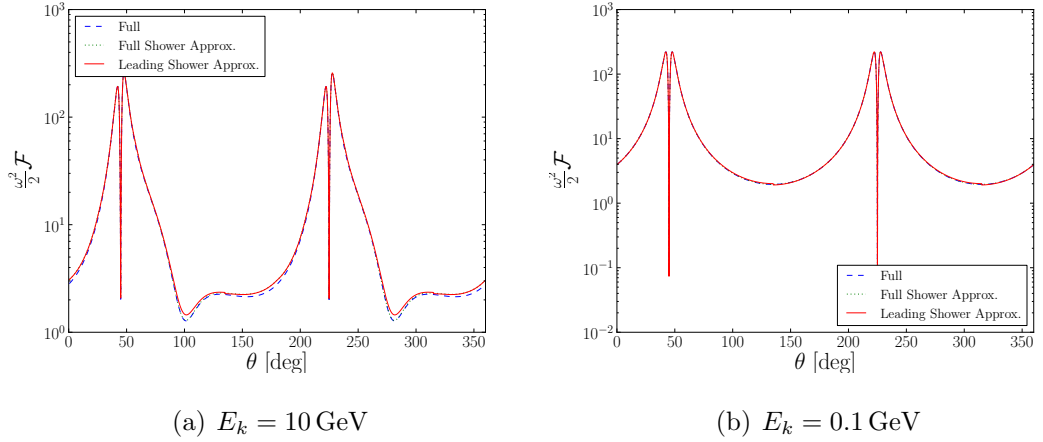
Figure 3.10: The production of top quarks by e^+e^- 

Figure 3.11: The radiation pattern for single gluon emission from e^+e^- collisions. We show the full radiation pattern, the shower approximation to the full radiation pattern and shower approximation with the interference terms neglected. These interference terms are so small, that this line lies on top of the shower approximation line.

$$(C_{\bar{t}} - C_{t\bar{t}}) \left(W_{t\bar{b}}^{\bar{b}} - W_{b\bar{b}}^{\bar{b}} + W_{t\bar{b}}^t - W_{t\bar{t}}^t \right).$$

The radiation pattern produced from this process is shown in Fig. 3.11. We can interpret this radiation pattern as the radiation from the top anti-top and top bottom dipoles being suppressed by $(1 - C_t)$ with the radiation from the bottom quarks being suppressed by a similar amount. The same applies for the anti-particles, but with $(1 - C_{\bar{t}})$. There is additional soft radiation from the bottom anti-bottom quark dipole with radiation suppressed by C_t , or $C_{\bar{t}}$ depending on whether it is the bottom or anti-bottom radiating the gluon. We discard the remainder function, $\overline{\mathcal{F}}_{e^+e^- \rightarrow t\bar{t}}$ as it contains no collinear singularities and is therefore suppressed in the collinear limit.

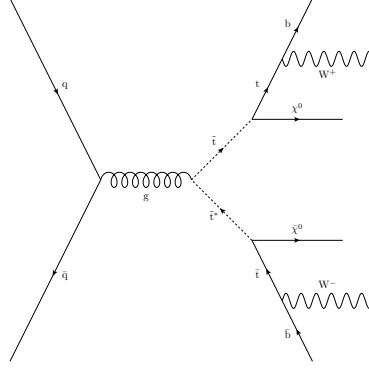


Figure 3.12: The production of stop quarks by the $q\bar{q}$ initiated processes.

3.2 SUSY Processes

We now turn our attention to SUSY processes, notably production of stop squarks. The fact that there are now two heavy particles occurring in a decay chain means that an extra width and mass scale has been introduced over the previous section, notably the stop squark width and mass. Understanding radiation patterns involving a decay chain of heavy particles will guide us in developing the algorithm for more complicated processes such as these.

3.2.1 $q\bar{q} \rightarrow \tilde{t}\tilde{t}^*$

Using a similar approach as in Section 3.1.2, and defining in this case

$$\mathcal{F} \equiv \left(\frac{M_t\Gamma_t}{\pi}\right)^2 \left(\frac{M_{\tilde{t}}\Gamma_{\tilde{t}}}{\pi}\right)^2 \int dq_t^2 dq_{\tilde{t}}^2 dq_{\tilde{t}^*}^2 dq_{t^*}^2 [-J \cdot J^*], \quad (3.2.38)$$

we find the radiation patterns for processes involving two heavy particles decaying. Below, we set the kinematics as in Fig. 3.3, except we now have the top squarks moving perpendicular to the beam direction, with the top quarks at -20° from the stops and the bottom quarks at -45° from the stops *i.e.* -25° from the tops. We assume $m_{\tilde{t}} = 400$ GeV, $\Gamma_{\tilde{t}} = 0.57$ GeV and $m_{\chi^0} = 50$ GeV.

The leading N_C contribution to the radiation pattern is

$$\begin{aligned} \frac{\omega^2}{2} \mathcal{F}_{q\bar{q} \rightarrow \tilde{t}\tilde{t}^*} = \frac{C_A}{2} [& (W_{t,b}^t + W_{t,\tilde{t}}^t)(1 - C_t) + (W_{p_1,\tilde{t}}^{\tilde{t}} + W_{\tilde{t},t}^{\tilde{t}})(1 - C_{\tilde{t}}) + \\ & W_{t,b}^b(1 - C_t) + W_{p_1,\tilde{t}}^{p_1}(1 - C_{\tilde{t}}) + C_t W_{p_1,b}^b + C_{\tilde{t}} W_{p_1,b}^{p_1} + \end{aligned} \quad (3.2.39)$$

$$\begin{aligned}
& (W_{\bar{t},\bar{b}}^{\bar{t}} + W_{\bar{t},\bar{t}^*}^{\bar{t}}) (1 - C_{\bar{t}}) + (W_{p_2,\bar{t}^*}^{\bar{t}^*} + W_{\bar{t}^*,\bar{t}}^{\bar{t}^*}) (1 - C_{\bar{t}^*}) + \\
& W_{\bar{t},\bar{b}}^{\bar{b}} (1 - C_{\bar{t}}) + W_{p_2,\bar{t}^*}^{p_2} (1 - C_{\bar{t}^*}) + C_{\bar{t}} W_{p_2,\bar{b}}^{\bar{b}} + C_{\bar{t}^*} W_{p_2,\bar{b}}^{p_2} \Big] + \\
& + \overline{\mathcal{F}}_{q\bar{q} \rightarrow \bar{t}\bar{t}^*},
\end{aligned}$$

and is shown in Fig. 3.13. We see similar features as to the patterns shown earlier, with the dips in the pattern associated with the finite mass of the bottom quarks. This radiation pattern can be interpreted in a similar way as before with the radiation from the top stop dipole and top bottom dipoles being suppressed by $(1 - C_t)$. There is similar suppression between the incoming quark and stop dipole and stop top dipole with a suppression factor of $(1 - C_{\bar{t}})$ and similarly for the anti particles but with $(1 - C_{\bar{t}})$ or $(1 - C_{\bar{t}^*})$ depending on whether it is the top quark or top squark. There is then additional soft radiation between the bottom and incoming quark dipole suppressed by C_t or $C_{\bar{t}}$ depending on whether the radiation is from the incoming quark or bottom. There is a similar suppression for the anti-particles but with the obvious replacements of the C_i functions.

The remainder function, $\mathcal{F}_{q\bar{q} \rightarrow \bar{t}\bar{t}^*}$ is given by

$$\begin{aligned}
\overline{\mathcal{F}}_{q\bar{q} \rightarrow \bar{t}\bar{t}^*} = & \frac{C_A}{2} \Big[(C_t - C_{t\bar{t}}) (W_{\bar{t},b}^{\bar{t}} - W_{\bar{t},t}^{\bar{t}} - W_{p_1,b}^b + W_{\bar{t},b}^b) + \\
& (C_{\bar{t}} - C_{\bar{t}\bar{t}}) (W_{p_1,t}^t - W_{\bar{t},\bar{t}}^t - W_{p_1,b}^{p_1} + W_{p_1,t}^{p_1}) + \\
& (C_{\bar{t}} - C_{\bar{t}\bar{t}^*}) (W_{\bar{t}^*,\bar{b}}^{\bar{t}^*} - W_{\bar{t}^*,\bar{t}}^{\bar{t}^*} - W_{p_2,\bar{b}}^{\bar{b}} + W_{\bar{t}^*,\bar{b}}^{\bar{b}}) + \\
& (C_{\bar{t}^*} - C_{\bar{t}\bar{t}^*}) (W_{p_2,\bar{t}}^{\bar{t}} - W_{\bar{t},\bar{t}^*}^{\bar{t}} - W_{p_2,\bar{b}}^{p_2} + W_{p_2,\bar{t}}^{p_2}) \Big],
\end{aligned} \tag{3.2.40}$$

which like the $e^+e^- \rightarrow t\bar{t}$ process contains no collinear singularities and is therefore discarded in terms of interpretation in a Monte Carlo event generator.

3.2.2 $e^+e^- \rightarrow \bar{t}\bar{t}^*$

The Feynman diagram for this process is shown in Fig. 3.14. We have divided by the leading order colour factor and so the radiation pattern for this process is

$$\begin{aligned}
\frac{\omega^2}{2} \mathcal{F}_{e^+e^- \rightarrow \bar{t}\bar{t}^*} = & (1 - C_t) (W_{b,t}^t + W_{\bar{t},\bar{t}}^t) + (1 - C_{\bar{t}}) (W_{\bar{b},\bar{t}}^{\bar{t}} + W_{\bar{t},\bar{t}^*}^{\bar{t}}) + \\
& (1 - C_{\bar{t}}) (W_{\bar{t},\bar{t}}^{\bar{t}} + W_{\bar{t},\bar{t}^*}^{\bar{t}}) + (1 - C_{\bar{t}^*}) (W_{\bar{t},\bar{t}^*}^{\bar{t}^*} + W_{\bar{t},\bar{t}^*}^{\bar{t}^*}) + \\
& (1 - C_t) W_{b,t}^b + (1 - C_{\bar{t}}) W_{\bar{b},\bar{t}}^{\bar{b}} + W_{b,\bar{b}}^b C_t + W_{\bar{b},\bar{b}}^{\bar{b}} C_{\bar{t}} + \overline{\mathcal{F}}_{e^+e^- \rightarrow \bar{t}\bar{t}^*},
\end{aligned} \tag{3.2.41}$$

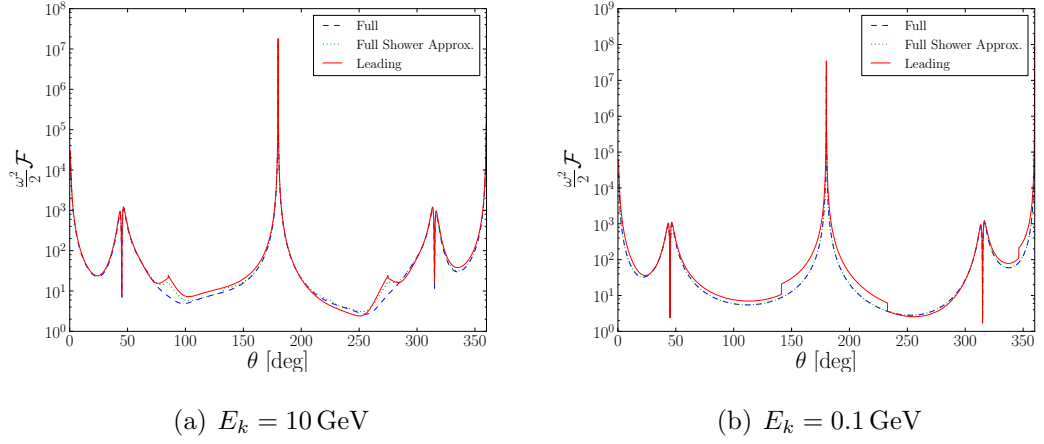


Figure 3.13: The radiation pattern for single emission from $q\bar{q} \rightarrow t\bar{t}^*$. We show the full radiation pattern, the shower approximation to the full radiation pattern and the leading N_C contribution. E_k is the energy of the emitted gluon.

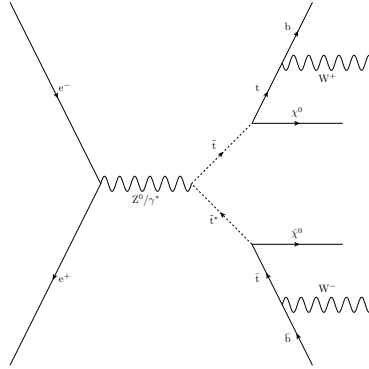


Figure 3.14: The production of stop quarks in e^+e^- collisions.

which is written as a leading contribution and a remainder function that contains no collinear singularities, $\overline{\mathcal{F}}_{e^+e^- \rightarrow t\bar{t}^*}$, which we can see from

$$\begin{aligned}
 \overline{\mathcal{F}}_{e^+e^- \rightarrow t\bar{t}^*} = & C_t \left[C_{t\bar{t}} C_{t^*} \left(W_{b,t}^{\bar{b}} + W_{b,\bar{t}}^{\bar{t}} + W_{b,t}^t + W_{b,\bar{t}}^b - \right. \right. & (3.2.42) \\
 & \left. \left. W_{b,\bar{b}}^{\bar{b}} - W_{b,\bar{b}}^b - W_{t,\bar{t}}^{\bar{t}} - W_{t,\bar{t}}^t \right) + \right. \\
 & C_{t\bar{t}^*} C_{\bar{t}} \left(W_{b,\bar{b}}^{\bar{b}} + W_{b,\bar{b}}^b + W_{t,\bar{t}}^{\bar{t}} + W_{t,\bar{t}}^t - \right. \\
 & \left. \left. W_{b,t}^{\bar{b}} - W_{b,\bar{t}}^{\bar{t}} - W_{b,t}^t - W_{b,\bar{t}}^b \right) + \right. \\
 & \left. C_{t\bar{t}^*} \left(W_{b,\bar{t}}^{\bar{t}} + W_{b,\bar{t}}^b + W_{t,\bar{t}^*}^{\bar{t}^*} + W_{t,\bar{t}^*}^t - \right. \right.
 \end{aligned}$$

$$\begin{aligned}
& \left. \begin{aligned} & W_{t,\tilde{t}}^{\bar{t}} + W_{t,\tilde{t}}^t + W_{\tilde{t},\tilde{t}^*}^{\tilde{t}^*} + W_{\tilde{t},\tilde{t}^*}^{\tilde{t}} - \\ & W_{\tilde{t},\tilde{t}}^{\bar{t}} - W_{\tilde{t},\tilde{t}}^{\tilde{t}} - W_{\tilde{t},\tilde{t}^*}^{\tilde{t}^*} - W_{\tilde{t},\tilde{t}^*}^t \end{aligned} \right] + \\
& C_{\tilde{t}\tilde{t}^*} \left(W_{\tilde{b},\tilde{t}}^{\bar{b}} + W_{\tilde{b},\tilde{t}}^{\tilde{t}} + W_{\tilde{t},\tilde{t}^*}^{\bar{t}} + W_{\tilde{t},\tilde{t}^*}^{\tilde{t}^*} - \right. \\
& \quad \left. W_{\tilde{t},\tilde{t}}^{\tilde{t}} - W_{\tilde{b},\tilde{t}^*}^{\bar{b}} - W_{\tilde{b},\tilde{t}^*}^{\tilde{t}^*} - W_{\tilde{t},\tilde{t}}^{\bar{t}} \right) + \\
& C_{t\tilde{t}} \left(W_{\tilde{b},\tilde{t}^*}^{\tilde{t}^*} + W_{\tilde{b},\tilde{t}^*}^b + W_{t,\tilde{t}}^{\tilde{t}} + W_{t,\tilde{t}}^t - \right. \\
& \quad \left. W_{t,\tilde{t}^*}^t - W_{\tilde{b},\tilde{t}}^{\tilde{t}} - W_{\tilde{b},\tilde{t}}^b - W_{t,\tilde{t}^*}^{\tilde{t}^*} \right).
\end{aligned}$$

We therefore discard this remainder function in interpreting and implementing the radiation patterns in terms of a Monte Carlo event generator. A plot for this process is shown in Fig. 3.15, where the radiation pattern is dominated by the outgoing partons with the remaining feature at around 90° being from radiation from the top stop dipole.

Here radiation from the top and stop quarks in their production and decay is suppressed by $(1 - C_t)$ and $(1 - C_{\tilde{t}})$ respectively. Finally there is soft radiation from the dipole formed by the bottom and anti-bottom quarks which is suppressed by C_t or $C_{\tilde{t}}$ depending on which quark is emitting.

3.3 Algorithm

Improving the simulation of radiation in heavy particle production and decay in a Monte Carlo event generator requires an algorithm based on the interpretation of the radiation patterns above. From the radiation patterns, with special note to the double emission radiation patterns in Eqs. 3.1.31 and 3.1.33, we see that particles still colour connected to the unstable particle have their radiation suppressed by a factor $(1 - C_i)$, where i is the heavy particle, in the simulation of QCD radiation in the production and decay of heavy particles. Finally there is a new soft contribution with radiation from the dipole formed by parent and decay products of the unstable particle where the probability of radiation is proportional to C_i . Here the parent is either the colour connected incoming particle for an unstable particle produced in the hard process or in the case of an unstable particle produced in the decay of

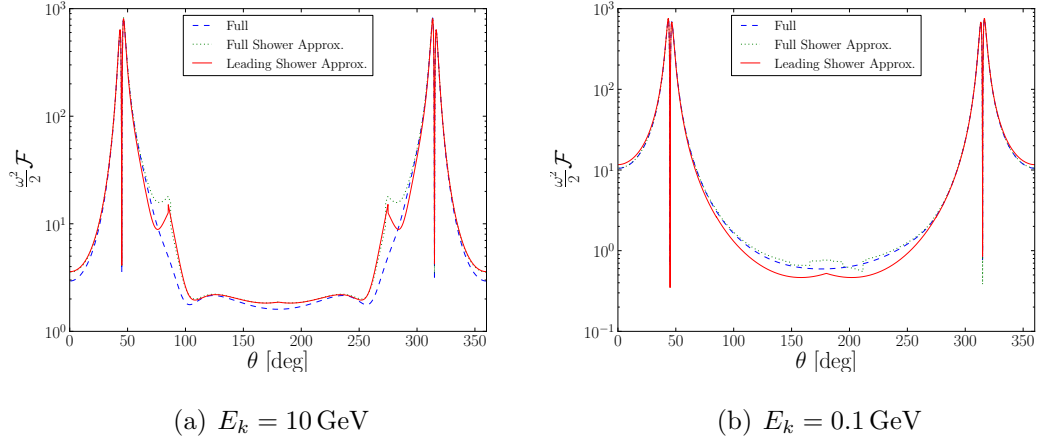


Figure 3.15: The radiation pattern for single gluon emission from e^+e^- collisions producing top squarks. We show the full radiation pattern, the shower approximation to the full radiation pattern and shower approximation with the interference terms neglected.

a heavier particle the heavy particle. In the case of the unstable colour connected particles as in $e^+e^- \rightarrow t\bar{t}$ the decay products are colour connected. Below we refer to the first stage of the shower as the “hard” shower and the soft remaining piece as the “soft” shower.

Referring to the example of top production, we therefore modify the Sudakov form factor to include the appropriate suppression factor $S(C_t)$, *i.e.* the new Sudakov form factor is

$$\Delta_{\tilde{i}j \rightarrow ij}(\tilde{q}, \tilde{q}_h) = \exp \left\{ - \int_{\tilde{q}}^{\tilde{q}_h} \frac{d\tilde{q}'^2}{\tilde{q}'^2} \int dz \frac{\alpha_S(z, \tilde{q}')}{2\pi} S(C_t) P_{\tilde{i}j \rightarrow ij}(z, \tilde{q}') \right\}. \quad (3.3.43)$$

This can be implemented as an additional step in the veto algorithm [49] which is used to calculate the Sudakov form factor and generate radiation in most Monte Carlo event generators. Therefore, during the shower process, we accept the radiation off a particle colour connected to the top quark during the “hard” shower using the veto algorithm, such that we accept the radiation according to $S(C_t) = 1 - C_t > \mathcal{R}$, where the uniform random number \mathcal{R} is between $[0, 1]$. If the particle is not colour connected to the top quark, then $S(C_t) = 1$ and the standard shower algorithm applies.

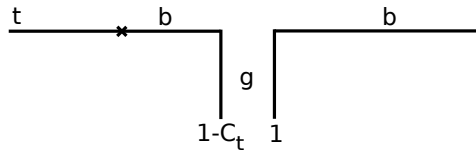


Figure 3.16: The probabilities of radiation from the colour lines of a gluon undergoing secondary radiation of a gluon whilst colour connected to a top and bottom in this example.

Secondary radiation from gluons requires a slightly different treatment. We apply the new Sudakov form factor with suppression factor $S(C_t) = \frac{1}{2}(2 - C_t)$ but then, we choose which colour line radiates according to the new probabilities and $1 - C_t$ and 1 depending on which line is colour connected to the top quark as shown in Fig. 3.16.

At the end of the shower, a new “soft” shower is constructed using the particles that terminate the top quark’s colour lines and applying the correction of $S(C_t) = C_t$ to radiation during this process.

3.4 Results

The effects of the new multi-scale shower were tested by observing the effect on the reconstructed top quark mass. The Rivet [101] system was used. The in-built MC_TTBAR analysis proceeds by looking for a semi-leptonically decaying W boson and:

- require a charged lepton, $p_T > 30$ GeV;
- require $E_T > 30$ GeV;
- rejecting any event with less than 4 jets, where each jet has $p_T > 30$ GeV, and the hardest has $p_T > 60$ GeV and the second hardest has $p_T > 50$ GeV;
- require two b-tagged jets, where 100% efficiency is assumed;
- require the two light jets to reconstruct the W boson mass.

As the top mass is not known a priori, the b-tagged jets are combined into pairs and the mass of the pairs binned. The results of this analysis are shown in Fig. 3.17. We see a suppression in the top mass spectrum with hadronization switched off and the new multi-scale shower switched on, but the effect of the new multi-scale shower are degraded upon the inclusion of hadronization effects. This is not unsurprising as hadronization is a model dependent process and introduces a coarse graining compared to the parton-level simulation.

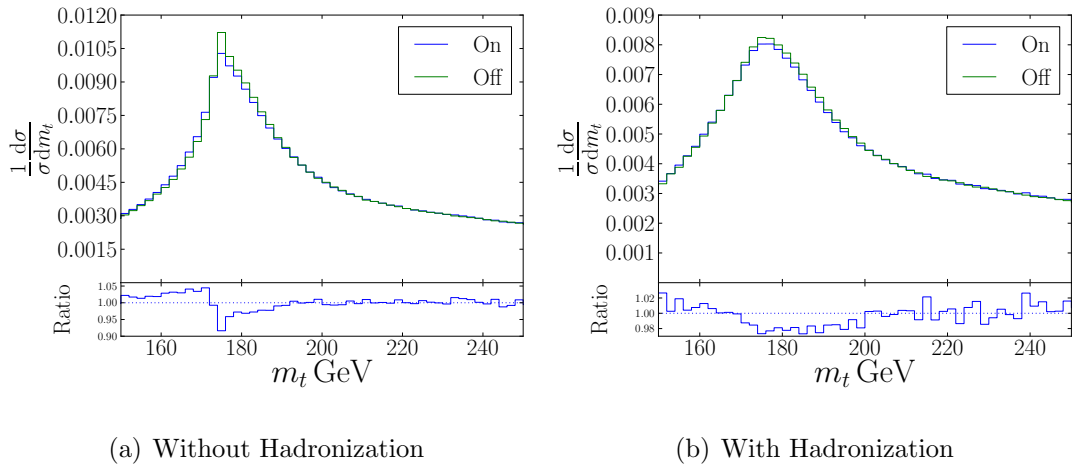


Figure 3.17: A plot showing the effects of the new multi-scale shower with and without hadronization on the top mass using the Rivet MC_TTBAR analysis.

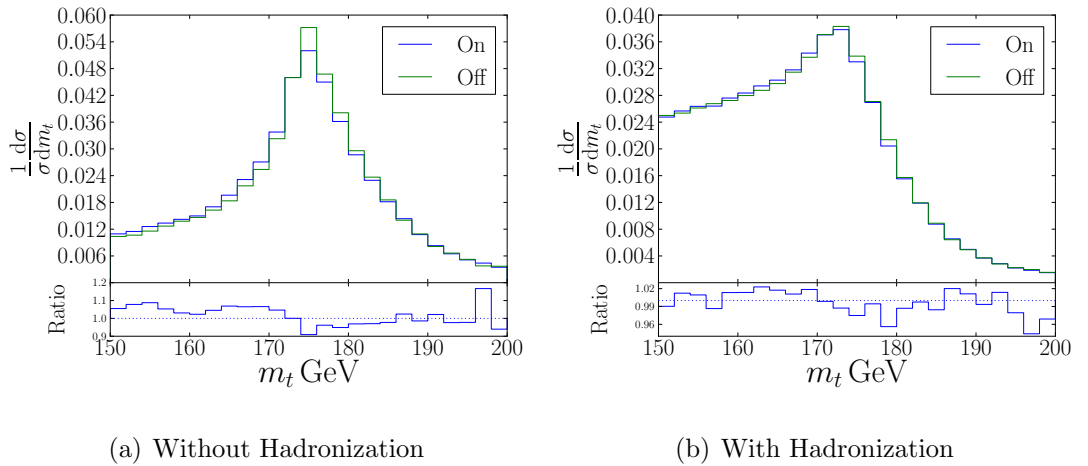


Figure 3.18: A plot showing the effects of the new multi-scale shower with and without hadronization on the top mass using the HEPTopTagger analysis.

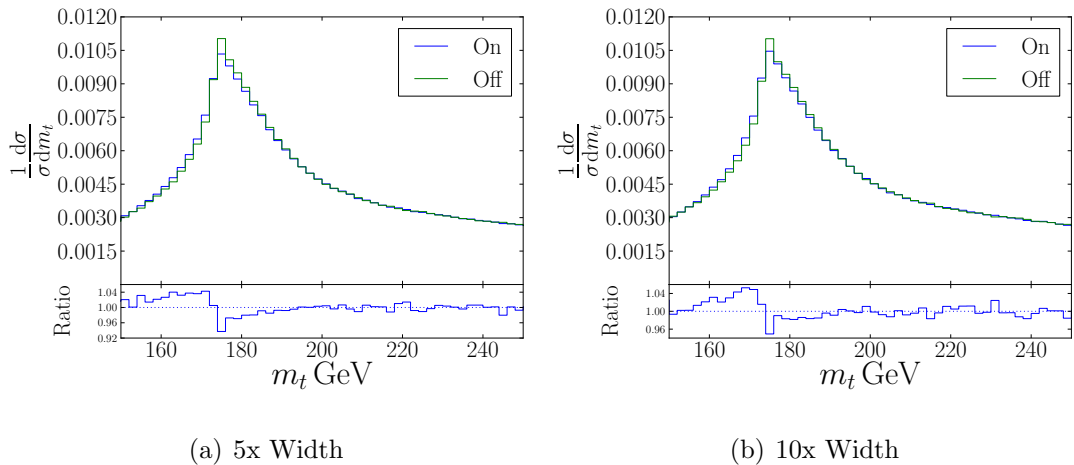


Figure 3.19: A plot showing the effects of the new multi-scale shower without hadronization and with increasing width on the top mass using the Rivet MC_TTBAR analysis.

We also examined the use of the **HEPTopTagger** algorithm as described in Refs. [78, 135]. There, the analysis proceeds by using the Cambridge/Aachen algorithm using $R = 1.5$ and:

- require two or more hard jets and a lepton where the jet satisfies $p_{T\text{jet}} > 200 \text{ GeV}$, $|y_{\text{jet}}| < 4$, and the lepton satisfies $p_{T\text{lepton}} > 15 \text{ GeV}$ and $|y_{\text{jet}}| < 2.5$;
- require one or two of the jets to pass the top tagger and if two pass, the one whose top candidate mass is closest to the top mass is chosen.

A window of $150 \rightarrow 200 \text{ GeV}$ was chosen for the top mass in the **HEPTopTagger** algorithm.

We show the results of this analysis in Fig. 3.18 where we see a slight change around the top mass peak both with and without hadronization on, but hadronization significantly reduces the effect of the inclusion of the new multi-scale shower. We also show the effects of increasing the width on the MC_TTBAR analysis in Fig. 3.19.

To investigate the effects on larger decay chains as found in some BSM models, we simulated a Little Higgs model with heavy top quark production, where the two

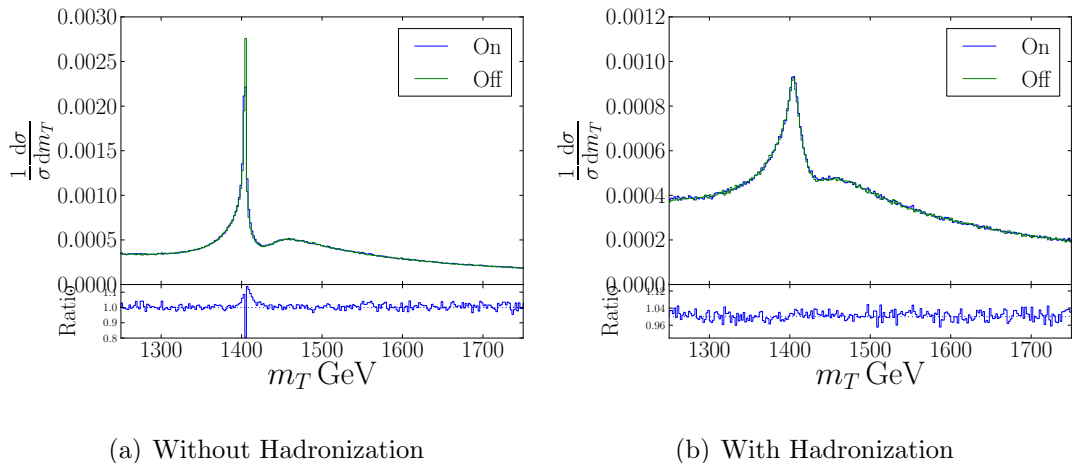


Figure 3.20: A plot showing the effects of the new multi-scale shower with and without hadronization on the heavy top quark mass in a Little Higgs model using a similar analysis to the Rivet MC_TTBAR analysis.

heavy top quarks decay into two SM top quarks. We assumed the mass of the heavy top quarks to be 1400 GeV. The analysis proceeds in a similar way to the Rivet MC_TTBAR analysis and results are shown in Fig. 3.20.

We see that there is an effect at the parton level, *i.e.* without hadronization but again, hadronization significantly reduces the effect of the inclusion of the new multi-scale shower.

3.5 Conclusions

In this chapter we have outlined radiation patterns for single gluon emission for top and stop production processes relevant to both the LHC and a future lepton collider. We have also shown new results for radiation patterns for double gluon emission for top production processes relevant to the LHC. We have also seen that the leading colour approximation that we employ in our Monte Carlo event generators is actually a good approximation, as the leading colour contribution is often very similar to the full fixed order calculation. This in practice means that we can have faith that our existing Monte Carlo event generator is delivering an accurate simulation of aspects of the radiation and can be used for studies at modern collider experiments. This

does not mean that efforts should not be undertaken to improve the simulation though, as any increase in accuracy will be beneficial given the highly complex hadronic final states at the LHC.

The existing single and new double gluon emission radiation patterns have been interpreted in terms of a Monte Carlo event generator by the means of a new multi-scale shower where, radiation is suppressed off particles colour connected to heavy decaying particles by means of a modification to the Sudakov form factor. This takes the form of a “hard” shower which runs in the place of the usual shower and a new “soft” shower that is run at the end of the “hard” showering process and effects only the particles that terminate the top quark’s colour lines.

The new shower was implemented in the Monte Carlo event generator **Herwig++** and the effects on some observables were shown. With the new multi-scale shower, the top mass is shown to be clearly altered with hadronization effects switched off, but upon turning hadronization on in the shower, the effect of the new multi-scale shower is reduced. The same applies for heavy top quark production in the Little Higgs model where the effect of the new multi-scale shower on the determination of the mass of the heavy top quark is negligible when hadronization is turned on. The small effect that this new aspect of simulation introduces can be thought of as reassuring that our existing tools are already providing a high quality level of simulation.

The multi-scale shower may nevertheless still prove important in certain observables and in the accurate simulation of new Physics beyond the Standard Model, where heavy, unstable particle production dominates. In further work it would be enlightening to see how these effects behave in other processes such as single top quark production, which is used to probe the Electroweak interaction, especially as this is currently being studied at the LHC.

Chapter 4

Colour Sextet Diquark

Phenomenology

Many models of Beyond the Standard Model (BSM) physics require the inclusion of diquarks. For example, diquarks appear in a number of Grand Unified Theories (GUTs) and have even been postulated as a form of dynamical symmetry breaking, giving rise to the masses of particles, [136, 137]. The colour sextet diquark is, in group theory language, a rank 2 symmetric tensor formed from the direct product of two fundamental representations $\mathbf{3} \otimes \mathbf{3} = \mathbf{6} \oplus \bar{\mathbf{3}}$. As such it is the lowest colour representation which has not been observed and therefore investigation of sextet diquark production at the CERN Large Hadron Collider (LHC) is interesting in its own right.

The LHC experiments are data taking at the high energy frontier ($\sqrt{s} = 8 \text{ TeV}$), allowing probes of energy scales not previously seen. At the LHC because the fundamental collisions are between the quarks and gluons inside the colliding protons the strong force is the dominant interaction allowing Quantum Chromodynamics (QCD) to be studied at these new high energies. As a diquark is produced via strong interactions, and with the potential of a relatively low mass, diquarks may be seen in the early stages of LHC data taking. The LHC also favours the formation of diquarks from the valence quarks as it is a proton-proton collider as opposed to a proton-antiproton collider, such as the Tevatron.

Due to their exotic colour structure and $SU(3)_C$ quantum numbers, diquarks will

give rise to jets in the detector. The expected signals will be either a resonance in the invariant dijet mass distribution or the production of two equal mass dijet systems in four jet events in the case of pair production. In order to study the experimental signatures of diquark production, a Monte Carlo simulation is required that includes the production of sextet particles, their perturbative decays and the full Monte Carlo machinery of showering (including the exotic colour structure) and hadronization.

Although significant efforts have been made to study the resonant production of diquarks [138–145] and also pair production [140, 146, 147], a full study of experimental signatures including Monte Carlo simulations has not been performed. In this chapter, we discuss: the implementation of the diquark model in general purpose Monte Carlo event generators; place constraints on the coupling as a function of mass based on the latest ATLAS results [3, 4]; present some results of invariant mass distributions both for resonant and pair production.

In the remainder of this chapter a method for simulating the production and decay of particles in the sextet representation of $SU(3)_C$ including the simulation of QCD radiation is presented. The colour decomposition is shown in detail for both the hard process and the shower.

Results from the Monte Carlo simulation of sextet diquark production at the LHC including both resonant and pair production are detailed. Limits on resonant diquark production from ATLAS results are shown and the first simulation studies of the less model dependent pair production mechanism is also performed.

4.1 Simulation

4.1.1 Lagrangian

As with all models, the simulation starts with the calculation of the hard production and decay processes using the most general Lagrangian for the coupling of the sextet particles to the quarks [139, 141, 144, 148, 149]

$$\begin{aligned} \mathcal{L} = & (g_{1L}\bar{q}_L^c i\tau_2 q_L + g_{1R}\bar{u}_R^c d_R) \Phi_{1,1/3} + g'_{1R}\bar{d}_R^c d_R \Phi_{1,-2/3} + g''_{1R}\bar{u}_R^c u_R \Phi_{1,4/3} + \\ & g_{3L}\bar{q}_L^c i\tau_2 \tau q_L \cdot \Phi_{3,1/3} + g_2\bar{q}_L^c \gamma_\mu d_R V_{2,-1/6}^\mu + g'_2\bar{q}_L^c \gamma_\mu u_R V_{2,5/6}^\mu + h.c., \end{aligned} \quad (4.1.1)$$

where q_L is the left-handed quark doublet, u_R and d_R are the right-handed quark singlet fields, and $q^c \equiv C\bar{q}^T$ is the charge conjugate quark field. The colour and generation indices are omitted to give a more compact notation and the subscripts on the scalar, Φ , and vector, V^μ , fields denote the SM electroweak gauge quantum numbers: $(SU(2)_L, U(1)_Y)$. The Lagrangian is assumed to be flavour diagonal to avoid any flavour changing currents arising from the new interactions.

The kinetic and QCD terms in the Lagrangian are

$$\mathcal{L}_{\text{QCD}}^{\text{scalar}} = D^\mu \Phi D_\mu \Phi - m^2 \Phi \Phi^\dagger, \quad (4.1.2a)$$

for scalar diquarks, where Φ is the scalar diquark field and

$$\mathcal{L}_{\text{QCD}}^{\text{vector}} = -\frac{1}{4} (D^\mu V^\nu - D^\nu V^\mu) (D_\mu V_\nu - D_\nu V_\mu) - m^2 V^\mu V_\mu, \quad (4.1.2b)$$

for vector diquarks, where V^μ is the vector diquark field. The covariant derivative D^μ has the standard form for Quantum Chromodynamics.

As discussed in the introduction, the simulation of perturbative QCD radiation, relies on the large number of colours, N_C , limit for both the treatment of perturbative QCD radiation and the subsequent hadronization. In this approach particles in the fundamental representation of $SU(N_C)$ carry a colour, those in the antifundamental representation an anticolour and those in the adjoint representation both a colour and an anticolour.

This is complicated in models involving sextet particles where in the large- N_C limit the sextet particles possess two fundamental colours, appropriately symmetrized. This cannot be handled by conventional Monte Carlo simulations which require all the colours of the particles to have fundamental colours and/or anticolours. In order to simulate these particles we choose to represent (anti)sextet particles as having two (anti)colours.

Consider the production and subsequent decay of a scalar sextet particle. In order to simulate QCD radiation from the intermediate sextet resonance we have to simulate the production and decay separately. The matrix element for the process is

$$\mathcal{M} = \mathcal{M}_{i\text{prod}} \frac{i\delta_j^i}{p^2 - m^2} \mathcal{M}_{\text{decay}}^j \quad (4.1.3)$$

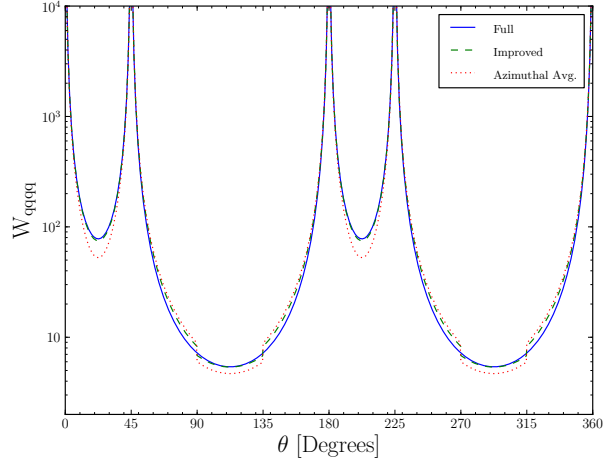


Figure 4.1: The radiation pattern associated with gluon emission from the incoming and outgoing quarks during resonant production, where θ is the polar angle of the gluon with respect to the z -axis.

where i, j are colour indices of the sextet particle, $\mathcal{M}_{i\text{prod}}$ is the matrix element for the production of a scalar sextet particle with colour i , four-momentum p and mass m , and $\mathcal{M}_{\text{decay}}^j$ is the matrix element for the decay of a scalar sextet particle with colour j .

This can be rewritten using $\delta_j^i = K_{ab}^i \bar{K}_j^{ba}$ where K and \bar{K} are the Clebsch-Gordan coefficients in the sextet and antisextet representations, respectively. Hence

$$\mathcal{M} = \mathcal{M}_{i\text{prod}} \frac{i K_{ab}^i \bar{K}_j^{ba}}{p^2 - m^2} \mathcal{M}_{\text{decay}}^j = \mathcal{M}'_{ab\text{prod}} \frac{i}{p^2 - m^2} \mathcal{M}'^{ba}_{\text{decay}}. \quad (4.1.4)$$

In order to consider the intermediate sextet particle as having two fundamental colours we have absorbed the Clebsch-Gordan into the redefined production, $\mathcal{M}'_{ab\text{prod}}$, and decay matrix elements, $\mathcal{M}'^{ba}_{\text{decay}}$. The Clebsch-Gordan coefficients and the associated generators are given in Ref. [138], and we will make use of them to decompose the colour of the production processes and shower, below.

From this, the colour partners of the decay products can be determined and the usual angular ordering procedure applied [42, 51]. The radiation pattern of gluons from the quarks for the resonant production of diquarks,

$q(p_1)q(p_2) \rightarrow \{\Phi, V\} \rightarrow q(p_3)q(p_4)$, is

$$J^2 = C_F \left[(W_{13} + W_{14} + W_{23} + W_{24}) \right. \\ \left. + \frac{2}{N_C + 1} \left[\frac{1}{2} (W_{13} + W_{14} + W_{23} + W_{24}) - W_{12} - W_{34} \right] \right]. \quad (4.1.5)$$

The last term in Eqn. 4.1.5 can be neglected, as usual, due to both the $\frac{1}{N_C}$ suppression, compared to the leading term, and the dynamical suppression in the massless limit because there is no collinear singularity in this term. The radiation pattern is shown in Fig. 4.1. The massless limit was used and so the momenta of the partons may be written as

$$\begin{aligned} p_1 &= E (1; 0, 0, 1) & p_3 &= E (1; -\sin \theta, 0, -\cos \theta) \\ p_2 &= E (1; 0, 0, -1) & p_4 &= E (1; \sin \theta, 0, \cos \theta) \\ k &= \omega (1; \cos \phi_k \sin \theta_k, \sin \phi_k \sin \theta_k, \cos \theta_k) . \end{aligned} \quad (4.1.6)$$

The outgoing quarks were held at 45° and 225° with respect to the incoming beam direction. The full radiation pattern, the result after neglecting the subleading terms and azimuthally averaging, and the improved angular ordered result, where the full result is used instead of the azimuthal average inside the angular-ordered region, are shown. Improved angular ordering, as implemented in `Herwig++` performs well in the collinear limit.

4.1.2 Colour Decomposition

As we mentioned in the introduction, owing to the fact that `Herwig++`, as with all general purpose Monte Carlo generators, has all the machinery set up to work with the (anti)fundamental representation of $SU(3)$. Therefore exotic color representations must be decomposed into a fundamental representation basis. We do this now below for both the resonant production and pair production of the sextet diquarks.

Resonant Production

The process of diquark production in a resonant way, followed by decay into two coloured particles is shown in Fig. 4.2. We may decompose the colour of this process

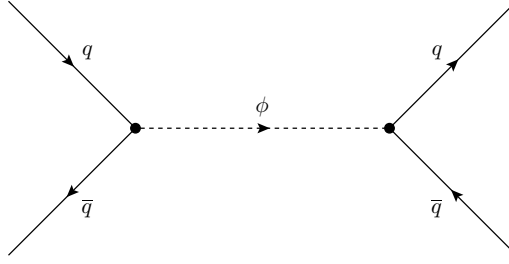


Figure 4.2: Resonant production and decay of a diquark



Figure 4.3: Unique colour flows associated with the resonant production of a diquark.

using the Clebsch-Gordan coefficients by writing our resonant production matrix element as

$$\mathcal{M}_0 = K_{ab}^i \bar{K}_i^{cd} \mathcal{A}, \quad (4.1.7)$$

where \mathcal{A} is the colour-stripped amplitude. We now make use of the completeness relation

$$K_{ab}^i \bar{K}_i^{cd} = \frac{1}{2} (\delta_a^d \delta_b^c + \delta_a^c \delta_b^d), \quad (4.1.8)$$

to read off the colour flow in the fundamental representation for the resonant production mechanism.

Following this decomposition, there are two unique colour flows associated with this process as shown in Fig. 4.3. The colour factor associated with these colour flows is $\frac{N_C(N_C+1)}{2}$.

Pair Production

The main diagrams contributing to the pair production of diquarks are shown in Fig. 4.4. We do not include the quark initiated process here, as the gluon initiated process dominates at the LHC. Each of these diagrams is decomposed into a colour

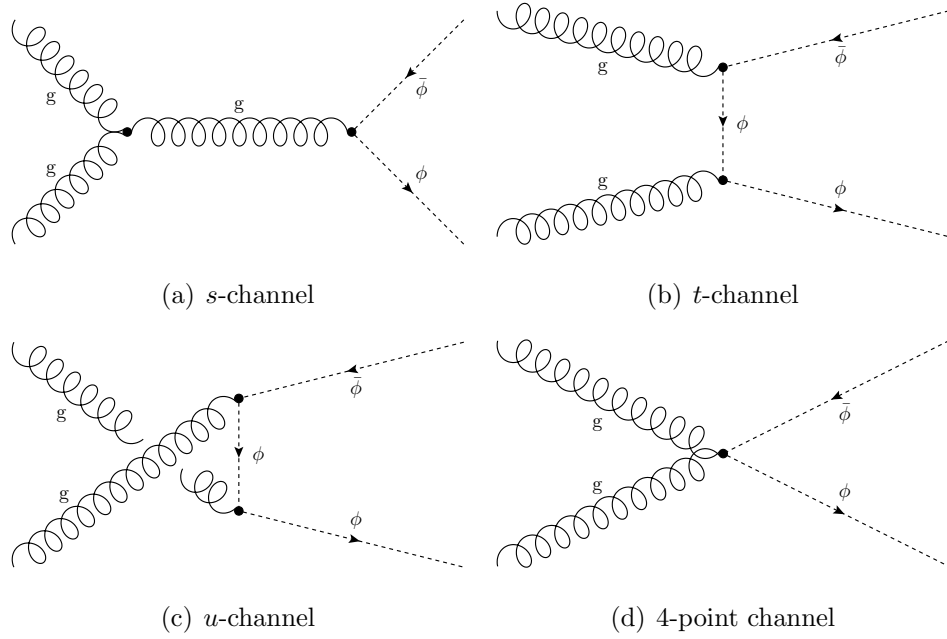


Figure 4.4: The four diagrams contributing to the pair production of a diquark.

factor and colourless component like for resonant production. By taking the colour factors for the diagrams, adding and squaring, a table of colour factors can be produced for each term in the total matrix element squared.

The s, t and u -channel go through in the way as above, making use of the fact that the generators T^A in the diquark representation may be written as

$$T_j^{Ai} = 2\text{Tr} (K^i t^A \bar{K}_j) , \quad (4.1.9)$$

where t^A is in the fundamental representation, and that the s -channel is decomposed into a t -channel like colour flow and u -channel like colour flow. The only difficulty remains in finding the colour flow for the four-point interaction. Using the Feynman rules for two gauge bosons and two scalar-quarks in Ref. [150], we find that

$$\mathcal{M}_0 = \left(\frac{1}{3} \delta^{AB} + d^{ABC} T^C \right) K_{ab}^j \bar{K}_i^{dc} , \quad (4.1.10)$$

and now we make use of the relation [18]

$$\{T^A, T^B\} = \frac{1}{N} \delta^{AB} + d^{ABC} T^C . \quad (4.1.11)$$

These results can now be used to decompose the four-point interaction's colour flows into the (anti)fundamental representation. We find that the pair production process

Diagram	(a)	(b)	(c)	(d)	(e)	(f)	(g)	(h)	(i)	(j)	(k)	(l)
(a)†	c_1	c_2	c_2	0	c_2	c_3	0	c_6	c_6	0	0	c_2
(b)†	c_2	c_1	0	c_2	c_3	c_2	c_6	0	0	c_6	c_2	0
(c)†	c_2	0	c_1	c_2	0	c_6	c_2	c_3	c_5	c_5	c_5	c_3
(d)†	0	c_2	c_2	c_1	c_6	0	c_3	c_4	c_6	c_5	c_3	c_6
(e)†	c_2	c_5	0	c_6	c_1	c_1	c_2	0	0	c_2	c_6	0
(f)†	c_3	c_2	c_6	0	c_1	c_1	0	c_2	c_2	0	0	c_6
(g)†	0	c_6	c_4	c_3	c_2	0	c_1	c_2	c_6	c_3	c_5	c_6
(h)†	c_6	0	c_3	c_4	0	c_2	c_2	c_1	c_3	c_6	c_6	c_5
(i)†	c_6	0	c_5	c_6	0	c_2	c_6	c_3	c_1	c_2	c_2	c_3
(j)†	0	c_6	c_5	c_5	c_2	0	c_3	c_6	c_2	c_1	c_3	c_2
(k)†	0	c_2	c_5	c_3	c_6	0	c_5	c_6	c_2	c_3	c_1	c_2
(l)†	c_2	0	c_3	c_6	0	c_6	c_6	c_5	c_3	c_2	c_2	c_1

has twelve unique colour flows, as shown in Fig. 4.5. We include the colours in Fig. 4.5 as a visual aid, they have no physical meaning. From these colour flows, Table 4.1.2 is produced, where $c_1 = \frac{(N_C^2-1)^2}{16}$, $c_2 = \frac{(N_C^2-1)^2}{16N_C}$, $c_3 = \frac{(N_C^2-1)}{16}$, $c_4 = \frac{(N_C^2-1)}{16N_C}$, $c_5 = \frac{-(N_C^2-1)}{16}$ and $c_6 = \frac{-(N_C^2-1)}{16N_C}$.

Shower

The splitting functions were decomposed in the same way as for the pair production, and by making use of the fact that

$$T_m^{Ak} = \delta_k^i T_j^{Ai} \delta_m^j = \text{Tr}(K^k \bar{K}_i) T_j^{Ai} \text{Tr}(K^j \bar{K}_m), \quad (4.1.12)$$

and from earlier that $\delta_j^i = \text{Tr}(K^i \bar{K}_j)$. Then we split the traces, such that we are left with

$$\bar{K}_i^{ab} T_j^{Ai} K_{cd}^j, \quad (4.1.13)$$

and using the above, we decompose the splitting functions into four unique colour flows associated with a diquark emitting a gluon, as shown in Fig. 4.6, again where the colours are included as a visual aid.

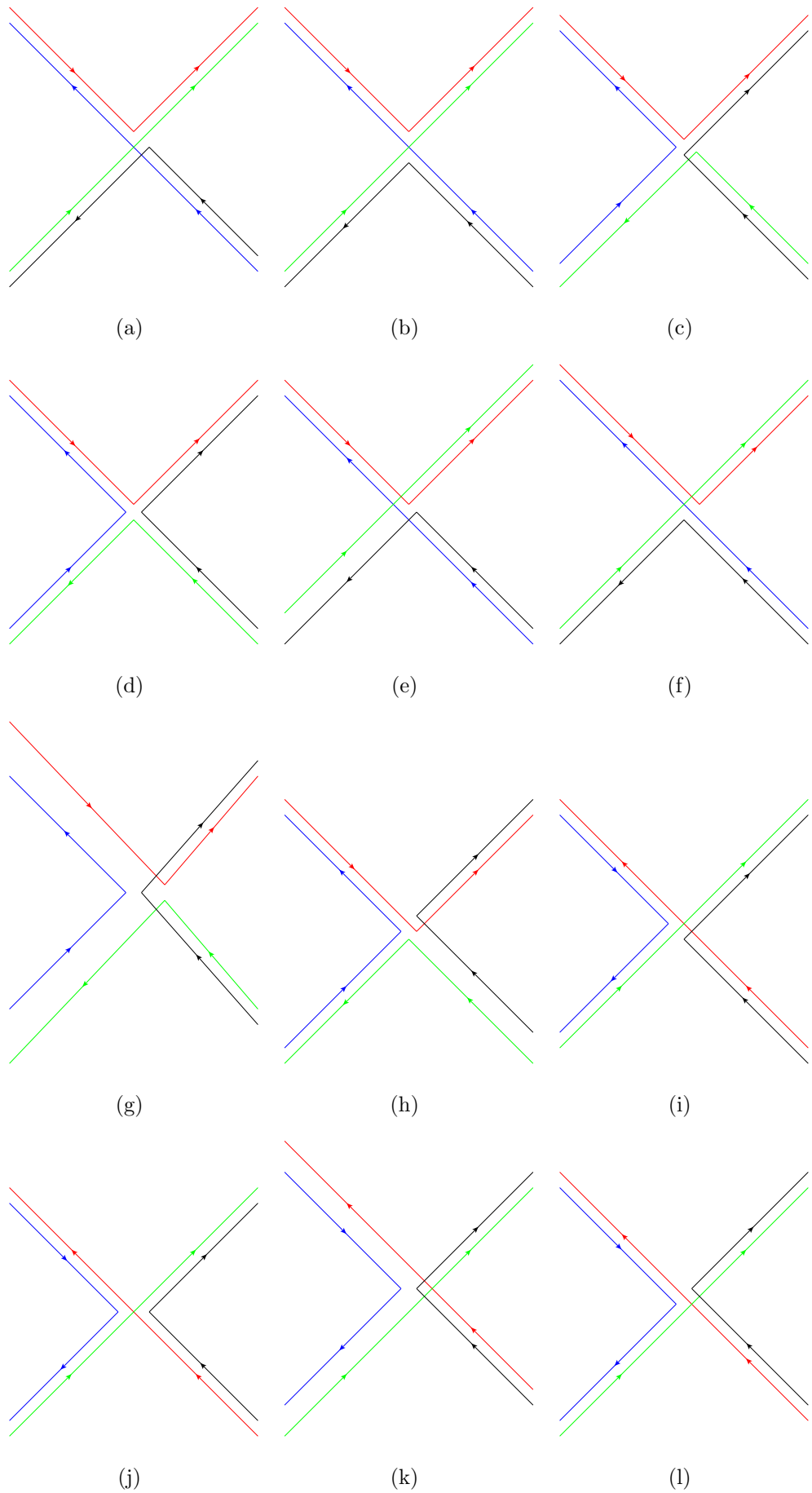


Figure 4.5: Unique colour flows associated with the pair production of diquarks.

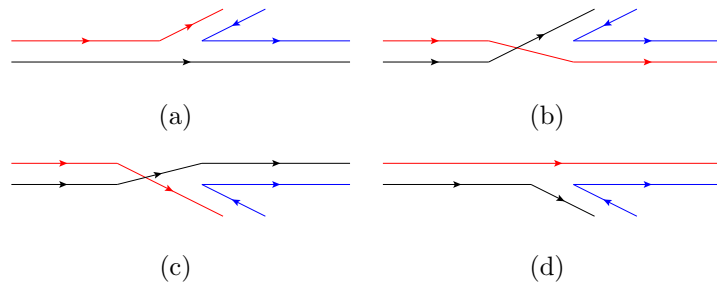


Figure 4.6: Colour flows for a diquark emitting a gluon during the shower.

Only the colour prefactor of the existing splitting functions is changed. The colour prefactor is given by $\frac{10}{3}$, *i.e.* the diquarks radiate $2\frac{1}{2}$ times more than a particle in the octet representation. In simulating diquarks during the shower, we assumed that gluons did not branch to form diquarks owing to the large diquark mass.

4.2 Phenomenology

In order to study the phenomenology simulations were performed for the scalar $\Phi_{1,4/3}$ and the vector $V_{2,5/6}^{\mu+}$ diquarks which were chosen as they can be produced as s -channel resonances from the partonic collision of the valence up quarks. In all our analyses, jets were clustered using the anti- k_T algorithm [151], as implemented in the `FastJet` package [106], using a radius parameter of $R = 0.6$. This choice is typical for the ATLAS experiment at the LHC [3]. The LO** PDFs of Ref. [152], which are the default choice in `Herwig++`, were used.

There are phenomenological constraints on the diquark couplings from $D^0 - \bar{D}^0$ mixing and non-strange pion decays [142]. For the up-type quarks there are constraints that require

$$g_R^{uu} \lesssim 0.1 \quad \text{and} \quad g_R^{cc} \sim 0. \quad (4.2.14)$$

The g_L couplings have to be constrained due to minimal flavour violation as the left-handed CKM matrix is well known [138].

It was therefore decided to take the couplings

$$g_{R/L}^{11} = 0.1 \quad \text{and} \quad g_{R/L}^{22} = g_{R/L}^{33} = 0, \quad (4.2.15)$$

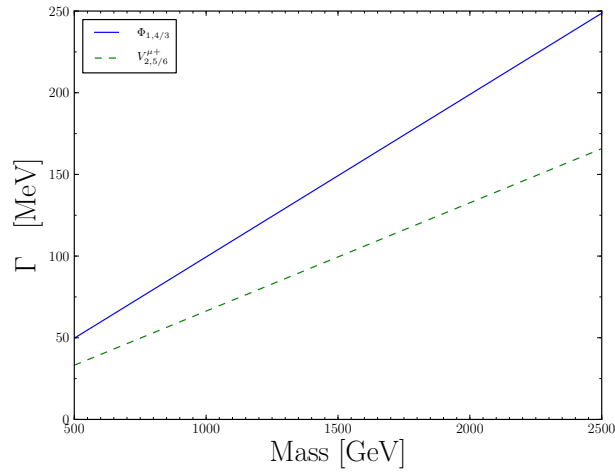


Figure 4.7: The diquark width as a function of the diquark mass for a coupling as quoted in the text for scalar and vector diquarks. The diquark coupling to quarks has been taken to be 0.1.

where the numbered indices refer to the generation.

The value of the coupling will affect any studies involving jets as the width of the particle varies as a function of the couplings.¹ If the coupling is less than the value chosen above, any peak maybe enhanced compared to what is presented in the following sections. The width as a function of the diquark mass is shown in Fig. 4.7. We note that as the width is very small the diquark potentially hadronizes before it decays.

4.2.1 Resonance Production

Firstly we look at the resonant production of sextet diquarks. If the diquark has an appropriate mass and coupling it may be resonantly produced at the LHC. The resonance production and subsequent decay of a general diquark (scalar or vector) is shown in Fig. 4.2, where the decay of the diquark will depend on its mass and unknown couplings to the quarks, g .

Fig. 4.8 shows the cross section for the production of scalar and vector diquarks

¹In fact, if the width is small then the diquark may hadronize before it decays.

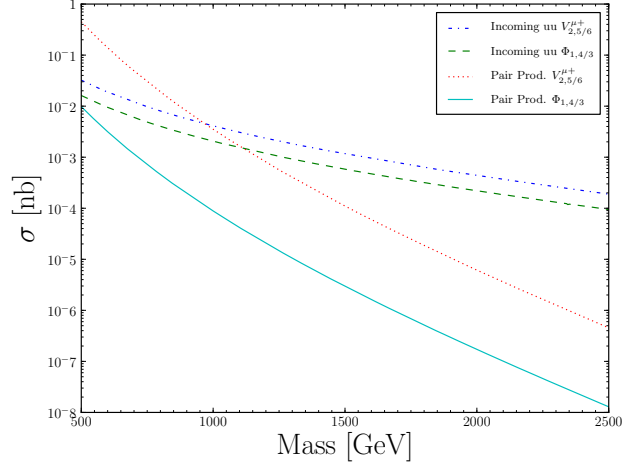


Figure 4.8: Cross section for the production of vector and scalar diquarks as a function of the diquark mass for both resonant production, from incoming uu states, and diquark pair production at $\sqrt{s} = 14$ TeV. The diquark coupling to quarks has been taken to be 0.1.

from incoming uu quarks (resonant production) and for incoming gluons (pair production). The resonant production cross section depends quadratically on the unknown diquark coupling to quarks, which as been assumed to be 0.1 in this plot, whereas the pair production cross section is independent of this coupling.

The diquark will decay into two quarks giving rise to at least two jets. The search for the production of a diquark via resonant production should therefore be in the dijet invariant mass spectrum, where a smeared peak is expected around the diquark mass. The primary background to this search channel is QCD $2 \rightarrow 2$ scattering processes.

The signal and background were simulated using **Herwig++**. The analysis and modelling of the backgrounds followed that suggested in Ref. [3]. The transverse momenta and pseudorapidities of the jets were required to be $p_T^1 > 150$ GeV, $p_T^2 > 60$ GeV and $|\eta_{1,2}| < 2.5$ where 1 is the hardest jet and 2 is the subleading jet. In addition we required that the dijet invariant mass, m_{jj} satisfied $m_{jj} > 300$ GeV and the rapidity difference between the leading and subleading jet was $|\Delta\eta_{12}| < 1.3$. The dijet invariant mass spectrum after these cuts is shown in

Figs 4.9 and 4.10 for $\sqrt{s} = 7$ and 14 TeV, respectively. The diquarks were simulated at masses of 500 GeV, 800 GeV, 1200 GeV, 1600 GeV and 2000 GeV.

As simulating the QCD m_{jj} spectrum at high masses is difficult, a functional form

$$f(x) = a_0(1 - x)x^{(a_1 + a_2 \ln x)}, \quad (4.2.16)$$

was fitted to the low masses, where the a_i are fitted parameters and $x = m_{jj}/\sqrt{s}$, and extrapolated out into the high mass region.

The results of Ref. [3] can be used to impose constraints on the diquark coupling as a function of the diquark mass. The event selection from Ref. [3] was used to reproduce the correct acceptance. This requires that the event contains at least two jets with $p_T > 150$ GeV and a subleading jet with $p_T > 30$ GeV. Both the leading and subleading p_T jets must satisfy $|\eta_j| < 2.5$ with $\Delta\eta_{12} < 1.3$ and $m_{jj} > 150$ GeV.

The signal, after the cuts, was fitted to a Gaussian distribution, with the mean fixed, m , at the simulated diquark mass to obtain the standard deviation of the distribution, σ , so that the results presented in Ref. [3] could be used to obtain the limits on the diquark coupling.

A standard Gaussian was chosen as it is practically easy to implement and after experimenting with a skewed Gaussian was found to give comparable results. The Gaussian was fitted using the usual process of minimising χ^2 with the Python implementation of the popular Minuit package [153].

As suggested in [3], long tails were removed by taking a window around the diquark mass of $\pm 20\%$ for the fit. If the σ/m value obtained was below the range of that given in the paper, then the number of events associated with the lowest σ/m for that mass was used. This allows a conservative estimate for the excluded coupling, as opposed to one which may be obtained by extrapolation into the unknown region. The limit on the diquark coupling is shown in Fig. 4.11 where because the statistical errors were negligible, the bands shown come from varying the scale from 50% to 200% of the default scale choice, *i.e.* the diquark mass.

Following the work of Ref. [3] the ATLAS collaboration has released an updated analysis [4], including additional data corresponding to an integrated luminosity of 163 pb⁻¹. This analysis included slightly harder cuts requiring $p_T > 180$ GeV and

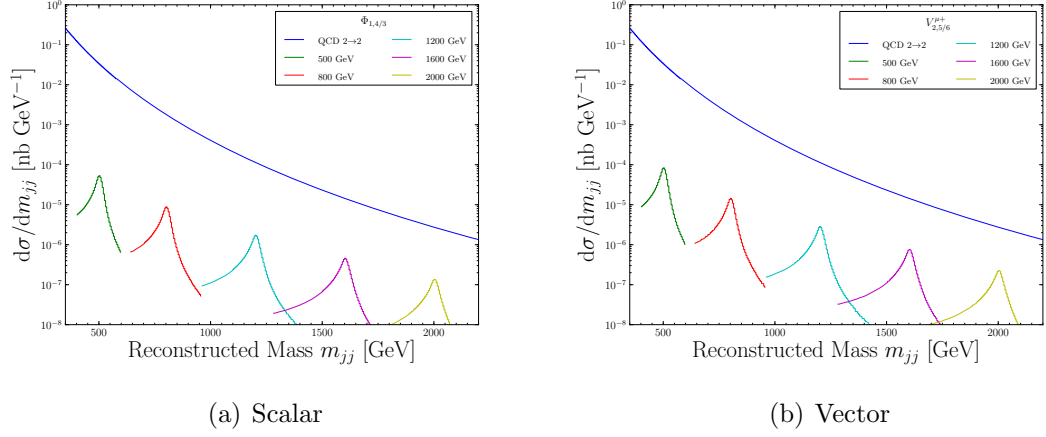


Figure 4.9: The dijet mass spectrum at $\sqrt{s} = 7 \text{ TeV}$ for 500 GeV, 800 GeV, 1200 GeV, 1600 GeV and 2000 GeV diquark masses with the couplings given in the text.

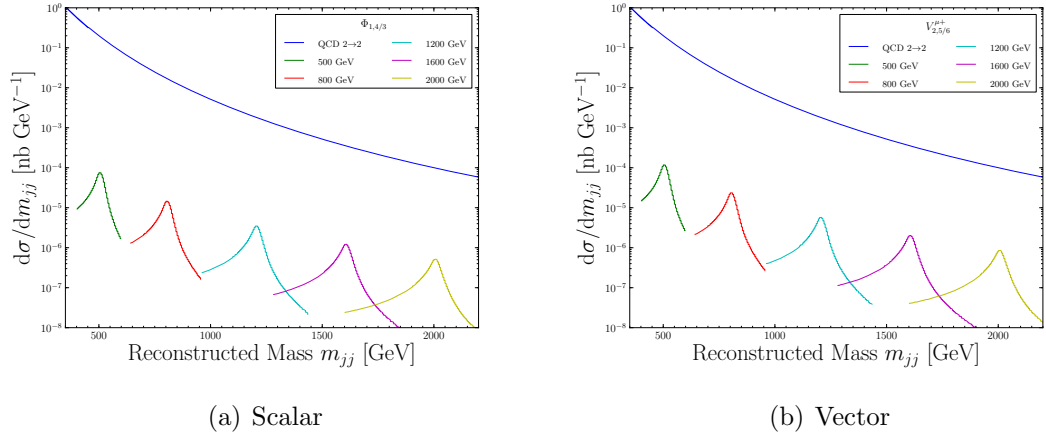


Figure 4.10: The dijet mass spectrum at $\sqrt{s} = 14 \text{ TeV}$ for 500 GeV, 800 GeV, 1200 GeV, 1600 GeV and 2000 GeV diquark masses with the couplings given in the text.

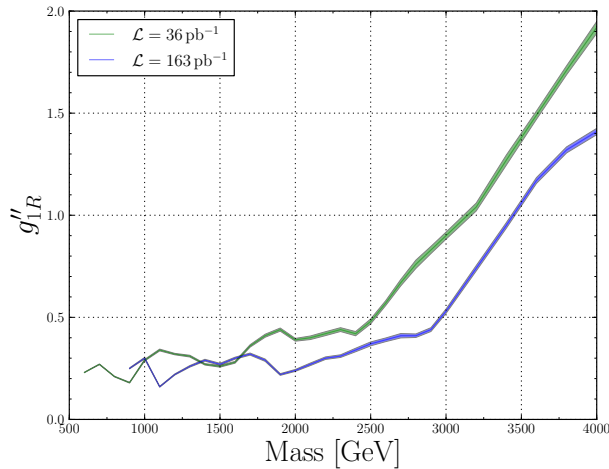


Figure 4.11: Limit on the coupling as a function of the diquark mass based on the model independent data given in the recent ATLAS publications [3, 4]. The band reflects the uncertainty from varying the scale between 50% and 200% of the diquark mass.

$m_{jj} > 170$ GeV in addition to the cuts used in Ref. [3]. The limit obtained from this higher integrated luminosity analysis is also shown in Fig. 4.11. We note that ATLAS performed better than the expected median limit in the Ref. [3] and worse than the expected median limit in [4] in the 1400 – 1600 GeV mass range, giving rise to the overlap in Fig. 4.11.

4.2.2 Pair Production

The pair production of diquarks (scalar and vector) occurs via the Feynman diagrams shown in Fig. 4.4 and also via a quark-quark initiated process with an s -channel gluon. At the LHC we expect the gluon-gluon initial state to be dominant over the quark-quark initial state and so we choose to only study the incoming gluon case here. The pair production process has one main advantage over the resonant production, it does not depend on the unknown diquark coupling. Instead, the pair production cross section depends only on the $SU(3)_C$ representation, mass and spin of the particle. The pair production process therefore has the potential to distinguish between whether a particle in the antitriplet or sextet representation was

produced due to the dependency of the cross section on the colour representation.

To date there have been no studies of the experimental signals of diquark pair production. The cross section has been calculated [140, 146, 147] and some work towards a jet study, no Monte Carlo study has been performed.

The pair production and subsequent decay of diquarks is expected to give four jets, with two pairs of jets forming systems with the mass of the diquark. The backgrounds to the pair production of diquarks are:

- vector boson WW , ZZ and ZW pair production;
- vector boson, W and Z , production in association with additional jets;
- top quark pair, $t\bar{t}$, production;
- QCD jet production.

The analysis proceeded by placing cuts on the four hardest jets: $p_T^1 > 150$ GeV, $p_T^2 > 100$ GeV, $p_T^3 > 60$ GeV and $p_T^4 > 30$ GeV, where the four jets $i = 1, 4$ are ordered in p_T such that the first jet is the hardest. All four jets were required to have pseudorapidity $|\eta_i| < 3$. Two pairs of jets were then formed with the pairing selected that minimized the mass difference between the two pairs of jets. If, after pairing, the two hardest jets are in the same pair of jets, the event was vetoed. The mass difference between the pairs was required to be less than 20 GeV.

The signal and backgrounds were simulated for the production of the $\Phi_{1,1/3}$ and $V_{2,5/6}^{\mu+}$ diquarks giving the results shown in Fig.s 4.12 and 4.13 for $\sqrt{s} = 7$ and 14 TeV, respectively. As the backgrounds are dominated by QCD scattering, *i.e.* the contribution of the QCD scattering processes is approximately one hundred times that of all the other backgrounds combined, only the sum of the backgrounds is shown. As for the resonant production, the plots show the production of diquarks with masses of 500 GeV, 800 GeV and 1200 GeV, 1600 GeV and 2000 GeV. The low mass QCD background was fitted with Eqn. 4.2.16 and extended out into the high mass region.

A window of ± 50 GeV was taken around the diquark mass and the $\frac{S}{\sqrt{B}}$ was calculated for a number of luminosities the results of which are shown in Fig. 4.14. We

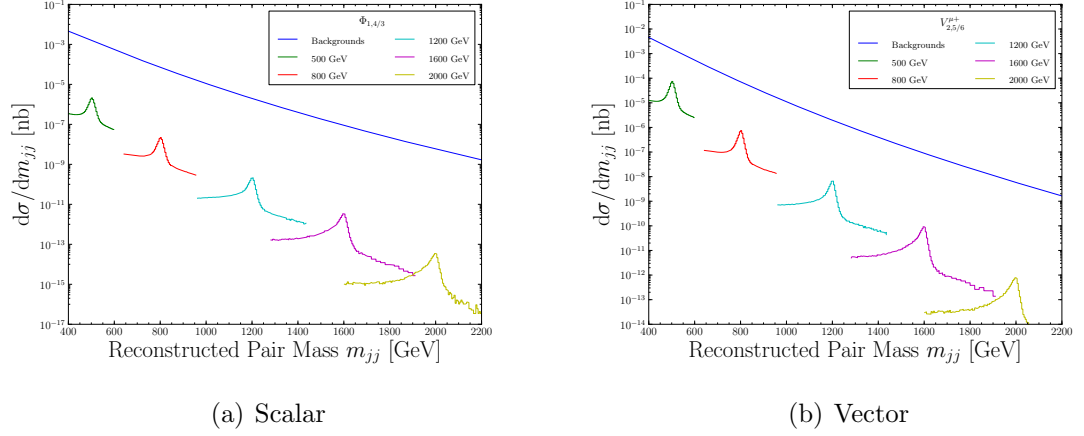


Figure 4.12: The mass spectrum of dijet pairs in four jet events at $\sqrt{s} = 7$ TeV for 500 GeV, 800 GeV, 1200 GeV, 1600 GeV and 2000 GeV diquark masses.

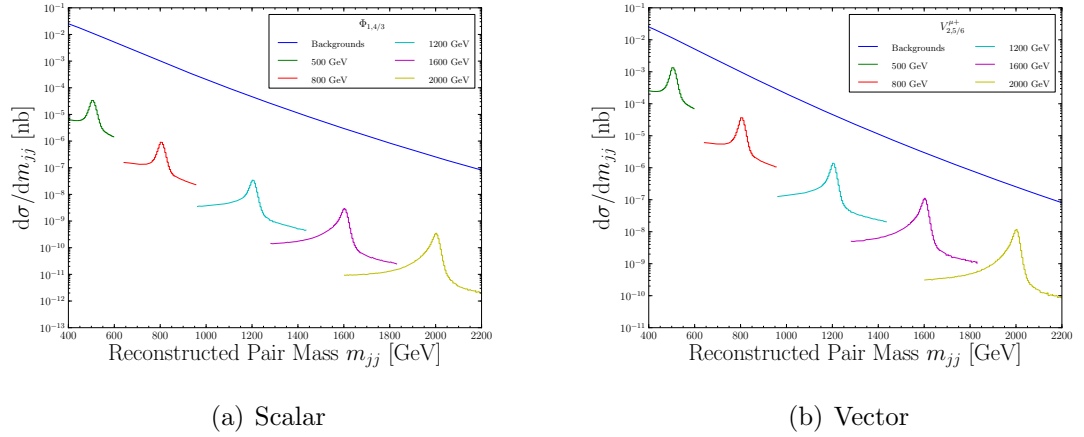


Figure 4.13: The mass spectrum of dijet pairs in four jet events at $\sqrt{s} = 14$ TeV for 500 GeV, 800 GeV, 1200 GeV, 1600 GeV and 2000 GeV diquark masses.

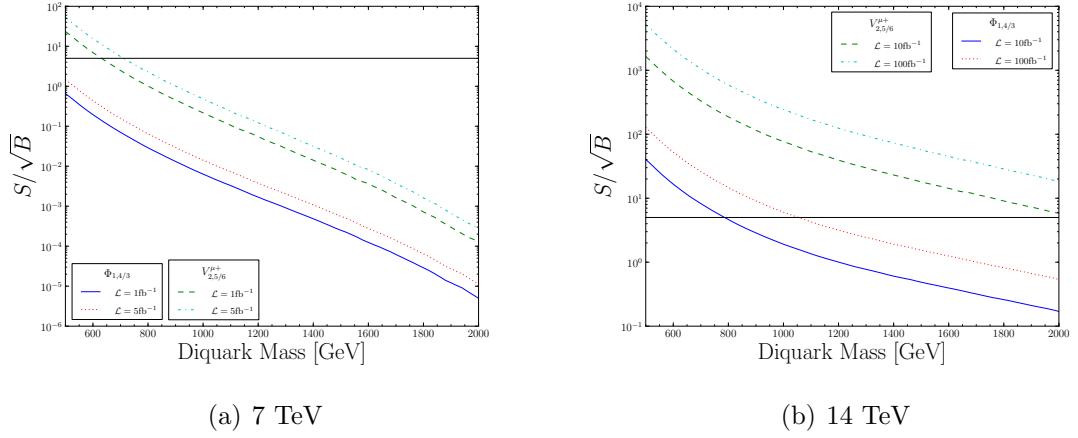


Figure 4.14: $\frac{S}{\sqrt{B}}$ for the scalar and vector diquark at luminosities of $\mathcal{L} = 1\text{fb}^{-1}$ and $\mathcal{L} = 5\text{fb}^{-1}$ at $\sqrt{s} = 7\text{TeV}$ and $\mathcal{L} = 10\text{fb}^{-1}$ and $\mathcal{L} = 100\text{fb}^{-1}$ at $\sqrt{s} = 14\text{TeV}$. The black horizontal line shows $\frac{S}{\sqrt{B}} = 5$.

see that the vector diquark manifests itself more prominently than the scalar, which is consistent with the increased cross section of the vector in the pair production process as seen in Fig. 4.8. It will be hard to observe a scalar diquark using the pair production process at $\sqrt{s} = 7\text{TeV}$ while with $\mathcal{L} = 5\text{fb}^{-1}$ it should be possible to observe a vector diquark with mass less than 700 GeV.

There is a marked increase in discovery potential at the increased energy and luminosities running at $\sqrt{s} = 14\text{TeV}$ brings. A vector diquark in the mass range presented here ($< 2000\text{GeV}$) should be seen with $\mathcal{L} = 10\text{fb}^{-1}$, whereas even with $\mathcal{L} = 100\text{fb}^{-1}$ only a low mass ($\lesssim 1050\text{GeV}$) scalar diquark has potential for discovery.

4.3 Conclusions

In this chapter we have presented a method for simulating the production and decay of particles in the sextet colour representation which has been implemented in Herwig++.

We simulated the production and decay of vector and scalar sextet diquarks at energies relevant to the LHC. Based on the findings and the latest ATLAS search for

new particles in two-jet final states, new constraints have been put on the couplings of the diquarks to SM particles. Unfortunately we see from the large backgrounds that discovery in the dijet channel will be very difficult at the LHC.

We have also presented studies of the gluon-gluon initiated pair production mechanism, which is independent of the unknown coupling of the sextet diquark to quarks. The quark-quark initiated pair production mechanism has not been studied, as at low masses we expect the gluon-gluon initiated pair production process to dominate. This process has a promising search reach with the possibility of observing vector diquarks with masses less than 710 GeV at $\sqrt{s} = 7$ TeV and both vector, for masses less than 2 TeV, and scalar, for masses less than 1 TeV, with the LHC running at design energy.

We have seen that the potential to discover the diquark is also very limited at the LHC in the pair production mechanism owing to its small rate and again large backgrounds. However, It could still be possible to observe the diquark via its coupling to top quarks and in the future it may be prudent to conduct an analysis focusing on the process where the pair produced diquarks decays to two top quarks.

Using the decay of a diquark to two top quarks allows us to distinguish the diquark from other SUSY particles as we can fully reconstruct the final state by the four jets produced, compared to most SUSY processes where an experimentally ‘invisible’ particle *e.g.* neutralino is involved in the process. A fully reconstructed state also allows us to measure the spin properties of the particle produced and distinguish whether a scalar or vector diquark was produced.

Furthermore, other improved analyses may be able to uncover a signature of a diquark in these large backgrounds. The tool provided here can now be used by other interested parties in this area to perform such analyses and also be used with a full detector simulator by experimentalists searching for diquarks.

Further Monte Carlo studies of diquark production in this area in the future could prove to be beneficial in the search for new Physics.

Chapter 5

Conclusions

In this thesis we have examined the principles behind a Monte Carlo event generator and outlined the Physics and its implementation in the **Herwig++** Monte Carlo event generator.

The improvement of the accuracy of simulation has been stressed throughout and examples of two improvements with a subsequent study of the phenomenology has been shown for the highly relevant boosted Higgs boson studies, to examine the Higgs boson decaying to two bottom quarks at the LHC. Although currently not used as a discovery channel, the verification of existing results and extension of the accuracy of simulation will prove fruitful if we are to use this method to study the decay of a light Higgs boson at the LHC. This is especially relevant with the discovery of new boson of mass 125 GeV. Studying this new boson to see if it has the expected couplings to bottom quarks will be important so we can ascertain whether this is the Standard Model Higgs boson we are expecting.

With regards to the technique itself, we have found that the use of jet substructure has promise to study the Higgs boson in this challenging decay mode, and warrants further study at the LHC. The series of error tunes provided will also enable experimentalists and theorists alike to produce a more robust error associated with the tuning of a Monte Carlo event generator, whilst obviously still taking into consideration statistical errors.

As mentioned, one area of further study in this region should focus around understanding to $g \rightarrow b\bar{b}$ splitting as implemented in a Monte Carlo even generator.

Accurately simulating this splitting is important for the backgrounds to jet substructure techniques that rely on the decay of heavy objects to bottom quarks. Also, such studies are sensitive to the underlying event and more detailed studies on how underlying event effects jet substructure would be of use.

Following on from the jet substructure investigation, we also outlined the systematic improvement of simulation of top quark radiation, owing to its width. We have shown that the leading colour approximation employed by a Monte Carlo event generator is actually a good approximation and that current event generators can be thought to be giving an accurate simulation of the radiation. A new algorithm as implemented in the Monte Carlo event generator **Herwig++** is shown based on calculated radiation patterns up to the emission of two gluons and a study of the phenomenology outlined.

Although the effect seen on the top quark mass analyses presented was small, other observables may be more sensitive to these effects and so including them in our simulation could become important, especially for SUSY style processes where there is more than one heavy particle in a decay cascade. Single top production as being investigated at the LHC as a probe of the Electroweak sector may also be sensitive to these effects and so further study in this area in the future would be relevant.

We have also discussed the simulation of new Physics and that without an accurate simulation the goal of finding such new Physics at a modern collider experiment such as the LHC would be very challenging. The Sextet diquark model was outlined along with its implementation in the Monte Carlo event generator **Herwig++** and again, an associated phenomenological study. Limits were placed on the diquark coupling and the potential of discovery of such an object discussed.

The dijet channel, and also pair production channel, all have large backgrounds and so potential for discovery of a diquark is limited at the LHC. An investigation of the diquark coupling to top quarks could lead to a potential discovery though. If the diquark decays to two top quarks then there is a chance to create a fully reconstructed final state. This is beneficial compared to the decays of many SUSY particles which have an experimentally ‘invisible’ object in their final state *e.g.*

neutralino. The fully reconstructed final state could allow us also to measure the spin properties of any produced diquark and determine whether a scalar or vector diquark has been produced.

Clearly as the modern collider experiments increase in energy and their final states become more complex, improving all aspects of simulation will remain an important task in the future. We have shown that we can have a good degree of confidence in our existing tools, however, improving the accuracy of simulation should still continue. This thesis has been written at exciting time in Particle Physics and hopefully many more discoveries are still to come. The work undertaken here has contributed towards the current round of experiments and their work in unlocking the secrets of Nature.

Appendix A

Monte Carlo Integration

Often we wish to evaluate complex integrals numerically, as they cannot be done analytically. There are a number of ways to achieve this. The simplest example is the Newton-Cotes method. Assuming we want to evaluate the integral

$$I_{ab} = \int_a^b f(x) \quad (\text{A.0.1})$$

we approximate the integral by splitting our region up into rectangular segments and summing over them

$$I_{ab} \approx \sum_{i=0}^{n-1} f(x_i) \Delta x \quad (\text{A.0.2})$$

where $\Delta x = \frac{(b-a)}{n}$ and $x_i = a + i\Delta x$. We define the error by

$$\int_a^b f(x) - \sum_{i=0}^{n-1} f(x_i) \Delta x, \quad (\text{A.0.3})$$

where the error in this method goes like $\frac{1}{n}$. We can go better, by instead of approximating the area under our function $f(x)$ as a series of trapezoids

$$I_{ab} \approx \sum_{i=0}^{n-1} (f(x_{i+1}) + f(x_i)) \frac{\Delta x}{2} \quad (\text{A.0.4})$$

where now the error goes like $\frac{1}{n^2}$ [154]. Or we can even go one better and use an interpolated parabola, called Simpson's rule, where the error goes like $\frac{1}{n^4}$ [154]. Another alternative way relies on the mean value theorem of calculus

$$I_{ab} = (b - a) f(c) \quad (\text{A.0.5})$$

where $f(c)$ is the mean value of the function over the region. Using this method we can define a Monte Carlo integration by sampling the function $f(x)$ in the region $[a, b]$ *i.e.*

$$I_{ab} = \int_a^b f(x) = (b-a) f(c) \approx (b-a) \frac{1}{n} \sum_{i=0}^{n-1} f(x_i) . \quad (\text{A.0.6})$$

The law of large numbers states that the approximation becomes exact in the asymptotic limit, and so

$$\begin{aligned} \mathbb{E}[f(x)] &= \lim_{n \rightarrow \infty} \frac{1}{n} \sum_{i=0}^{n-1} f(x_i) \\ &\approx \frac{1}{n} \sum_{i=0}^{n-1} f(x_i) . \end{aligned} \quad (\text{A.0.7})$$

An appreciation of the error is developed by computing

$$\begin{aligned} \epsilon^2 &= \left(\frac{1}{n} \sum_{i=0}^{n-1} f(x_i) - \mathbb{E}[f(x)] \right)^2 \\ &= \frac{\text{Var}[f(x)]}{n} \left(\left[\frac{\sum_{i=0}^{n-1} f(x_i) - n\mathbb{E}[f(x)]}{\sqrt{n}\sqrt{\text{Var}[f(x)]}} \right] \right)^2 \\ \Rightarrow \epsilon &= \frac{\sigma[f(x)]}{\sqrt{n}} \mathcal{N}(0, 1) \end{aligned} \quad (\text{A.0.8})$$

where $\mathcal{N}(0, 1)$ is a normally distributed random number of mean 0 and standard deviation 1, $\sigma^2[X] = \text{Var}(X)$ is the variance of X and the second to third line holds from the Central Limit Theorem. So we see this way of evaluating the integral converges like $1/\sqrt{n}$. Whilst this is slower in low numbers of dimensions when compared to the other rules above, the real key is that the rate of convergence is always $1/\sqrt{n}$, no matter what the dimension, where as for the trapezoid rule, the error goes like $\mathcal{O}(n^{-2/d})$ or for Simpson's rule $\mathcal{O}(n^{-4/d})$ [154] with the error bound becoming less useful as the dimension increases. To reduce our error with a Monte Carlo integral then, all we need do is generate more points and our error is guaranteed to decrease like $1/\sqrt{n}$.

In fact, more tricks can be applied to the integration to reduce the variance. If we decide to sample the integration region in areas where $f(x)$ is larger, compared to when it is smaller, we can lower the variance. Mathematically speaking we write

$$I = \int f(x) dx = \int \frac{f(x)}{g(x)} g(x) dx = \mathbb{E}_g \left[\frac{f(x)}{g(x)} \right] , \quad (\text{A.0.9})$$

which we achieve by sampling the points in our distribution according to $g(x)$ and then evaluating $\frac{f(x)}{g(x)}$. If we are clever, and choose $g(x)$ such that it smoothly follows $f(x)$, then we can reduce the variance and associated error of our integral. These techniques become more important than just generating more points to decrease $1/\sqrt{n}$.

The question then remains as to how to generate our points according to $g(x)$. If we are lucky and we can invert our integrated function $G(x)$, and assuming $g(x)$ is defined and wanted for $x \in [-\infty, +\infty]$, then from cumulative probability function

$$G(x) = \int_{-\infty}^x g(y) dy = \mathcal{R}, \quad (\text{A.0.10})$$

with the random number $\mathcal{R} \sim \text{Unif}[0, 1]$ then clearly

$$x = G^{-1}(\mathcal{R}). \quad (\text{A.0.11})$$

This is practically never the case, however, and we must use a different method for generating according to a distribution. One such method is John von Neumann's¹ hit or miss method. We build a simple, invertible over-estimator $h(x)$ of our function $g(x)$ across the region of interest such that

$$h(x) \geq \max[g(x)]. \quad (\text{A.0.12})$$

We then generate points according to $h(x)$ and accept the point according to the probability $\frac{g(x)}{h(x)}$, by comparing to another random number, which then distributes points correctly and according to $g(x)$. This can be seen as the first point is picked according to $h(x)dx$ and then retained according to $\frac{g(x)}{h(x)}$ and when these two are multiplied together, we recover the original distribution we wanted, $g(x)$.

If the function in questions varies a lot between intervals, we can sub-divide the function into the required intervals by defining $g(x) = \sum_i g_i(x)$ and applying these methods to each of the regions i . This is called stratified sampling.

An example of importance sampling method can be seen with the integral of $f(x) = \sin\left(\frac{\pi x}{2}\right)$, using $g(x) = 2x - x^2$, where x was sampled according to $g(x)$ by

¹John von Neumann is considered by many to be the father of Monte Carlo techniques, which were pioneered during the efforts at the Los Alamos laboratory and development of the nuclear bomb during the World War II Manhattan Project.

Sampling	Result	Error
Uniform	0.637	$0.308/\sqrt{N}$
Importance	0.636	$0.033/\sqrt{N}$

Table A.1: A comparison of the uniform sampling method and the importance sampling method for the integration of the function $f(x) = \sin\left(\frac{\pi x}{2}\right)$, $N = 10^3$.

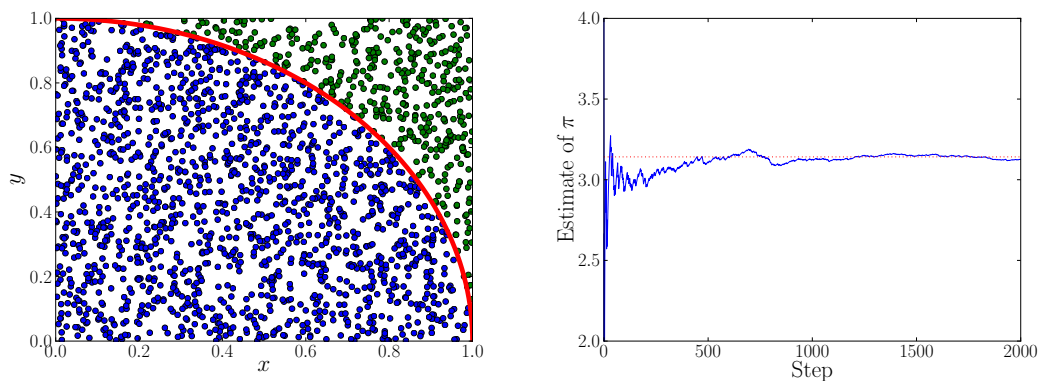


Figure A.1: The evaluation of π using the hit or miss method.

using the hit or miss method, with our over-estimator $h(x) = 1$. Table A.1 shows a comparison between the standard uniform and the importance sampling method.

The hit or miss method can actually be used to directly integrate functions too. If, as above, we define an over-estimator of our function of interest and throw points down in the area bounded by this function and, in two dimensions, the x -axis then the integral of our function is given by

$$I = \int f(x) \approx \frac{N_{\text{hit}}}{N_{\text{hit}} + N_{\text{miss}}} \quad (\text{A.0.13})$$

where by N_{hit} is the number of points inside $f(x)$ and N_{miss} is between the function we're integrating, $f(x)$ and the over-estimator $h(x)$. The canonical example is estimating π by this method, using a circle bounded by a square, as seen in Fig. A.1.

Appendix B

Jets and Jet Algorithms

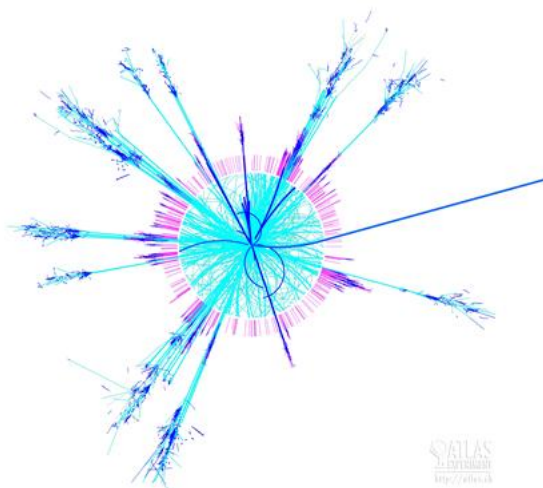


Figure B.1: The simulated production of microscopic black hole in the ATLAS detector at the LHC. Image courtesy of the CERN press office, with whom copyright remains.

Free quarks or gluons don't exist in Nature - after being produced they themselves produce a collimated spray of hadrons, known as a jet. Jets are clearly seen in events for example in Fig. B.1, but to define mathematically what a jet is in such a way that both experiment and theory can use the same definition turns out to be non-trivial. An excellent review of jet physics can be found in Ref. [5], of which we summarise some of the more important findings here.

The Snowmass accord laid out the requirements for a jet algorithm and these

are given as [5, 155, 156]:

1. *Simple to implement in an experimental analysis;*
2. *Simple to implement in theoretical calculations;*
3. *Defined at any order of perturbation theory;*
4. *Yields finite cross sections at any order of perturbation theory;*
5. *Yields a cross section that is relatively insensitive to hadronization.*

In general jet algorithms fall broadly into two categories - cone algorithms and sequential recombination algorithms. We will not look at cone algorithms here, as none have been used in this thesis and some older cone algorithms are plagued by a lack of IR safety.

A jet algorithm has to be both IR and collinear safe, and by this we mean that the addition of an extra soft or collinear parton should not change the set of hard jets that are found in the event [5]. This *has* to be the case if we are to satisfy the KLN theorem. For example, if the addition of an extra soft gluon gets combined into a different jet than the parton that produced it, then the IR cancellation between virtual and real corrections would not be complete in either jet, with implications for perturbative calculations. A diagram exposing this is shown in Fig. B.2.

One cone algorithm, **SISCone** [157], has surpassed this problem and is now both IR and collinear safe, however, the current round of experiments at the LHC are focused on sequential recombination type algorithms and it is these that we turn our attention to now.

Sequential Recombination Algorithms

Sequential recombination algorithms came out of e^+e^- experiments, with the Jade algorithm being the first [158, 159]. The Jade algorithm satisfies the requirements of being both I.R. and collinear safe, as soft particles get recombined at the beginning of the clustering. The Jade algorithm proceeds by:

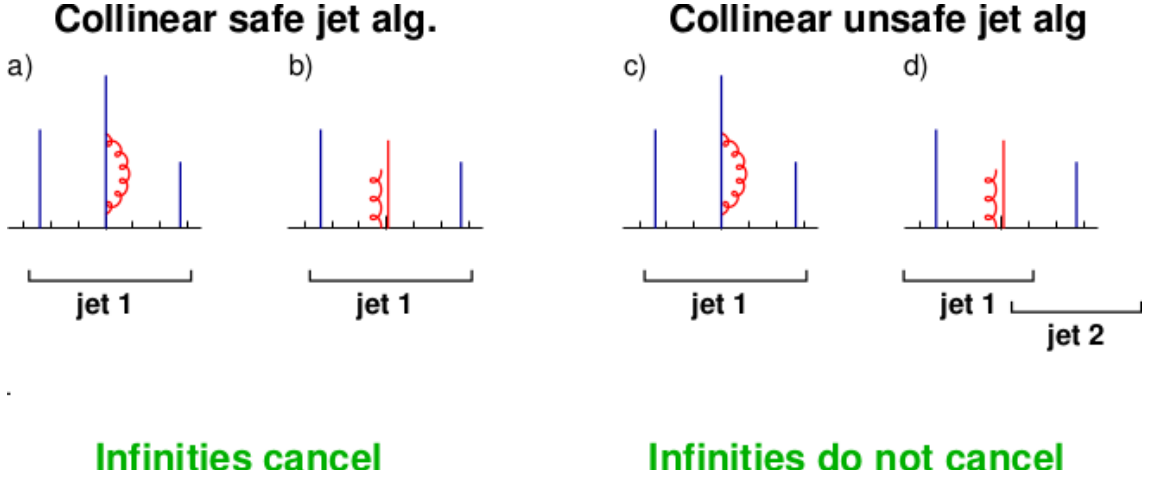


Figure B.2: An example of the cancellation of divergencies in jets, taken from Ref. [5].

1. For each pair of particles i, j calculate a distance

$$y_{ij} = \frac{2E_i E_j (1 - \cos \theta_{ij})}{Q^2} \quad (\text{B.0.1})$$

where Q is the total energy in an event. E_i is the energy of the i^{th} particle and θ_{ij} is the angle between particles i, j ;

2. Find y_{\min} of all the y_{ij} s;
3. If $y_{ij} < y_{\text{cut}}$ recombine i, j into a single particle and repeat;
4. Otherwise declare all remaining particles to be jets and exit.

Experimentally, we measure energy deposits in a calorimeter within the detector and so a particle here can be thought of as an energy deposit in an experimental detector. The Jade algorithm does have a subtlety in that two very soft particles moving backwards can be recombined into a single particle at the start of the algorithm. This is counterintuitive to jets having a constrained angular size [5].

The originally defined k_t algorithm is exactly the same as the Jade algorithm, except one now defines

$$y_{ij} = \frac{2 \min(E_i, E_j) (1 - \cos \theta_{ij})}{Q^2} \quad (\text{B.0.2})$$

as the jet measure. This has the added advantage of using the minimum energy between the two particles i, j , so that the measure between two soft back-to-back particles is greater than that between a soft particle and a hard particle close in angle.

For hadron colliders, where the total energy in a collision may not be well defined, we may use the *inclusive* k_t algorithm. The inclusive k_t algorithm does away with the parameter d_{cut} , and introduces a new parameter R . Now, compared to the original k_t algorithm, one instead defines

$$d_{ij} = \min(p_{T,i}^2, p_{T,j}^2) \frac{\Delta R_{ij}^2}{R^2}, \quad (\text{B.0.3})$$

where $\Delta R_{ij}^2 = (y_i - y_j)^2 + (\phi_i - \phi_j)^2$, there is the introduction of a beam distance

$$d_{iB} = p_{T,i}^2, \quad (\text{B.0.4})$$

which defines how far a particle is from an incoming beam and we introduce a new parameter R . The algorithm proceeds by [160]

1. For each pair of particles i, j calculate a d_{ij} and d_{iB} ;
2. Find the minimum of all the calculated d_{ij} and d_{iB} ;
3. If it is a d_{ij} recombine i, j into a single particle and repeat;
4. If it is a d_{iB} then declare i to be a jet, remove it from the set of particles and return to 1;
5. Stop when there are no particles left, and one just has jets.

For hadron-hadron collisions, we define there to be two beam particles [161]. The advantage of these variables is that they are invariant under longitudinal boosts.

Experimentalists, however, do not like this definition as it gives jagged edges to the jets and was arguably computationally slow to calculate [5]. The anti- k_t algorithm gets around the jagged edge problem, by now defining [151]

$$d_{ij} = \min\left(\frac{1}{p_{T,i}^2}, \frac{1}{p_{T,j}^2}\right) \frac{\Delta R_{ij}^2}{R^2}, \quad (\text{B.0.5})$$

and

$$d_{iB} = \frac{1}{p_{T,i}^2}, \quad (\text{B.0.6})$$

so that now the the hardest particles are favoured, compared to the softest in the k_t algorithm. The jets grow outwards from the hardest particles and produce shapes that are approximately circular.

There is yet another type of sequential recombination algorithm called the Cambridge-Aachen algorithm, or C/A for short, which is used in the jet substructure analysis of this thesis [104, 105]. This is like the k_t algorithm, but without the k_t and proceeds by recombining all jets until $d_{ij} = \Delta R_{ij} > R$. This can be thought of angular ordering in reverse.

Typically at ATLAS at the LHC, an anti- k_t algorithm is used with an R parameter of $R = 0.6$. Thankfully a package, **FastJet** [106], has been written that allows interface to a library of jet algorithms for use in Monte Carlo simulations. **FastJet** also has the advantage of being quick - achieving $\mathcal{O}(N \ln N)$ timing for the sequential recombination algorithms compared to the original implementations that took either $\mathcal{O}(N^3)$ or $\mathcal{O}(N^2)$. The **FastJet** package is readily available for download and easy to link to.

Appendix C

Triple Gluon Vertex

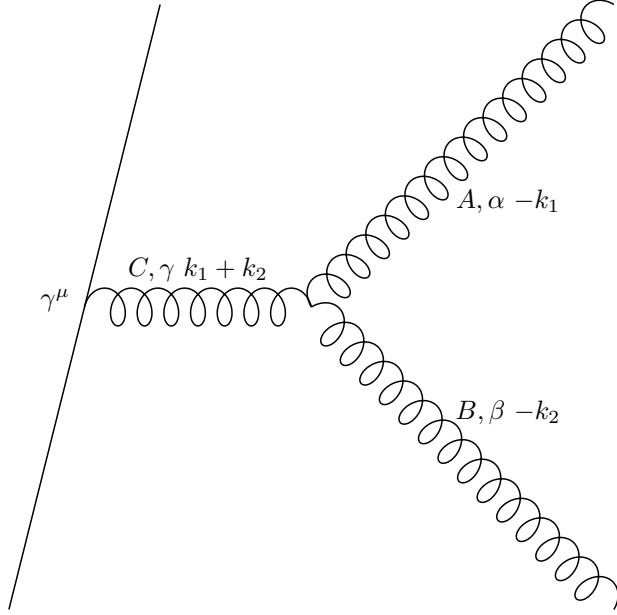


Figure C.1: The triple gluon vertex.

We show the labelling of indices and momenta for the triple gluon vertex in this case in Fig. C.1 and following the usual principles whereby the fermion line we assume is connected to a larger diagram, we write

$$\begin{aligned}
 \mathcal{M}_{n+1} = & g_s^2 \bar{u}(p) f^{ABC} t^C \gamma^\mu \frac{1}{(k_1 + k_2)^2} \left[-g^{\mu\gamma} + \frac{n^\mu (k_1 + k_2)^\gamma + n^\gamma (k_1 + k_2)^\mu}{n \cdot (k_1 + k_2)} \right] \\
 & \times [(-k_1 + k_2)^\gamma g^{\alpha\beta} - (k_1 + 2k_2)^\alpha g^{\beta\gamma} + (2k_1 + k_2)^\beta g^{\gamma\alpha}] \epsilon^{*\alpha}(k_1) \epsilon^{*\beta}(k_2) \mathcal{M}'_n.
 \end{aligned} \tag{C.0.1}$$

We then expand this, and use the subscripts $\epsilon_1 = \epsilon^{*\alpha}(k_1)$ and $\epsilon_2 = \epsilon^{*\beta}(k_2)$ and dropping the unnecessary prefactors, so that

$$\begin{aligned}
 \mathcal{M}_{n+1}^\mu &\sim [(k_1 - k_2)^\mu (\epsilon_1 \cdot \epsilon_2) + ((k_1 + 2k_2) \cdot \epsilon_1) \epsilon_2^\mu - ((k_2 + 2k_1) \cdot \epsilon_2) \epsilon_1^\mu] \\
 &\quad + \frac{1}{n \cdot (k_1 + k_2)} \left[((k_2 - k_1) \cdot (k_1 + k_2)) (\epsilon_1 \cdot \epsilon_2) n^\mu - ((k_1 + 2k_2) \cdot \epsilon_1) ((k_1 + k_2) \cdot \epsilon_2) n^\mu \right. \\
 &\quad + ((k_2 + 2k_1) \cdot \epsilon_2) ((k_1 + k_2) \cdot \epsilon_1) n^\mu + (n \cdot (k_2 - k_1)) (\epsilon_1 \cdot \epsilon_2) (k_1 + k_2)^\mu \\
 &\quad \left. - ((k_1 + 2k_2) \cdot \epsilon_1) (\epsilon_2 \cdot n) (k_1 + k_2)^\mu + ((2k_1 + k_2) \cdot \epsilon_2) (\epsilon_1 \cdot n) (k_1 + k_2)^\mu \right]
 \end{aligned} \tag{C.0.2}$$

and choosing to work in a physical gauge, such that $\epsilon_i \cdot k_i = 0$ and $\epsilon_i \cdot n = 0$, this becomes

$$\mathcal{M}_{n+1}^\mu \sim (k_1 - k_2)^\mu \epsilon_1 \cdot \epsilon_2 + 2k_2 \cdot \epsilon_1 \epsilon_2^\mu - 2k_1 \cdot \epsilon_2 \epsilon_1^\mu + \frac{\epsilon_1 \cdot \epsilon_2}{n \cdot (k_1 + k_2)} [(k_2 - k_1) \cdot n (k_1 + k_2)^\mu]. \tag{C.0.3}$$

Again, expanding the bracket, and using the strong ordering limit of $k_1 \gg k_2$ we get

$$\begin{aligned}
 \mathcal{M}_{n+1}^\mu &\sim (k_1 - k_2)^\mu \epsilon_1 \cdot \epsilon_2 + 2k_2 \cdot \epsilon_1 \epsilon_2^\mu - 2k_1 \cdot \epsilon_2 \epsilon_1^\mu + 2 \frac{\epsilon_1 \cdot \epsilon_2}{n \cdot (k_1 + k_2)} [(-n \cdot k_1) k_2^\mu + (k_2 \cdot n) k_1^\mu] \\
 &\sim \frac{2(k_2 \cdot \epsilon_1) \epsilon_2^\mu - 2(k_1 \cdot \epsilon_2) \epsilon_1^\mu}{2k_1 \cdot k_2} \\
 &\approx - \frac{k_1 \cdot \epsilon_2}{k_1 \cdot k_2} \epsilon_1^\mu.
 \end{aligned} \tag{C.0.4}$$

Now, putting the prefactors back in, we find that

$$\mathcal{M}_{n+1} = -g_s^2(p_b) f^{ABC} t^C \frac{k_1 \cdot \epsilon_2}{k_1 \cdot k_2} \bar{u}(p) \not{\epsilon}_1 \mathcal{M}'_n, \tag{C.0.5}$$

which can be used to derive radiation patterns for soft gluon emission when there is more than one gluon being emitted.

Appendix D

Veto Algorithm

We detail here the formalism laid out in Ref. [49] and outline the veto algorithm. If we start with a process involving particles beginning at time $t = 0$ and continuing to time t , *e.g.* radioactive decay, then the probability of particle decay at a certain time will be proportional to the probability that something will happen at a time t , $f(t)$, and the probability that nothing has happened by a time t , $\mathcal{N}(t)$, as clearly a particle cannot decay if it already has. We can therefore write the differential probability that something has happen at a time t as

$$\mathcal{P}(t) = -\frac{d\mathcal{N}}{dt} = f(t)\mathcal{N}(t), \quad (\text{D.0.1})$$

which is easily solved to give

$$\mathcal{P}(t) = f(t) \exp \left\{ -\int_0^t f(t') dt' \right\}. \quad (\text{D.0.2})$$

As discussed in terms of the Sudakov form factor in the introduction, the exponential can be thought of as the probability that nothing happens between the times $(0, t)$. In Appendix A, we see that this can be inverted if $f(t)$ has a primitive inverse to give the correct distribution of t

$$\int_0^t \mathcal{P}(t') dt' = \mathcal{N}(0) - \mathcal{N}(t) = 1 - \exp \left\{ -\int_0^t f(t') dt' \right\} = 1 - \mathcal{R}, \quad (\text{D.0.3})$$

where $\mathcal{R} \sim \text{Unif}[0, 1]$, so that

$$t = F^{-1} (F(0) - \ln \mathcal{R}), \quad (\text{D.0.4})$$

with $F(t)$ being the integral of $f(t') dt'$. If $f(t)$ does not have an analytic integral

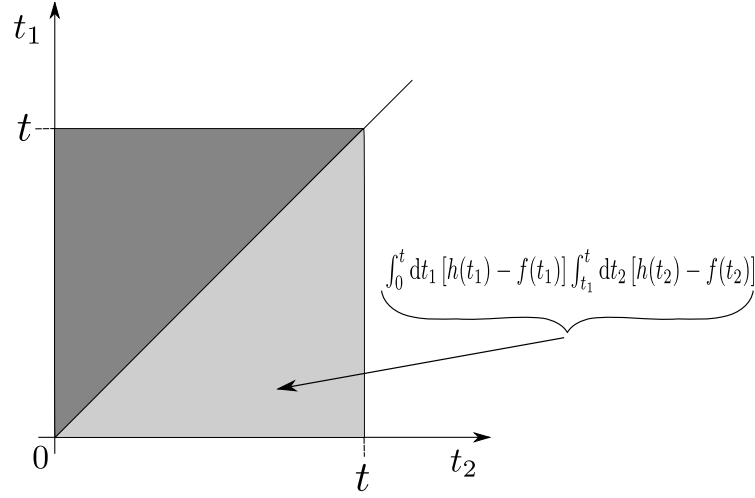


Figure D.1: The region of integration in the veto algorithm.

we need to use a hit or miss like method that takes care of the exponent properly and this is the so called veto algorithm.

Again, we start with an overestimate integral $h(t)$ and now select t_i according to $h(t)$, but as we have a process ordered in time t , we impose an additional constraint on our values that for a generated point i , we must have $t_i > t_{i-1}$. We then accept the new time t_i according to the probability $\frac{f(t_i)}{h(t_i)}$.

We can see how this works firstly if we reject no intermediate points, and the first try $t = t_1$ works, as then the probability of accepting the first point is given by

$$\mathcal{P}_0(t) = \exp \left\{ - \int_0^t h(t') dt' \right\} h(t) \frac{f(t)}{h(t)} = f(t) \exp \left\{ - \int_0^t h(t') dt' \right\}. \quad (\text{D.0.5})$$

Now, if we reject the first point t_1 and go on to accept a second t_2 , the probability associated with this is given by

$$\mathcal{P}_1(t) = \int_0^t dt_1 \exp \left\{ - \int_0^{t_1} h(t') dt' \right\} h(t_1) \left[1 - \frac{f(t_1)}{h(t_1)} \right] \exp \left\{ - \int_{t_1}^t h(t') dt' \right\} h(t) \frac{f(t)}{h(t)}, \quad (\text{D.0.6})$$

where we note we must integrate over all possible intermediate time periods. We can write this in terms of $\mathcal{P}_0(t)$ as

$$\mathcal{P}_1(t) = \mathcal{P}_0(t) \int_0^t dt_1 [h(t_1) - f(t_1)]. \quad (\text{D.0.7})$$

Continuing in the same way for more than one intermediate time being rejected,

we find that

$$\begin{aligned}\mathcal{P}_1(t) &= \mathcal{P}_0(t) \int_0^t dt_1 [h(t_1) - f(t_1)] \int_{t_1}^t dt_2 [h(t_2) - f(t_2)] \\ &= \mathcal{P}_0(t) \frac{1}{2} \left(\int_0^t dt' [h(t') - f(t')] \right)^2, \end{aligned} \quad (\text{D.0.8})$$

where to see the last equality, one can re-order the integration variables of t_1 and t_2 and then from Fig. D.1 the equality is seen.

In general if there are i intermediate times, these can be ordered in $i!$ ways, and so we have that

$$\begin{aligned}\mathcal{P}(t) &= \sum_{i=0}^{\infty} \mathcal{P}_i(t) = \mathcal{P}_0(t) \sum_{i=0}^{\infty} \frac{1}{i!} \left(\int_0^t dt' [h(t') - f(t')] \right)^i \\ &= f(t) \exp \left\{ - \int_0^t h(t') dt' \right\} \exp \left\{ - \int_0^t [h(t') - f(t')] dt' \right\} \\ &= \exp \left\{ - \int_0^t f(t') dt' \right\}. \end{aligned} \quad (\text{D.0.9})$$

Bibliography

- [1] A. Djouadi, J. Kalinowski, and M. Spira, *HDECAY: A Program for Higgs boson decays in the standard model and its supersymmetric extension*, *Comput.Phys.Commun.* **108** (1998) 56–74, [[hep-ph/9704448](#)].
- [2] **DELPHI** Collaboration, P. Abreu *et. al.*, *Tuning and Test of Fragmentation Models based on Identified Particles and Precision Event Shape Data*, *Z. Phys.* **C73** (1996) 11–60.
- [3] **ATLAS** Collaboration, G. Aad *et. al.*, *Search for New Physics in Dijet Mass and Angular Distributions in pp Collisions at $\sqrt{s} = 7$ TeV Measured with the ATLAS Detector*, *New J. Phys.* **13** (2011) 053044, [[arXiv:1103.3864](#)].
- [4] **ATLAS** Collaboration, G. Aad *et. al.*, *Update of the search for new physics in the dijet mass distribution in 163pb^{-1} of pp collisions at $\sqrt{s} = 7$ TeV measured with the ATLAS detector*, Tech. Rep. ATLAS-CONF-2011-081, CERN, Geneva, Jun, 2011.
- [5] G. P. Salam, *Towards Jetography*, *Eur.Phys.J.* **C67** (2010) 637–686, [[arXiv:0906.1833](#)].
- [6] **ALEPH** Collaboration, R. Barate *et. al.*, *Studies of Quantum Chromodynamics with the ALEPH detector*, *Phys. Rept.* **294** (1998) 1–165.
- [7] **Particle Data Group** Collaboration, C. Amsler *et. al.*, *Review of Particle Physics*, *Phys.Lett.* **B667** (2008) 1–1340.
- [8] G. Barker, E. Ben-Haim, M. Feindt, U. Kerzel, P. Roudeau, L. Ramler, and A. Savoy-Navarro, *A study of the b-quark fragmentation function with the*

- DELPHI detector at LEP I. oai:cds.cern.ch:994376*, Tech. Rep. DELPHI-2002-069-CONF-603. CERN-DELPHI-2002-069-CONF-603, CERN, Geneva, Jul, 2002.
- [9] S. Weinberg, *A model of leptons*, *Phys. Rev. Lett.* **19** (1967) 1264–1266.
- [10] S. Glashow, *Partial Symmetries of Weak Interactions*, *Nucl.Phys.* **22** (1961) 579–588.
- [11] P. W. Higgs, *Broken Symmetries and the Masses of Gauge Bosons*, *Phys. Rev. Lett.* **13** (1964) 508–509.
- [12] I. Aitchison and A. Hey, *Gauge Theories in Particle Physics. Volume 1: From Relativistic Quantum Mechanics to QED*. Taylor & Francis, 2003.
- [13] G. 't Hooft, *Renormalizable Lagrangians for Massive Yang-Mills Fields*, *Nucl.Phys.* **B35** (1971) 167–188.
- [14] G. 't Hooft, *Renormalization of Massless Yang-Mills Fields*, *Nucl.Phys.* **B33** (1971) 173–199.
- [15] F. Halzen and A. Martin, *Quarks & Leptons: An introductory course in modern particle physics*. John Wiley & Sons, New York, USA, 1984.
- [16] M. E. Peskin and D. V. Schroeder, *An Introduction to Quantum Field Theory*. Perseus Books, Cambridge, Massachusetts, 1995.
- [17] H. Georgie, *Lie Algebras In Particle Physics: From Isospin to Unified Theories*. Westview Press, 1999.
- [18] R. K. Ellis, W. J. Stirling, and B. R. Webber, *QCD and Collider Physics*, *Camb. Monogr. Part. Phys. Nucl. Phys. Cosmol.* **8** (1996) 1–435.
- [19] G. Dissertori, I. Knowles, and M. Schmelling, *Quantum Chromodynamics, High Energy Experiments and Theory*. Oxford Science Publications, Oxford, England, 2005.

- [20] J. C. Maxwell, *A dynamical theory of the electromagnetic field*, *Philosophical Transactions of the Royal Society of London* **155** (1865) 459–513.
- [21] N. Cabibbo, *Unitary Symmetry and Leptonic Decays*, *Phys.Rev.Lett.* **10** (1963) 531–533.
- [22] M. Kobayashi and T. Maskawa, *CP Violation in the Renormalizable Theory of Weak Interaction*, *Prog.Theor.Phys.* **49** (1973) 652–657.
- [23] **Particle Data Group** Collaboration, J. Beringer *et. al.*, *Review of Particle Physics (RPP)*, *Phys.Rev.* **D86** (2012) 010001.
- [24] Z. Maki, M. Nakagawa, and S. Sakata, *Remarks on the unified model of elementary particles*, *Prog.Theor.Phys.* **28** (1962) 870–880.
- [25] F. Olness and R. Scalise, *Regularization, Renormalization, and Dimensional Analysis: Dimensional Regularization meets Freshman EM*, *Am.J.Phys.* **79** (2011) 306, [[arXiv:0812.3578](https://arxiv.org/abs/0812.3578)].
- [26] B. Delamotte, *A Hint of renormalization*, *Am.J.Phys.* **72** (2004) 170–184, [[hep-th/0212049](https://arxiv.org/abs/hep-th/0212049)].
- [27] M. Srednicki, *Quantum Field Theory*. Cambridge University Press, 1 ed., 2007.
- [28] H. D. Politzer, *Reliable Perturbative Results for Strong Interactions?*, *Phys.Rev.Lett.* **30** (1973) 1346–1349.
- [29] D. Gross and F. Wilczek, *Asymptotically Free Gauge Theories. 1*, *Phys.Rev.* **D8** (1973) 3633–3652.
- [30] T.-P. Cheng and L.-F. Li, *Gauge Theory Of Elementary Particle Physics*. Oxford Science Publications, Oxford, England, 1982.
- [31] I. Aitchison and A. Hey, *Gauge Theories in Particle Physics. Volume 2: QCD and the Electroweak Theory*. Taylor & Francis, 2003.

- [32] F. Bloch and A. Nordsieck, *Note on the radiation field of the electron*, *Phys. Rev.* **52** (1937) 54–59.
- [33] T. Kinoshita, *Mass singularities of feynman amplitudes*, *J. Math. Phys.* **3** (1962) 650–677.
- [34] T. D. Lee and M. Nauenberg, *Degenerate systems and mass singularities*, *Phys. Rev.* **133** (1964) B1549–B1562.
- [35] J. Tully, *Monte Carlo simulations of hard QCD radiation*. PhD thesis, Durham University, 2009.
- [36] J. Kuipers, T. Ueda, J. Vermaseren, and J. Vollinga, *FORM version 4.0*, [arXiv:1203.6543](https://arxiv.org/abs/1203.6543).
- [37] M. Bahr *et. al.*, *Herwig++ Physics and Manual*, *Eur. Phys. J.* **C58** (2008) 639–707, [[arXiv:0803.0883](https://arxiv.org/abs/0803.0883)].
- [38] T. Plehn, *Lectures on LHC Physics*, *Lect. Notes Phys.* **844** (2012) 1–193, [[arXiv:0910.4182](https://arxiv.org/abs/0910.4182)].
- [39] G. Altarelli and G. Parisi, *Asymptotic Freedom in Parton Language*, *Nucl. Phys.* **B126** (1977) 298.
- [40] V. Gribov and L. Lipatov, *Deep inelastic e p scattering in perturbation theory*, *Sov. J. Nucl. Phys.* **15** (1972) 438–450.
- [41] Y. L. Dokshitzer, *Calculation of the Structure Functions for Deep Inelastic Scattering and e+ e- Annihilation by Perturbation Theory in Quantum Chromodynamics.*, *Sov. Phys. JETP* **46** (1977) 641–653.
- [42] A. Buckley *et. al.*, *General-purpose event generators for LHC physics*, [arXiv:1101.2599](https://arxiv.org/abs/1101.2599).
- [43] D. Amati, A. Bassetto, M. Ciafaloni, G. Marchesini, and G. Veneziano, *A Treatment of Hard Processes Sensitive to the Infrared Structure of QCD*, *Nucl. Phys.* **B173** (1980) 429.

- [44] G. Marchesini and B. R. Webber, *Simulation of QCD Coherence in Heavy Quark Production and Decay*, *Nucl. Phys.* **B330** (1990) 261.
- [45] P. Richardson and D. Winn, *Simulation of Sextet Diquark Production*, *Eur.Phys.J.* **C72** (2012) 1862, [arXiv:1108.6154].
- [46] J. C. Collins, D. E. Soper, and G. F. Sterman, *Factorization for Short Distance Hadron - Hadron Scattering*, *Nucl.Phys.* **B261** (1985) 104.
- [47] H. Murayama, I. Watanabe, and K. Hagiwara, *HELAS: HELicity amplitude subroutines for Feynman diagram evaluations*, KEK-91-11.
- [48] M. R. Whalley, D. Bourilkov, and R. C. Group, *The Les Houches accord PDFs (LHAPDF) and LHAGLUE*, hep-ph/0508110.
- [49] T. Sjöstrand, S. Mrenna, and P. Skands, *PYTHIA 6.4 Physics and Manual*, *JHEP* **05** (2006) 026, [hep-ph/0603175].
- [50] T. Sjöstrand, *A Model for Initial State Parton Showers*, *Phys. Lett.* **B157** (1985) 321.
- [51] G. Marchesini and B. R. Webber, *Monte Carlo Simulation of General Hard Processes with Coherent QCD radiation*, *Nucl. Phys.* **B310** (1988) 461.
- [52] D. Amati and G. Veneziano, *Preconfinement as a Property of Perturbative QCD*, *Phys. Lett.* **B83** (1979) 87.
- [53] B. R. Webber, *A QCD Model for Jet Fragmentation including Soft Gluon Interference*, *Nucl. Phys.* **B238** (1984) 492.
- [54] B. Andersson, G. Gustafson, G. Ingelman, and T. Sjostrand, *Parton Fragmentation and String Dynamics*, *Phys. Rept.* **97** (1983) 31-145.
- [55] B. Andersson, *The Lund model*, *Camb. Monogr. Part. Phys. Nucl. Phys. Cosmol.* **7** (1997) 1-471.
- [56] S. Catani and M. H. Seymour, *A general algorithm for calculating jet cross sections in NLO QCD*, *Nucl. Phys.* **B485** (1997) 291-419, [hep-ph/9605323].

- [57] S. Catani, S. Dittmaier, M. H. Seymour, and Z. Trócsányi, *The Dipole Formalism for Next-to-Leading Order QCD Calculations with Massive Partons*, *Nucl. Phys.* **B627** (2002) 189–265, [[hep-ph/0201036](#)].
- [58] S. Catani and M. H. Seymour, *Jet cross-sections at next-to-leading order*, *Acta Phys. Polon.* **B28** (1997) 863–881, [[hep-ph/9612236](#)].
- [59] S. Frixione and B. R. Webber, *Matching NLO QCD Computations and Parton Shower Simulations*, *JHEP* **06** (2002) 029, [[hep-ph/0204244](#)].
- [60] P. Nason, *A new method for combining NLO QCD with shower Monte Carlo algorithms*, *JHEP* **11** (2004) 040, [[hep-ph/0409146](#)].
- [61] S. Frixione, P. Nason, and C. Oleari, *Matching NLO QCD computations with Parton Shower simulations: the POWHEG method*, *JHEP* **11** (2007) 070, [[0709.2092](#)].
- [62] K. Hamilton, P. Richardson, and J. Tully, *A Positive-Weight Next-to-Leading Order Monte Carlo Simulation of Drell-Yan Vector Boson Production*, *JHEP* **0810** (2008) 015, [[arXiv:0806.0290](#)].
- [63] K. Hamilton, P. Richardson, and J. Tully, *A Positive-Weight Next-to-Leading Order Monte Carlo Simulation for Higgs Boson Production*, *JHEP* **04** (2009) 116, [[arXiv:0903.4345](#)].
- [64] L. D’Errico and P. Richardson, *A Positive-Weight Next-to-Leading-Order Monte Carlo Simulation of Deep Inelastic Scattering and Higgs Boson Production via Vector Boson Fusion in Herwig++*, *Eur.Phys.J.* **C72** (2012) 2042, [[arXiv:1106.2983](#)].
- [65] P. Z. Skands, *Tuning Monte Carlo Generators: The Perugia Tunes*, *Phys.Rev.* **D82** (2010) 074018, [[arXiv:1005.3457](#)].
- [66] B. Cooper, J. Katzy, M. Mangano, A. Messina, L. Mijovic, *et. al.*, *Importance of a consistent choice of $\alpha(s)$ in the matching of AlpGen and Pythia*, *Eur.Phys.J.* **C72** (2012) 2078, [[arXiv:1109.5295](#)].

- [67] A. Buckley, H. Hoeth, H. Lacker, H. Schulz, and J. E. von Seggern, *Systematic event generator tuning for the LHC*, *Eur. Phys. J.* **C65** (2010) 331–357, [arXiv:0907.2973].
- [68] J. M. Butterworth, A. R. Davison, M. Rubin, and G. P. Salam, *Jet substructure as a new Higgs search channel at the LHC*, *Phys. Rev. Lett.* **100** (2008) 242001, [arXiv:0802.2470].
- [69] S. D. Ellis, C. K. Vermilion, and J. R. Walsh, *Techniques for improved heavy particle searches with jet substructure*, *Phys. Rev.* **D80** (2009) 051501, [arXiv:0903.5081].
- [70] S. D. Ellis, C. K. Vermilion, and J. R. Walsh, *Recombination Algorithms and Jet Substructure: Pruning as a Tool for Heavy Particle Searches*, *Phys. Rev.* **D81** (2010) 094023, [arXiv:0912.0033].
- [71] G. D. Kribs, A. Martin, T. S. Roy, and M. Spannowsky, *Discovering the Higgs Boson in New Physics Events using Jet Substructure*, *Phys. Rev.* **D81** (2010) 111501, [arXiv:0912.4731].
- [72] G. D. Kribs, A. Martin, T. S. Roy, and M. Spannowsky, *Discovering Higgs Bosons of the MSSM using Jet Substructure*, *Phys. Rev.* **D82** (2010) 095012, [arXiv:1006.1656].
- [73] G. D. Kribs, A. Martin, and T. S. Roy, *Higgs boson discovery through top-partners decays using jet substructure*, *Phys.Rev.* **D84** (2011) 095024, [arXiv:1012.2866].
- [74] J. M. Butterworth, J. R. Ellis, A. R. Raklev, and G. P. Salam, *Discovering baryon-number violating neutralino decays at the LHC*, *Phys.Rev.Lett.* **103** (2009) 241803, [arXiv:0906.0728].
- [75] **CDF Collaboration** Collaboration, T. Aaltonen *et. al.*, *Study of Substructure of High Transverse Momentum Jets Produced in Proton-Antiproton Collisions at $\sqrt{s} = 1.96$ TeV*, *Phys.Rev.* **D85** (2012) 091101, [arXiv:1106.5952].

- [76] Y. Bai and J. Shelton, *Composite Octet Searches with Jet Substructure*, *JHEP* **1207** (2012) 067, [[arXiv:1107.3563](#)].
- [77] C. K. Vermilion, *Jet Substructure at the Large Hadron Collider: Harder, Better, Faster, Stronger*, [arXiv:1101.1335](#). Ph.D.Thesis.
- [78] T. Plehn, G. P. Salam, and M. Spannowsky, *Fat Jets for a Light Higgs*, *Phys.Rev.Lett.* **104** (2010) 111801, [[arXiv:0910.5472](#)].
- [79] M. H. Seymour, *Searches for new particles using cone and cluster jet algorithms: A Comparative study*, *Z.Phys.* **C62** (1994) 127–138.
- [80] A. Abdesselam, E. B. Kuutmann, U. Bitenc, G. Brooijmans, J. Butterworth, *et. al.*, *Boosted objects: A Probe of beyond the Standard Model physics*, *Eur.Phys.J.* **C71** (2011) 1661, [[arXiv:1012.5412](#)].
- [81] I. Feige, M. D. Schwartz, I. W. Stewart, and J. Thaler, *Precision Jet Substructure from Boosted Event Shapes*, *Phys.Rev.Lett.* **109** (2012) 092001, [[arXiv:1204.3898](#)].
- [82] A. Altheimer, S. Arora, L. Asquith, G. Brooijmans, J. Butterworth, *et. al.*, *Jet Substructure at the Tevatron and LHC: New results, new tools, new benchmarks*, *J.Phys.G* **39** (2012) 063001, [[arXiv:1201.0008](#)].
- [83] S. Yang and Q.-S. Yan, *Searching for Heavy Charged Higgs Boson with Jet Substructure at the LHC*, *JHEP* **1202** (2012) 074, [[arXiv:1111.4530](#)].
- [84] J. M. Butterworth, B. E. Cox, and J. R. Forshaw, *WW scattering at the CERN LHC*, *Phys. Rev.* **D65** (2002) 096014, [[hep-ph/0201098](#)].
- [85] J. M. Butterworth, J. R. Ellis, and A. R. Raklev, *Reconstructing sparticle mass spectra using hadronic decays*, *JHEP* **05** (2007) 033, [[hep-ph/0702150](#)].
- [86] *Measurement of jet mass and substructure for inclusive jets in $\sqrt{s} = 7$ Tev pp collisions with the ATLAS experiment*, Tech. Rep. ATLAS-CONF-2011-073, CERN, Geneva, May, 2011.

- [87] *ATLAS sensitivity to the standard model higgs in the HW and HZ channels at high transverse momenta*, Tech. Rep. ATL-PHYS-PUB-2009-088, CERN, Geneva, Aug, 2009.
- [88] *Study of jet substructure in pp collisions at 7 Tev in CMS*, Tech. Rep. CMS PAS JME 10-013, CERN, Geneva, March, 2011.
- [89] G. Corcella *et. al.*, *HERWIG 6: An event generator for Hadron Emission Reactions with Interfering Gluons (including supersymmetric processes)*, *JHEP* **01** (2001) 010, [[hep-ph/0011363](#)].
- [90] G. Corcella *et. al.*, *HERWIG 6.5 Release Note*, [hep-ph/0210213](#).
- [91] J. M. Butterworth, J. R. Forshaw, and M. H. Seymour, *Multi-Parton Interactions in Photoproduction at HERA*, *Z. Phys.* **C72** (1996) 637–646, [[hep-ph/9601371](#)].
- [92] K. Arnold, L. d’Errico, S. Gieseke, D. Grellscheid, K. Hamilton, *et. al.*, *Herwig++ 2.6 Release Note*, [arXiv:1205.4902](#).
- [93] S. Gieseke, P. Stephens, and B. Webber, *New Formalism for QCD Parton Showers*, *JHEP* **12** (2003) 045, [[hep-ph/0310083](#)].
- [94] M. Bahr, S. Gieseke, and M. H. Seymour, *Simulation of multiple partonic interactions in Herwig++*, *JHEP* **0807** (2008) 076, [[arXiv:0803.3633](#)].
- [95] M. Bahr, J. M. Butterworth, and M. H. Seymour, *The Underlying Event and the Total Cross Section from Tevatron to the LHC*, *JHEP* **0901** (2009) 065, [[arXiv:0806.2949](#)].
- [96] S. Gieseke, C. Rohr, and A. Siodmok, *Colour reconnections in Herwig++*, *Eur.Phys.J.* **C72** (2012) 2225, [[arXiv:1206.0041](#)].
- [97] S. Gieseke, C. Röhr, and A. Siodmok, *Multiple Partonic Interaction Developments in Herwig++*, [arXiv:1110.2675](#).

- [98] **ATLAS Collaboration** Collaboration, G. Aad *et. al.*, *Jet mass and substructure of inclusive jets in $\sqrt{s} = 7$ TeV pp collisions with the ATLAS experiment*, *JHEP* **1205** (2012) 128, [[arXiv:1203.4606](#)].
- [99] **ATLAS Collaboration** Collaboration, G. Aad *et. al.*, *ATLAS measurements of the properties of jets for boosted particle searches*, *Phys.Rev.* **D86** (2012) 072006, [[arXiv:1206.5369](#)].
- [100] E. Braaten and J. Leveille, *Higgs Boson Decay and the Running Mass*, *Phys.Rev.* **D22** (1980) 715.
- [101] A. Buckley, J. Butterworth, L. Lonnblad, H. Hoeth, J. Monk, *et. al.*, *Rivet user manual*, [arXiv:1003.0694](#).
- [102] J. Pumplin, D. Stump, R. Brock, D. Casey, J. Huston, *et. al.*, *Uncertainties of predictions from parton distribution functions. 2. The Hessian method*, *Phys.Rev.* **D65** (2001) 014013, [[hep-ph/0101032](#)].
- [103] J. Pumplin, D. Stump, and W. Tung, *Multivariate fitting and the error matrix in global analysis of data*, *Phys.Rev.* **D65** (2001) 014011, [[hep-ph/0008191](#)].
- [104] Y. L. Dokshitzer, G. D. Leder, S. Moretti, and B. R. Webber, *Better Jet Clustering Algorithms*, *JHEP* **08** (1997) 001, [[hep-ph/9707323](#)].
- [105] M. Wobisch, *Measurement and QCD analysis of jet cross sections in deep-inelastic positron proton collisions at $\sqrt{s} = 300$ GeV*, .
DESY-THESIS-2000-049.
- [106] M. Cacciari and G. P. Salam, *Dispelling the N^3 myth for the k_t jet-finder*, *Phys. Lett.* **B641** (2006) 57–61, [[hep-ph/0512210](#)].
- [107] **ATLAS Collaboration** Collaboration, G. Aad *et. al.*, *Observation of a new particle in the search for the Standard Model Higgs boson with the ATLAS detector at the LHC*, *Phys.Lett.* **B716** (2012) 1–29, [[arXiv:1207.7214](#)].

- [108] **CMS Collaboration** Collaboration, S. Chatrchyan *et. al.*, *Observation of a new boson at a mass of 125 GeV with the CMS experiment at the LHC*, *Phys.Lett.* **B716** (2012) 30–61, [[arXiv:1207.7235](#)].
- [109] K. Hamilton and P. Richardson, *A Simulation of QCD Radiation in Top Quark Decays*, *JHEP* **02** (2007) 069, [[hep-ph/0612236](#)].
- [110] K. Hamilton, *A positive-weight next-to-leading order simulation of weak boson pair production*, *JHEP* **1101** (2011) 009, [[arXiv:1009.5391](#)].
- [111] **CDF Collaboration** Collaboration, F. Abe *et. al.*, *Observation of top quark production in $\bar{p}p$ collisions*, *Phys.Rev.Lett.* **74** (1995) 2626–2631, [[hep-ex/9503002](#)].
- [112] **D0 Collaboration** Collaboration, S. Abachi *et. al.*, *Observation of the top quark*, *Phys.Rev.Lett.* **74** (1995) 2632–2637, [[hep-ex/9503003](#)].
- [113] **CDF Collaboration, D0 Collaboration** Collaboration, T. Aaltonen *et. al.*, *Combination of the top-quark mass measurements from the Tevatron collider*, *Phys.Rev.D* (2012) [[arXiv:1207.1069](#)].
- [114] **CMS Collaboration**, S. Chatrchyan *et. al.*, *Top mass combination*, Tech. Rep. CMS-PAS-TOP-11-018, CERN, 2012.
- [115] **ATLAS Collaboration** Collaboration, G. Aad *et. al.*, *Measurement of the top quark mass with the template method in the $t\bar{t}$ lepton plus jets channel using ATLAS data*, *Eur.Phys.J.* **C72** (2012) 2046, [[arXiv:1203.5755](#)].
- [116] **CDF Collaboration** Collaboration, A. Abulencia *et. al.*, *Top quark mass measurement using the template method in the lepton + jets channel at CDF II*, *Phys.Rev.* **D73** (2006) 032003, [[hep-ex/0510048](#)].
- [117] **CDF Collaboration** Collaboration, A. Abulencia *et. al.*, *Measurement of the top quark mass using template methods on dilepton events in proton antiproton collisions at $\sqrt{s} = 1.96$ -TeV.*, *Phys.Rev.* **D73** (2006) 112006, [[hep-ex/0602008](#)].

- [118] A. Etienvre, *Top quark mass measurement using template methods, with 35pb1 recorded by the ATLAS detector, at $\sqrt{s} = 7$ TeV.*, Tech. Rep. ATL-PHYS-PROC-2011-191, CERN, Geneva, Oct, 2011.
- [119] K. Kondo, *Dynamical likelihood method for reconstruction of events with missing momentum. 1: Method and toy models*, *J.Phys.Soc.Jap.* **57** (1988) 4126–4140.
- [120] K. Kondo, *Dynamical likelihood method for reconstruction of events with missing momentum. 2: Mass spectra for $2 \rightarrow 2$ processes*, *J.Phys.Soc.Jap.* **60** (1991) 836–844.
- [121] R. Dalitz and G. R. Goldstein, *The Decay and polarization properties of the top quark*, *Phys.Rev.* **D45** (1992) 1531–1543.
- [122] A. H. Hoang, A. Jain, I. Scimemi, and I. W. Stewart, *Infrared Renormalization Group Flow for Heavy Quark Masses*, *Phys.Rev.Lett.* **101** (2008) 151602, [[arXiv:0803.4214](#)].
- [123] S. Fleming, A. H. Hoang, S. Mantry, and I. W. Stewart, *Jets from massive unstable particles: Top-mass determination*, *Phys.Rev.* **D77** (2008) 074010, [[hep-ph/0703207](#)].
- [124] S. Fleming, A. H. Hoang, S. Mantry, and I. W. Stewart, *Top Jets in the Peak Region: Factorization Analysis with NLL Resummation*, *Phys.Rev.* **D77** (2008) 114003, [[arXiv:0711.2079](#)].
- [125] A. H. Hoang and I. W. Stewart, *Top Mass Measurements from Jets and the Tevatron Top-Quark Mass*, *Nucl.Phys.Proc.Suppl.* **185** (2008) 220–226, [[arXiv:0808.0222](#)].
- [126] U. Langenfeld, S. Moch, and P. Uwer, *Measuring the running top-quark mass*, *Phys.Rev.* **D80** (2009) 054009, [[arXiv:0906.5273](#)].
- [127] **D0 Collaboration** Collaboration, V. Abazov *et. al.*, *Measurement of the $t\bar{t}$ production cross section in $p\bar{p}$ collisions at $\sqrt{s} = 1.96$ -TeV*, *Phys.Rev.Lett.* **100** (2008) 192004, [[arXiv:0803.2779](#)].

- [128] V. A. Khoze and T. Sjostrand, *Color correlations and multiplicities in top events*, *Phys.Lett.* **B328** (1994) 466–476, [[hep-ph/9403394](#)].
- [129] R. K. Ellis and J. Sexton, *Explicit Formulae for Heavy Flavor Production*, *Nucl.Phys.* **B282** (1987) 642.
- [130] L. H. Orr and W. J. Stirling, *Additional soft jets in $t\bar{t}$ production at the Tevatron $p\bar{p}$ collider*, *Phys.Rev.* **D51** (1995) 1077–1085, [[hep-ph/9409238](#)].
- [131] V. A. Khoze, J. Ohnemus, and W. J. Stirling, *Soft gluon radiation in hadronic $t\bar{t}$ production*, *Phys.Rev.* **D49** (1994) 1237–1245, [[hep-ph/9308359](#)].
- [132] T. Hahn, *Generating Feynman diagrams and amplitudes with FeynArts 3*, *Comput.Phys.Commun.* **140** (2001) 418–431, [[hep-ph/0012260](#)].
- [133] R. Mertig, M. Bohm, and A. Denner, *FEYN CALC: Computer algebraic calculation of Feynman amplitudes*, *Comput.Phys.Commun.* **64** (1991) 345–359.
- [134] V. A. Khoze, W. J. Stirling, and L. H. Orr, *Soft gluon radiation in $e^+e^- \rightarrow t\bar{t}$* , *Nucl.Phys.* **B378** (1992) 413–442.
- [135] T. Plehn, M. Spannowsky, M. Takeuchi, and D. Zerwas, *Stop Reconstruction with Tagged Tops*, *JHEP* **1010** (2010) 078, [[arXiv:1006.2833](#)].
- [136] W. J. Marciano, *Exotic New Quarks and Dynamical Symmetry Breaking*, *Phys. Rev.* **D21** (1980) 2425.
- [137] K. Fukazawa *et. al.*, *Dynamical breaking of electroweak symmetry by color sextet quark condensates*, *Prog. Theor. Phys.* **85** (1991) 111–130.
- [138] T. Han, I. Lewis, and T. McElmurry, *QCD Corrections to Scalar Diquark Production at Hadron Colliders*, *JHEP* **01** (2010) 123, [[arXiv:0909.2666](#)].
- [139] H. Zhang, E. L. Berger, Q.-H. Cao, C.-R. Chen, and G. Shaughnessy, *Color Sextet Vector Bosons and Same-Sign Top Quark Pairs at the LHC*, *Phys. Lett.* **B696** (2011) 68–73, [[arXiv:1009.5379](#)].

- [140] C.-R. Chen, W. Klemm, V. Rentala, and K. Wang, *Color Sextet Scalars at the CERN Large Hadron Collider*, *Phys. Rev.* **D79** (2009) 054002, [arXiv:0811.2105].
- [141] E. Arik, O. Cakir, S. A. Cetin, and S. Sultansoy, *A Search for vector diquarks at the CERN LHC*, *JHEP* **09** (2002) 024, [hep-ph/0109011].
- [142] R. N. Mohapatra, N. Okada, and H.-B. Yu, *Diquark Higgs at LHC*, *Phys. Rev.* **D77** (2008) 011701, [arXiv:0709.1486].
- [143] E. L. Berger, Q.-H. Cao, C.-R. Chen, G. Shaughnessy, and H. Zhang, *Color Sextet Scalars in Early LHC Experiments*, *Phys. Rev. Lett.* **105** (2010) 181802, [arXiv:1005.2622].
- [144] O. Cakir and M. Sahin, *Resonant production of diquarks at high energy pp, ep and e+ e- colliders*, *Phys. Rev.* **D72** (2005) 115011, [hep-ph/0508205].
- [145] T. Han, I. Lewis, and Z. Liu, *Colored Resonant Signals at the LHC: Largest Rate and Simplest Topology*, *JHEP* **1012** (2010) 085, [arXiv:1010.4309].
- [146] H. Tanaka and I. Watanabe, *Color sextet quark productions at hadron colliders*, *Int. J. Mod. Phys.* **A7** (1992) 2679–2694.
- [147] K. M. Patel and P. Sharma, *Forward-backward asymmetry in top quark production from light colored scalars in SO(10) model*, *JHEP* **04** (2011) 085, [arXiv:1102.4736].
- [148] S. Atag, O. Cakir, and S. Sultansoy, *Resonance production of diquarks at the CERN LHC*, *Phys. Rev.* **D59** (1999) 015008.
- [149] E. Ma, M. Raidal, and U. Sarkar, *Probing the exotic particle content beyond the standard model*, *Eur. Phys. J.* **C8** (1999) 301–309, [hep-ph/9808484].
- [150] H. E. Haber and G. L. Kane, *The Search for Supersymmetry: Probing Physics Beyond the Standard Model*, *Phys.Rept.* **117** (1985) 75–263.
- [151] M. Cacciari, G. P. Salam, and G. Soyez, *The anti- k_t jet clustering algorithm*, *JHEP* **04** (2008) 063, [arXiv:0802.1189].

- [152] A. Sherstnev and R. S. Thorne, *Parton Distributions for LO Generators*, *Eur. Phys. J.* **C55** (2008) 553–575, [arXiv:0711.2473].
- [153] F. James and M. Roos, *Minuit: A System for Function Minimization and Analysis of the Parameter Errors and Correlations*, *Comput.Phys.Commun.* **10** (1975) 343–367.
- [154] S. Weinzierl, *Introduction to Monte Carlo methods*, hep-ph/0006269.
- [155] J. E. Huth, N. Wainer, K. Meier, N. Hadley, F. Aversa, *et. al.*, *Toward a standardization of jet definitions*, .
- [156] S. D. Ellis, Z. Kunszt, and D. E. Soper, *The One Jet Inclusive Cross-Section at $\mathcal{O}(\alpha_s^3)$. 1. Gluons Only*, *Phys.Rev.* **D40** (1989) 2188.
- [157] G. P. Salam and G. Soyez, *A Practical Seedless Infrared-Safe Cone jet algorithm*, *JHEP* **0705** (2007) 086, [arXiv:0704.0292].
- [158] **JADE Collaboration** Collaboration, W. Bartel *et. al.*, *Experimental Studies on Multi-Jet Production in $e^+ e^-$ Annihilation at PETRA Energies*, *Z.Phys.* **C33** (1986) 23.
- [159] **JADE Collaboration** Collaboration, S. Bethke *et. al.*, *Experimental Investigation of the Energy Dependence of the Strong Coupling Strength*, *Phys.Lett.* **B213** (1988) 235.
- [160] S. D. Ellis and D. E. Soper, *Successive combination jet algorithm for hadron collisions*, *Phys.Rev.* **D48** (1993) 3160–3166, [hep-ph/9305266].
- [161] S. Catani, Y. L. Dokshitzer, M. Seymour, and B. Webber, *Longitudinally invariant K_t clustering algorithms for hadron hadron collisions*, *Nucl.Phys.* **B406** (1993) 187–224.